Design of Water-Splitting Photocatalysts by First Principles Computations

by

Yabi Wu
B.Sc., Peking University (2008)

Submitted to the Department of Materials Science and Engineering
in Partial Fulfillment of the Requirements for the Degree of

Doctor of Philosophy

at the

MASSACHUSETTS INSTITUTE OF TECHNOLOGY

October 2013
[FEBRUARY 2014]

Signature of Author ....
Yabi Wu
Department of Materials Science and Engineering
October 2013

Certified by ....
Gerbrand Ceder
R.P. Simmons Professor of Materials Science and Engineering
Thesis Supervisor

Accepted by ....
Gerbrand Ceder
Chair, Departmental Committee on Graduate Students

Abstract

This thesis focuses on the design of novel inorganic water-splitting photocatalysts for solar applications using first principles computations. Water-splitting photocatalysts are materials that can photo-catalyze the water-splitting reaction under certain conditions. They provide an alternative way to capture and store the energy from the sun. Currently, the energy conversion efficiency of photocatalytic devices under solar illumination and in pure water (pH=7) is still far from the commercialization target. The design of new photocatalysts with better potentials is the key to solve this problem.

We have first developed a so-called three-step method to compute the relative position of a semiconductor's conduction band (valence band) vs. the H_2/H_2O (O_2/H_2O) level in solution from first principles. The merits of the method have been highlighted, and the performance of the method has been tested and compared with the performance of other methods. We conclude that the three-step method provides the desired accuracy for high throughput screening at an acceptable computational cost.

We have designed a three-tier first principles high throughput screening system to identify new water-splitting photocatalysts by examining the phase stability, band gap and band edge positions of the candidate compounds. We construct the screening system by integrating the three-step method together with other previously developed methods in our group. We use the system to screen about 3000 different materials. Through the screening, most of the known water-splitting photocatalysts have been reproduced and, more importantly, sixteen new promising candidates have been proposed. Properties of these new candidates have been analyzed and compared to those of the known photocatalysts. Some particularly promising ones are highlighted.

$Ti_3O_3N_2$ is one of the identified candidates from the high throughput screening, and is particularly interesting as it has good phase stability, a low band gap and suitable band edge positions. In addition, it has the same crystal structure as Ta_3N_5, which is also a photocatalyst with a low band gap. This leads to our study on the Ta_3N_5:$Ti_3O_3N_2$ solid solution as a water-splitting photocatalyst. Using first principles computations, we study the phase stability, band gap and band edge positions of the solid solution. The results suggest that the Ta_3N_5:$Ti_3O_3N_2$ solid solution may have a better potential than both its end members as a water-splitting photocatalyst.

Thesis Supervisor: Gerbrand Ceder

Title: R.P. Simmons Professor of Materials Science and Engineering

Acknowledgements

I have received a lot of help in my graduate life. I owe many thanks and much appreciation to everyone who helped me throughout graduate school. I would like to take this opportunity to express my gratitude to all of them.

I would like to first thank my advisor, Professor Ceder. I am very lucky to have him, a professional, inspiring and intelligent advisor, supervise my Ph.D. research. It is him who led me to the field of water-splitting photocatalysis. Otherwise, I may have not noticed this interesting field. He always encourages us to solve the major problems of a field. Therefore, I chose my Ph.D. project as the design of new water-splitting photocatalysts. He has provided a very stable environment for my research and is always very helpful in generating ideas and discussing research results. In addition, his teaching and presenting style deeply influenced me.

I am also deeply grateful to my family members who are always my firmest support. My parents understand me a lot and always give me an indispensable mental support. My wife, being also a MIT graduate student, has accompanied me all the way along my graduate life. I always feel very lucky that I have her around these years, sharing the joys and sadness, taking care of each other, and enjoying the research experience.

I want to thank all my collaborators, all members of Ceder group and all my friends too. This thesis would have been impossible without the important contributions of my co-workers, Maria K. Chan, Shyue Ping Ong, Oliviero Andreussi, Predrag Lazic, Geoffroy

Hautier, and Kristin Persson. Meanwhile, many of my research progresses were driven by the valuable discussions with Ruoshi Sun, ShinYoung Kang, Rahul Malik, Aziz Abdellahi, Alexander Urban, and Yifei Mo. In addition, I sincerely thank every member in the Ceder group for creating such a creative and stimulating working atmosphere, and thank all my friends for sharing their life and research experience with me. I have learned a lot from each of you.

Table of Contents

Chapter I. Introduction

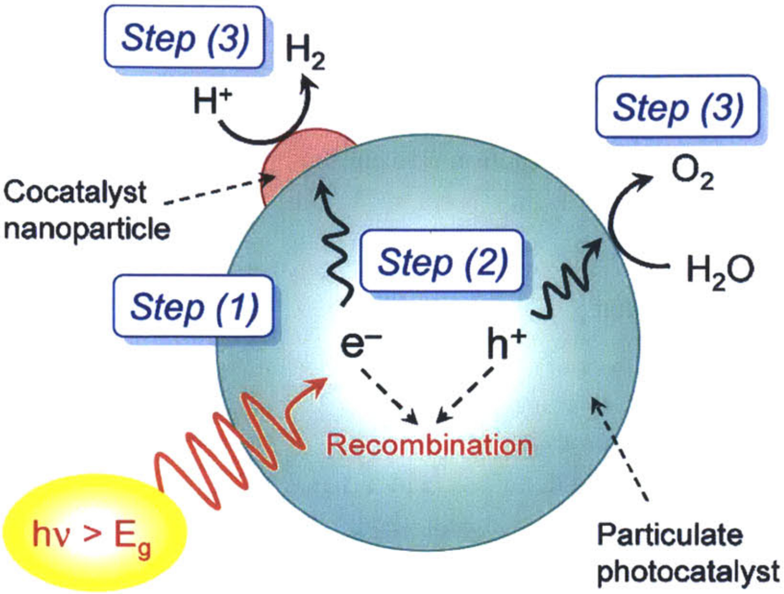

Figure 1.1 A schematic illustration of the water-splitting photocatalysis*. Step (1): photon absorption and electron-hole excitation. Step (2): electron-hole separation and transportation. Step (3): HER and OER activation.

$$H_2O(l) \xrightarrow{h\nu \geq 1.23eV} H_2(g) + \frac{1}{2}O_2(g) \quad (\Delta G = 237kJ/mol) \tag{1.1}$$

Water-splitting photocatalysts are materials that can photo-catalyze the water-splitting reaction (Eqn. 1.1) under certain conditions. Although they can be in the form of either inorganic semiconductors[1-3] or molecular materials[4-8], we focus on inorganic photocatalysts in this thesis. In the photocatalysis process (Fig. 1.1), the photocatalyst absorbs photons from artificial or natural lights, and generates excited electron-hole pairs. After separate with each other, the electrons and holes travel to the photocatalyst-solution interface and activate the hydrogen evolution reaction (HER) and oxygen evolution

---

* Reprinted (adapted) with permission from *J. Phys. Chem. C, 2007, 111 (22), 7851–7861*. Copyright (2007) American Chemical Society.

reaction (OER) respectively[1-2]. The difference of these two reduction potentials is 1.23 eV, indicating that the band gap of the photocatalyst must be greater than this value otherwise the absorbed photons do not have enough energy to drive the photocatalysis process[1-2]. In many cases, some co-catalysts are also used to reduce the kinetic barrier of the HER or OER so that the reaction rate can be improved[1-3].

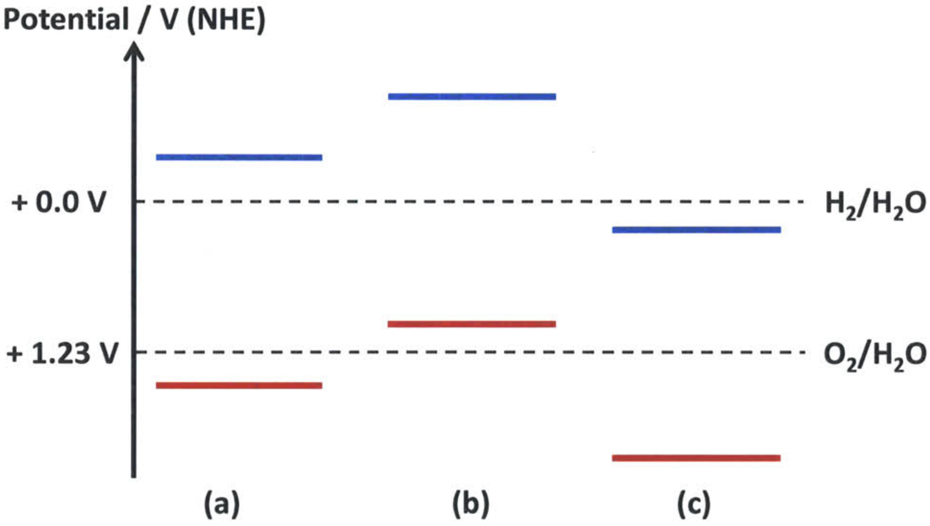

Figure 1.2 A diagram of the energetic requirements for the band edge positions at the photocatalyst-solution interface. Blue lines represent the CB positions while red lines represent the VB positions. (a) favorable band level arrangement; (b) unfavorable VB position; (c) unfavorable CB position.

Besides a band gap greater than 1.23 eV, the photocatalyst must also have its conduction band (CB) higher than the H_2/H_2O redox level in solution and have its valence band (VB) lower than the O_2/H_2O redox level in solution[9-11]. Otherwise, the HER or OER is not energetically favorable (Fig 1.2). Here and throughout this thesis, "higher" always refers to more negative in the Normal Hydrogen Electrode (NHE) reference while "lower" always refers to more positive in the NHE reference. It is worth to note that the CB and VB positions considered here should be the band edge positions at the photocatalyst-solution interface. They are usually different than the band edge positions in the bulk photocatalysts due to the band bending effect[11]. We will explain this point further in Chapter II.

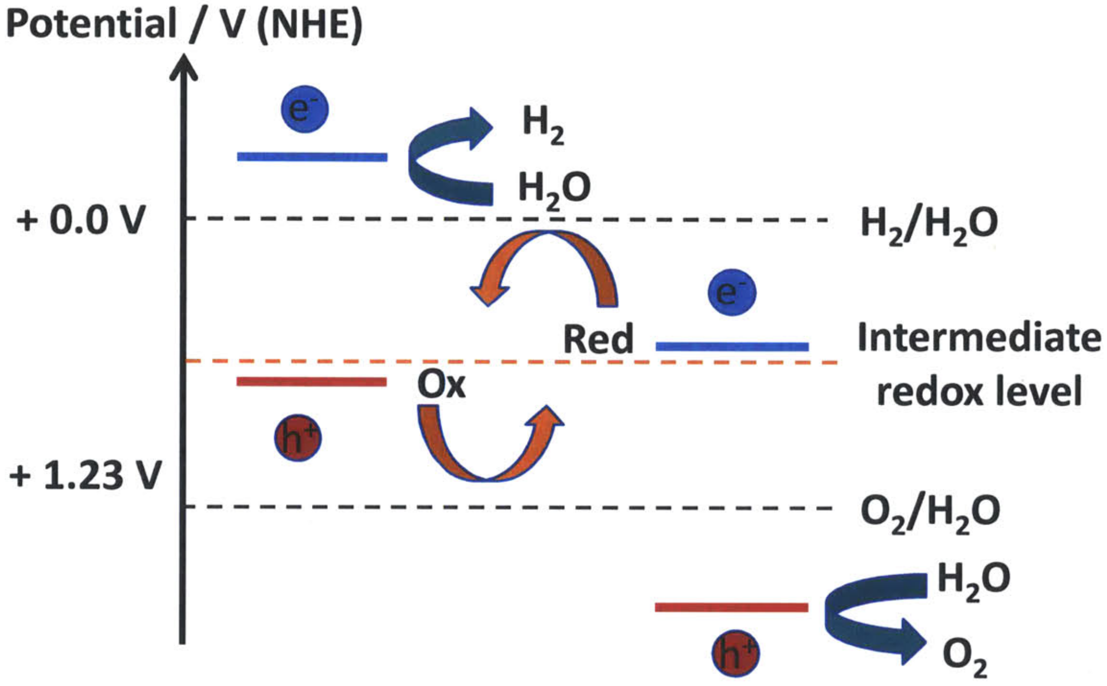

Figure 1.3 A schematic illustration of the z-scheme photocatalysts. Blue lines represent the CB positions while red lines represent the VB positions.

Alternatively, two materials may work together in a so-called z-scheme[1-2, 12-14] (Fig 1.3), one for anode where the OER takes place and one for cathode where the HER takes place. In this case, two photons are absorbed in order to provide one effective pair of electron and hole, which are the electron from the cathode and the hole from the anode. To cycle the other pair of the excited electron and hole (the electron from the anode and the hole from the cathode) which is not effective in the water-splitting reaction, some intermediate redox level should be introduced (Fig. 1.3). This intermediate redox level is often provided by certain ion couples in the solution[1-2, 12-14]. In the z-scheme, the photocatalysis process is energetically favorable if the anode material has its VB lower than the O_2/H_2O level and its CB higher than the intermediate redox level, while the cathode material has its CB higher than the H_2/H_2O level and its VB lower than the intermediate redox level[1-2, 14].

In principle, the z-scheme based photocatalysts have advantages over the single material photocatalysts in solar applications, since they are more flexible in band gaps and may absorb more faction of the solar spectrum[14], although they use only half of the excited electrons and holes. However, the z-scheme design dramatically increases the complexity of the device and the fabrication costs. In addition, it is usually not easy to find suitable ion couples that can provide the desired intermediate redox level. Therefore, we still mainly focus on the single material photocatalysts in this thesis.

There are mainly two types of water-splitting photocatalytic devices (Fig. 1.4), the photoelectrochemical (PEC) cell[1-2] and the so-called powdered device[14]. In a PEC cell device, the photocatalyst forms one of the two electronodes (e.g. a photo-anode in Fig. 1.4) while the other electronode is formed by a metal (e.g. platinum). The two electronodes are wired, so that the electrons and holes which are generated at one electronode, can travel to the cathode and anode, and activate the HER and OER respectively. In addition, a bias voltage can be applied to this device between the cathode and the anode. The bias voltage can shift the band edge positions of the photocatalyst relative to the water redox levels in the solution. By this way, materials with a band gap larger than 1.23 eV but unfavorable CB or VB positions may still achieve photocatalytic performances. However, applying a bias voltage consumes energy and thus reduces the efficiency of the device. Therefore, a large bias voltage should be avoided. For this reason, photocatalysts are still requited to have its CB and VB position close enough to the H_2/H_2O and O_2/H_2O level even a bias voltage can be applied.

In a powdered device, the photocatalyst in the powdered form are directly put into the solution. By some mechanisms of electron-hole separation such as p-n junctions[15-19], built-in electric fields[20-22], and so on, the exited electrons and holes can travel to different places at the photocatalyst-solution interface, where they activate the HER and OER respectively. The powdered device is simpler than the PEC cell device, and it is easy to be scaled up as it is not wired. Therefore, the powdered device has a good potential in practice. The disadvantage of this device is that no bias voltage can be applied on it, indicating that the requirement of the band edge position in Fig 1.2 should be strictly satisfied. In addition, unlike the PEC cell, the powdered device generates H_2 and O_2 at the same particles, so it requires a gas separation step which is non-trivial.

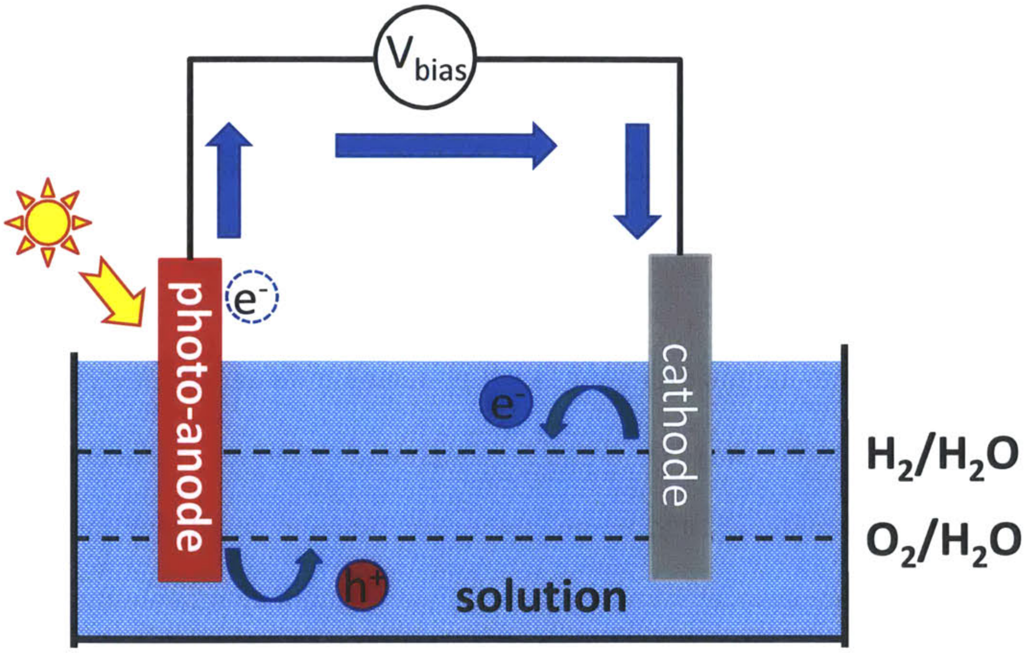

(a)

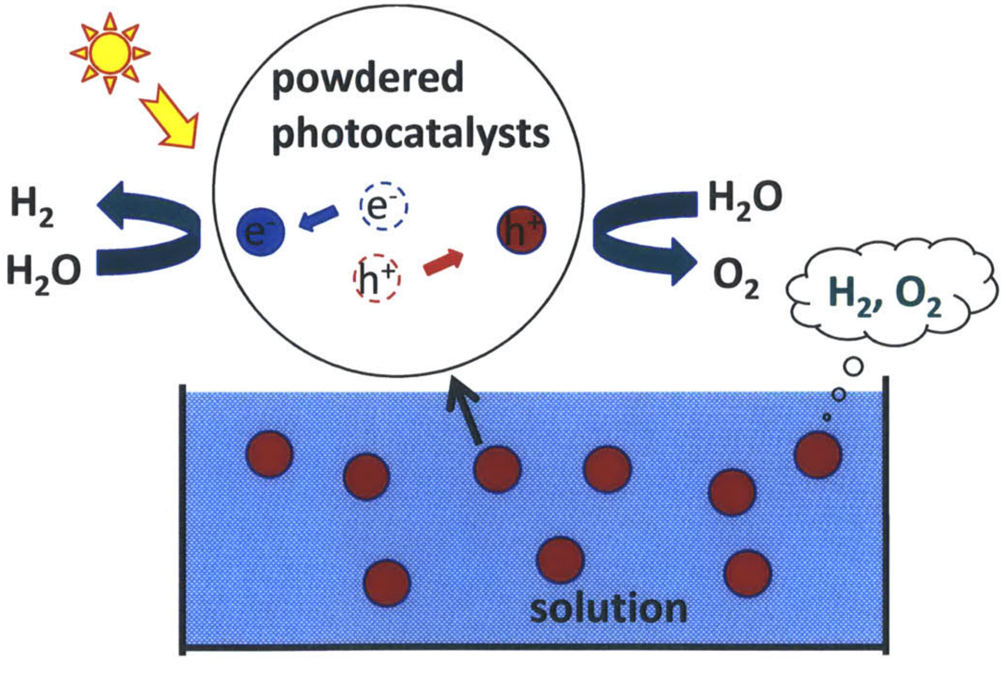

(b)

Figure 1.4 A schematic illustration of two types of photocatalytic devices. (a) PEC cell device; (b) powdered device.

1.1 Water-splitting photocatalysis as a technique to utilize the solar energy

Although the technique of photocatalysis has many interesting applications, such as water purification[23-26], artificial photo-synthesis[5-6, 12, 14, 21], photoelectrochemical CO_2 reduction[4, 8], and so on, the major interest in this thesis is to apply it to capture and store the solar energy by photo-catalyzing the water-splitting reaction[1-3, 14]. Indeed, at a power level of $1000W/m^2$, the solar energy incident on the earth's surface by far exceeds all human energy needs[1, 27]. Photovoltaic[28] and electrochemical solar cells[9, 28-29] that convert solar energy into electricity can reach up to 55% ~ 77% efficiency[30-32] but remain uneconomical because of high fabrication costs, insufficient light absorption[33] and inefficient charge transfer[28]. Photocatalysis, which directly converts solar energy into H_2-based chemical energy, may serve as an alternative way to utilize the solar spectrum[1-3, 14]. Currently, the primary objective in this field is to find photocatalyst materials which can achieve above ~10% energy conversion efficiency (ECE) without any bias voltage[1]. This is the performance that the US Department of Energy considers to be the minimum for commercialization[34].

Since the discovery of the first photocatalytic water-splitting system based on TiO_2 and Pt in 1972 by Fujishima and Honda[35-36], more than 130 inorganic materials have been demonstrated to exhibit photocatalytic performance for water-splitting[1]. However, under solar illumination, the efficiency of current photocatalytic devices is still well below the commercially viable level[1]. So far, the GaN:ZnO solid solution achieves the highest efficiency of any photocatalyst in pure water (pH = 7) and under visible light, with a quantum efficiency ~2.5%[1].

There are two major reasons for the low efficiency. One reason is the lack of low band gap photocatalysts. It is commonly known that the optimal range of band gap for absorbing the solar spectrum is 1.1 eV ~ 1.7 eV[37]. After considering multiple sources of efficiency loss in realistic conditions such as reflection loss, quantum-yield loss, absorption loss and collection loss, Refs. [38-39] concluded that a band gap around or less than 2.0 eV is necessary for a single material water-splitting system to reach a ECE level above ~10% under AM1.5 solar radiation. However, not many photocatalysts with a band gap around this level have been found. To solve this problem, new photocatalysts with a low band gap need to be identified. This is the major objective of this thesis.

The other reason is that the reaction rate of current water-splitting photocatalytic device is too low. The water-splitting reaction has very slow kinetics, as it is a process involving four electron/holes[1-2, 40]. The time from the generation of the electron-hole pairs to the activation of the HER and OER is significantly longer than the typical electron-hole lifetime in semiconductors[40-41]. Therefore, a large fraction of electrons and holes recombined with each other before going into the solution. To solve this problem, kinetic barrier of the water-splitting reaction at the interface should be reduced and the electron-hole lifetime should be enhanced. Besides to improve the photocatalysts, such as finding photocatalyst materials with better kinetic and transportation properties, growing purer compounds, increasing surface trapping states[42], forming p-n junctions[15-19], introducing innate electric fields[20-22] and so on, this purpose may be also achieved by searching and using good co-catalysts. Co-catalysts can often significantly reduce the reaction barrier and improve the water-splitting reaction rate. For instance, the rate of H_2 evolution reaction becomes ~100 times faster when 5 wt% Ru is added to TaON[43], and in the ZnO:GaN solid solution, both H_2 and O_2 evolution changed from negligible to clearly observable when 5 wt% RuO_2 was present[44]. It is noteworthy that the performance of co-catalysts is system dependent, and finding good co-catalysts for individual photocatalysts is an active research topic in this field as well, though it is not the main focus in this thesis.

1.2 Oxides, non-oxides, and oxynitrides as water-splitting photocatalysts

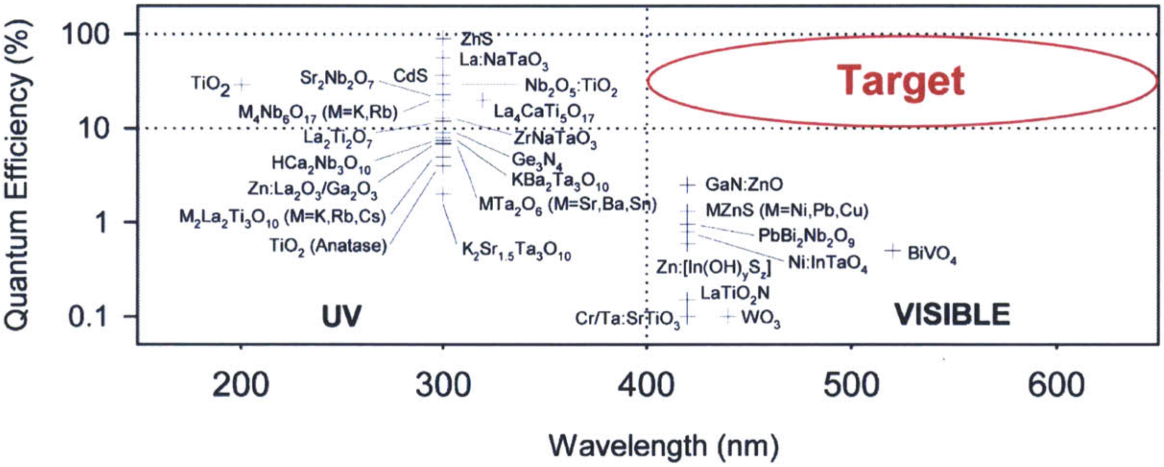

Figure 1.5 Quantum efficiency and band gap of some oxide photocatalysts*.

More than 130 inorganic materials have been demonstrated to exhibit photocatalytic performance for water-splitting over the last three decades, and over 80% of them are oxides[1]. This is primarily because oxides are the most well-studied chemistries, and

---

* Reprinted (adapted) from a website http://payneresearch.org/research/photo-electrochemical-pec-water-splitting/

many of them are stable in aqueous environment. Some of these oxide photocatalysts are summarized in Fig. 1.5. The figure shows two major trends of these oxides: (1) most of them contain d^0 or d^{10} cations; (2) most of them have a band gap larger than 2.7 eV(~ 450 nm), which is too high for achieving the commercially viable ECE level under solar illumination. The primary reason for the large band gap of these oxide photocatalysts is that their VB is typically dominated by O_{2p} states which are about 3 eV lower than the H_2/H_2O level[3]. This gives a lower bound roughly 3 eV to the band gap of the oxide photocatalysts, since the CB of photocatalysts needs to be above or close to the H_2/H_2O level. As a result, to achieve a lower band gap, the VB position of the oxide photocatalysts must be raised.

There are mainly two strategies to reduce the band gap of these oxide photocatalysts. The first strategy is to dope other cations or anions into the oxides. Different cations and anions have been studied by first principles computations as possible dopants into the photacatalytic system. For instance, cations (V[45], Mn[46], Fe[46], Co[47] and so on) or anions (C[48], N[49-50], P[51], S[51] and so on) doping and some co-doping strategy (doping cations and anions simultaneously)[52-54] have been studied by Density Functional Theory (DFT)[55-56] for TiO_2, the earliest experimentally demonstrated photocatalyst[35-36]. Similar studies have also been performed for other photocatalysts such as ZnO[57-58], WO_3[59], $SrTiO_3$[60-61] and so on. To generally summarize these studies, cation doping exhibits very limited band gap reduction, while anion doping or co-doping sometimes significantly reduce the band gap. This is because that the cation doping usually has little effect on the VB position of the oxide materials while the anion doping may sometimes raise the VB position significantly. However, doping anions into oxides are very challenging in practice.

The other strategy is to form solid solutions. Due to band bowing effects[62-63], solid solutions can have a lower band gap than both of their end members. For example, the GaN:ZnO solid solution has a band gap of 2.4 ~ 2.8 eV, while both GaN and ZnO have a band gap larger than 3.0 eV[3]. Following this strategy, one may form solid solutions of two or more photocatalysts with a same crystal structure and obtain new photocatalysts which have a lower band gap than both of their end members. More detail of this point will be presented in Chapter IV.

Besides to improve the oxide photocatalysts, one may also find photocatalysts with a low band gap in other chemistries. For instance, nitrides and sulfides may have a higher VB compared to oxides, since their VB are typically dominated by N_{2p} and S_{3p} states, which are higher in energy than the O_{2p} states. In fact, a few nitride compounds such as Ta_3N_5[64-65], GaN[44], Ge_3N_4[66] and so on have been experimentally demonstrated as water-splitting photocatalysts. Some of them indeed have a low band gap (e.g. Ta_3N_5, ~2.1 eV[64-65]). The potential problem of these materials is that they are usually less stable than oxides in aqueous environment[3]. This limits their commercial exploitation as water-splitting photocatalysts.

As a balance of the band gap and the aqueous stability, oxynitrides have been recently proposed as a promising chemical space for low band gap photocatalysts[3]. They usually have a VB dominated by a mixture of O_{2p} and N_{2p} states, which is typically higher in energy than the VB of pure oxides[3]. In the meantime, they are often more stable in aqueous environment compared to pure nitrides[3]. Following this idea, experimentalists have identified a few oxynitrides compounds as water-splitting photocatalysts with a low band gap, such as TaON (2.5eV)[3], $SrTaO_2N$ (2.1 eV)[67], $BaTaO_2N$ (1.9 eV)[67], $CaTaO_2N$ (2.4 eV) $LaTiO_2N$ (2.0 eV)[68], $Ca_{0.25}La_{0.75}TiO_{2.25}N_{0.75}$ (2.0 eV)[68], $LaTaO_2N$ (2.0 eV)[69] and $CaNbO_2N$ (1.9 eV)[69]. In this thesis, we use first principles computational approaches such as high throughput screening[70-73] to identify new oxynitride compounds as promising photocatalysts.

1.3 Design of new photocatalysts by first principles high throughput screening

Although theorists and experimentalists have put a lot of efforts in this field and have harvested fruitful results, the ECE of the currently known photocatalysts are still well below the commercially viable level (~10%)[1]. This spurs us to continue to identify new photocatalysts with better potentials by both experimental and computational approaches.

High throughput computational screening whereby one computationally assesses key properties of a large number of compounds for a given application has shown its merit in many fields, such as the design of new battery materials[74-77], thermoelectric materials[78-79], piezoelectric materials[80], and organic photovoltaic materials[81-83]. The development of ab-initio property prediction methods and their automation makes it possible to examine thousands of material candidates for a few desired properties[84-85].

In order to apply this technique to identify new water-splitting photocatalysts, one should first determine which properties are the identifiers for photocatalyst materials. We have mentioned earlier that water-splitting photocatalysts for solar applications should have the following properties[1-2]: (1) they should be thermodynamically stable enough so that they can be synthesized; (2) they should have a band gap that suitable for absorbing solar spectrum; (3) their CB should be higher than the H_2/H_2O level while their VB should be lower than the O_2/H_2O level (this requirement can be slightly loosen in a PEC cell device which allows to apply a bias voltage); (4) they should be stable in aqueous environment; (5) they should have fast and selective kinetics for water-splitting reaction; (6) they should have good transportation properties and a long electron-hole lifetime; (7) they should be inexpensive to manufacture.

Apparently it is not practical to consider all these properties in the high throughput computational screening. Computational predictions on some properties, such as kinetics properties and transportation properties are still too computationally expensive and not stable enough to be handled in a high throughput manner. In fact, we have considered only the first three properties (i.e. the phase stability, the band gap, and the band edge positions in solution) in the high throughput screening in this thesis. The methods and the results of the screening will be explained in detail in Chapter II and Chapter III. For other properties, it may be better to investigate them in individual systems after new candidates have been identified from the high throughput screening.

1.4 Motivation and overview of this thesis

Material problem is the core problem in the field of photocatalysis and is the key to achieve high-efficiency water-splitting photocatalysis under solar illumination. To solve this problem, new photocatalyst materials with better properties need to be designed. In this thesis, we present our work on designing new water-splitting photocatalysts by first principles computations.

We mainly use the high throughput computational screening technique and focus on the three key properties of photocatalysts, the phase stability, the band gap, and the band edge positions in solution. The computational methods that are used in the high throughput screening system to predict these properties should be accurate, stable, and computationally inexpensive. For predicting the phase stability and the band gap, such methods are available as the convex hull construction method[86] and the Δ-sol method[87] which will be further introduced in Chapter III. However, methods that predict the CB and VB position of a semiconductor vs. the water redox levels are not satisfactory in either accuracy or computational cost. To solve this problem, we have developed a first principles computational method, the so-called three-step method[11]. It can predict the relative band edge positions of a semiconductor (i.e. the distance of the CB vs. the H_2/H_2O level and the distance of the VB vs. the O_2/H_2O level) with an acceptable computational cost. More importantly, the method takes the effect of the aqueous environment into account and thus significantly improved the accuracy of the results[11]. We will explain the method in detail in Chapter II.

By integrating the convex hull construction method[86], the Δ-sol method[87] and the three-step method[11], we construct the high throughput screening system for identifying new water-splitting photocatalysts. We implement this screening system mainly on oxynitride chemical space, as the reason we mentioned in Section 1.2. We have screened 2948 different candidate compounds including 68 binary nitrides, 1503 ternary oxynitrides and 1377 quaternary oxynitrides. The screening has reproduced most of the known water-splitting photocatalysts and has also found sixteen new promising candidates. Both the algorithms and the results of the screening will be presented in detail in Chapter III.

$Ti_3O_3N_2$, one of the identified candidates from the high-throughput screening, is particularly interesting. Computational results indicate that it can likely be synthesized[71]. In fact, it is recently declared to have been synthesized from a website[88]. Its CB and VB are predicted to be bracketing the water redox levels[71], indicating that it may activate both the H_2 and O_2 evolution reaction without any bias voltage. Its band gap is predicted to be 2.37 eV, which is in the visible light region. In addition, we find that it has the same crystal structure as Ta_3N_5, which is also a photocatalysts with a low band gap. This inspires us to study the solid solution of these two materials, because that by forming the solid solution, we may obtain a material with a lower band gap than both of the end members. Using first principles computations, we have shown that the solid solution of Ta_3N_5 and $Ti_3O_3N_2$ can likely be synthesized and remain stable. The lowest band gap of the solid solution is predicted to be around 2.0 eV at a composition around 50%:50%. Therefore, a band gap reduction of ~0.2 eV is achieved by forming the Ta_3N_5:$Ti_3O_3N_2$ solid solution. More details of this work will be provided in Chapter IV.

Chapter II. Prediction of semiconductor band edge positions in aqueous environments from first principles

In this chapter, we present a novel first principles method, the so-called three-step method[11], which computes the CB position of semiconductors relative to the water H_2/H_2O level using DFT[55-56] with semi-local functional[89-90] and classical molecular dynamics (MD). We test the method on some photocatalyst materials which have their band edge positions measured in experiments. The predicted band edge positions are within 0.34 eV of the experimental data, with a mean absolute error of 0.19 eV[11]. Both the accuracy and the computational cost of the method are acceptable for the application of the first principles high throughput screening. Therefore, we integrate this method into the high throughput screening system in Chapter III.

2.1 Introduction

As was shown in Fig. 1.2, one crucial requirement for a water-splitting photocatalyst material is that its CB should be higher than the H_2/H_2O level of water and its VB should be lower than the O_2/H_2O level. This requirement ensures that the water-splitting reaction is energetically favorable without a bias voltage. Therefore, the knowledge of a semiconductor's CB and VB band edge positions, relative to the H_2/H_2O level and the O_2/H_2O level in solution respectively, is important for the design of a water-splitting photocatalyst[9-11]. An *ab initio* approach to obtain such band edge positions is preferred as it can be used as a scalable approach to investigate a large number of possible materials.

A straightforward attempt for this purpose is to compute both band edge positions of semiconductors and water redox levels, relate them to a common reference, and then calculate their difference. The vacuum level is a natural candidate for the common reference. The band levels of semiconductors and the water redox levels relative to the vacuum level have been respectively computed using DFT in Refs. [91-92]. However, the problem comes from the fact that the band realignment at a semiconductor-water interface is not equal to the difference between the band realignment at the semiconductor-vacuum and water-vacuum surfaces. This difficulty is explained in Ref. [93] for the metal-semiconductor interfacial system. The main reason is that the dipole at metal-semiconductor interface is not equal to the difference between the surface dipoles at the metal-vacuum and semiconductor-vacuum surfaces. For the semiconductor-water interfacial system, we will show later in the Section 2.4 that the error due to this problem is up to 0.7 eV.

Apart from this approach, a few other computational methods have also been proposed in the literature. In Ref. [94], hydrogen levels in semiconductors and insulators have been aligned by a valence-band offset method[95-96]. This method assigns the absolute energy scale by setting the CB of Si to the measured EA of Si, calculates the formation energies of interstitial $H^+/H/H^-$ species, and sets the Fermi-level position at the energy level at which the positive (with H^+) and negative (with H^-) charged states share the same energy as the hydrogen levels within the semiconductors and insulators. However, this method also avoids directly dealing with a semiconductor-water interface system and thus may have similar band alignment problems as the vacuum reference method. The mean absolute error of the method is around 0.4 eV.

A method which directly deals with the semiconductor-water system was developed in Ref. [97]. In the paper, the authors computed the band edge positions of TiO_2 relative to water redox levels, using the generalized gradient approximation (GGA)[90] and *ab initio* MD. In principle, the method can be generalized to compute the band edge positions of other inorganic semiconductors too. However, the errors for TiO_2's CB and VB positions found by the method were substantial, at respectively 0.4 eV and 1.6 eV[97]. They argue that the error may come from the simplified assumption that the zero-point energy (ZPE) of a proton in a solvated H_3O^+ ion can be approximated by the net ZPE of a dummy proton in an isolated pseudo H_3O molecule, a molecule with the same atomic configuration as an isolated H_3O^+ ion but with neutral charge[98]. Since the ZPE is directly added to their results and is as large as 0.5 eV, the assumption may introduce significant errors.

Compared to the methods mentioned above, the first principles method presented in this chapter, which computes the CB position of a semiconductor relative to the H_2/H_2O level in solution, has the following advantages: (1) it is applicable for general inorganic semiconductors; (2) it directly deals with band realignment effects introduced by the semiconductor-water interface; (3) it is mainly based on total energy calculations using DFT-GGA, with reasonably low computation cost.

In fact, an approach for the computation of band edge alignments across a solid-solid interface has previously been developed. The band alignment between two semiconductors[99-100], and the Schottky barrier heights between a semiconductor and a metal[101], are typically computed with DFT by three sub calculations, two bulk calculations to compute the difference between the target energy level (CB, VB or Fermi energy) and the average Hartree potential of each solid, and an interfacial slab computation to compute the Hartree potential difference between the two solids.

There are several challenges when replacing one solid system by liquid water. Since liquid water lacks periodicity, and *ab initio* MD can produce considerable errors for water[102-103], it is non-trivial to construct a cell with accurately representative atomic configurations of liquid water in DFT. Instead, we use the idea proposed in Ref. [104] and equilibrate a classical MD computation of water at room temperature. Snapshots of the water configuration at different MD time points are then computed with DFT.

By combining the band alignment method for solid-solid system and the idea of using snapshots of classical MD water configurations for DFT, we develop a so-called three-step method for computing CB band edge position relative to the H_2/H_2O level. In the next sections, we introduce our methodology in detail, and present the computational results obtained with this approach for six common water-splitting photocatalyst materials, TiO_2, WO_3, CdS, ZnSe, GaAs and GaP. Finally, we compare the computational results to experimental data.

2.2 Methodology development

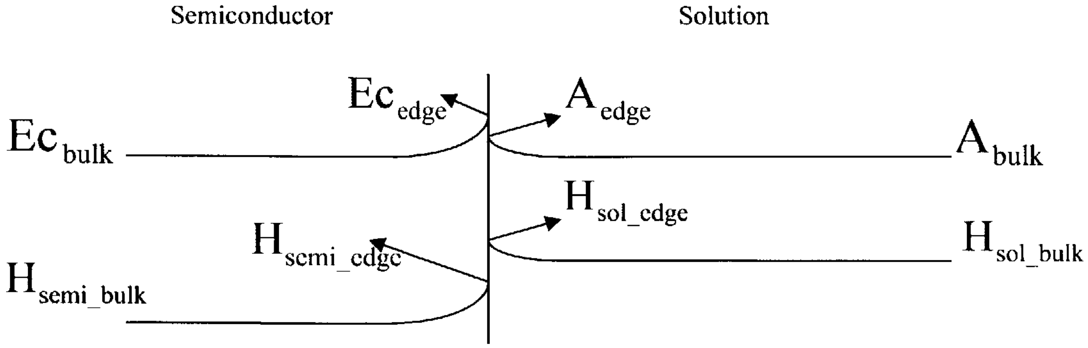

Figure 2.1 A schematic diagram of the band alignment at the semiconductor-water interface. Ec_{bulk} = CB in the bulk of the semiconductor; Ec_{edge} = CB at semiconductor-solution interface; A_{bulk} = Acceptor level (H_2/H_2O level of liquid water in this work) in the bulk of the solution; A_{edge} = Acceptor level at the semiconductor-solution interface; H_{semi_bulk} = Hartree potential in the semiconductor bulk; H_{semi_edge} = Hartree potential on the semiconductor side at the semiconductor-solution interface; H_{sol_bulk} = Hartree potential in the bulk of the solution; H_{sol_edge} = Hartree potential on the solution side at the semiconductor-solution interface

$$Ec_{edge} - H_{semi\_edge} = Ec_{bulk} - H_{semi\_bulk} \tag{2.1}$$

$$A_{edge} - H_{sol\_edge} = A_{bulk} - H_{sol\_bulk} \tag{2.2}$$

$$\begin{aligned} & Ec_{edge} - A_{edge} \\ & = (Ec_{edge} - H_{semi\_edge}) - (A_{edge} - H_{sol\_edge}) + (H_{semi\_edge} - H_{sol\_edge}) \\ & = (Ec_{bulk} - H_{semi\_bulk}) - (A_{bulk} - H_{sol\_bulk}) + (H_{semi\_edge} - H_{sol\_edge}) \end{aligned} \tag{2.3}$$

Fig. 2.1 shows a schematic diagram of band alignments at an interface, and introduces the terminology we will be using. Our objective is to compute the CB band edge position relative to the solution acceptor level (H_2/H_2O level of liquid water in this work) at the interface, i.e. $Ec_{edge} - A_{edge}$. We assume that the band alignment is due to electrostatic effects (electrons and ions redistribution near the interface due to Fermi energy realignment). So the energy levels and Hartree potential change by the same amount everywhere in space and their difference remains unchanged. Thus, we obtain Eqn. 2.1 and Eqn. 2.2. Therefore, the term $Ec_{edge} - A_{edge}$ can be computed by Eqn. 2.3.

Eqn. 2.3 indicates that the term $Ec_{edge} - A_{edge}$ can be obtained by the following three-step method. Step 1: compute the term $Ec_{bulk} - H_{semi\_bulk}$, i.e. the eigenvalue of the lowest unoccupied eigenstate relative to the average Hartree potential, in a bulk semiconductor system. Step 2: compute the term $A_{bulk} - H_{sol\_bulk}$, i.e. the eigenvalue of the molecular acceptor level relative to the average Hartree potential, in a bulk liquid water system. This is non-trivial and we adopt the idea of using MD atomic configurations for DFT. More details will be introduced in Section 2.3. Step 3: compute the term $H_{semi\_edge} - H_{sol\_edge}$, i.e. the difference in average Hartree potentials between the semiconductor vs. the liquid water, in a semiconductor-water interfacial slab system. During step 3, we join the bulk cells that we compute in steps 1 and 2 and make a supercell which contains the interface. In this supercell, we compute the variation of the Hartree potential with position. By averaging the Hartree potential on both the semiconductor side and liquid water side, we calculate $H_{semi\_edge} - H_{sol\_edge}$.

This method has two key features. One is that it includes the band realignment effect yet avoids a large supercell computation. The band realignment effect at the semiconductor-water interface is important for computing the relative energy levels. However, it usually occurs over a distance of 100Å to several micro meters from the interface[104]. As a consequence, directly computing the band alignment effect, i.e. the term $Ec_{edge} - Ec_{bulk}$

(or $A_{edge} - A_{bulk}$), in a single slab computation is not applicable, since it requires a prohibitively large supercell to converge both Ec_{edge} (A_{edge}) and Ec_{bulk} (A_{bulk}) in the same system. On the other hand, in the three-step method, the three objective terms, $Ec_{bulk} - H_{semi\_bulk}$, $A_{bulk} - H_{sol\_bulk}$, and $H_{semi\_edge} - H_{sol\_edge}$, are either pure bulk properties or pure interface properties, so a large supercell is not required. In this approach, the band realignment effect is captured by the computation of $H_{semi\_edge} - H_{sol\_edge}$. And the longest dimension of the supercell required to converge $H_{semi\_edge} - H_{sol\_edge}$ to 0.1 eV is typically 30Å to 40Å. The other important feature is that the three-step method only requires the Hartree potential in the interfacial slab computation but not any energy eigenvalues. This prevents the complicated problem of trying to assign electronic states to specific real space domains of the supercell.

2.3 Computational details and results

To test our approach, we select six popular photocatalyst materials: TiO_2, WO_3, CdS, ZnSe, GaAs and GaP. The details of their crystal structures are listed in Table 2.1. We applied the method described in Section 2.2 on these materials to compute their CB position relative to the H_2/H_2O level in liquid water, $Ec_{edge} - A_{edge}$. The computational results are compared to experimental data obtained from Refs. [105-106]. All DFT computations[55-56] are performed with projector augmented wave (PAW)[89] potentials using the plane-wave code Vienna Ab-initio Simulation Package (VASP)[107-108]. We use the Perdew-Burke-Ernzerhof (PBE)[90] GGA exchange-correlation functional unless specified otherwise.

semiconductor	TiO_2	WO_3	CdS	ZnSe	GaAs	GaP
Crystal type	Rutile (tetragonal)	Tetragonal	Wurtzite (hexagonal)	Zincblende (cubic)	Zincblende (cubic)	Zincblende (cubic)
Space group number	136	113	186	216	216	216
Space group name	P42/mnm	P421m	P63mc	F43m	F43m	F43m
Initial lattice parameters (Å)	a=4.598 b=4.598 c=2.956	a=7.616 b=7.616 c=3.960	a=4.137 b=4.137 c=6.714	a=5.670	a=5.654	a=5.447

Table 2.1 Crystal structure information for test materials.

2.3.1 Semiconductor bulk computation

To implement step 1 in Section 2.2, we compute the bulk CB relative to average Hartree potential for each selected material in this section. For every material, we optimize the volume, cell shape and atomic positions of the unit cell with a Monkhorst-Pack[109] 6×6×6 k-point grid and plane wave energy cutoff of 500 eV. On the optimized structures, we perform static DFT computations using a fine Γ-centered 10×10×10 k-point grid to compute the CB. We also plot the Hartree potential and determine a macroscopic average over the unit cell for every material. The resulting average Hartree potential H_{semi_bulk} is zero. This is consistent with the fact that the absolute Hartree potential in an infinite periodic system is customarily set to zero in DFT codes including VASP. The results of $Ec_{bulk} - H_{semi\_bulk}$ are show in Table 2.2.

Testing semiconductor	TiO_2	WO_3	CdS	ZnSe	GaAs	GaP
$Ec_{bulk} - H_{semi\_bulk}$ (eV)	3.77	1.89	2.91	3.25	3.64	4.08

Table 2.2 Values of $Ec_{bulk} - H_{semi\_bulk}$ from semiconductor bulk computations.

2.3.2 Liquid water bulk computation

Step 2 in Section 2.2 consists of determining the H_2/H_2O acceptor level relative to the Hartree potential in bulk liquid water. To prepare the water atomic configurations in DFT, we perform a classical MD computation by DLPOLY[110] and use the TIP4P[111] potential to describe the interaction between water molecules. A water system of 128 H_2O molecules is initially equilibrated at 300K with a relaxed cell size of 18Å × 15.6Å × 14.6Å. At the same temperature, we further perform an NVT MD simulation for 100 ps and take snapshots of the atomic configurations of this TIP4P water system at t = 50ps and t = 100ps. We construct two DFT cells using these two configurations.

Before proceeding, we perform two tests to verify that atomic configurations from classical MD produce consistent results in terms of DFT electronic structures. Only the Γ k-point is used in the DFT calculations of liquid water cells. First, we compute the band gap and plot in Figs. 3a and 3b the density of state (DOS) by DFT using each of the two cells obtained at different MD time points without any further DFT ionic relaxations. The similar band gap values (3.76 eV and 3.89 eV) and similar DOS plots between Fig. 2.2a and Fig. 2.2b indicate that the atomic configurations taken from different time points of classical MD give little difference in the DFT electronic structures. Second, we repeat the process but with full DFT ionic relaxations (cell volume, cell shape, and atomic positions) for the t = 100ps configuration, and the resulting DOS is shown in Fig. 2.2c. The identical band gap values and similar DOS plots between Fig. 2.2b and Fig. 2.2c indicate that DFT ionic relaxations do not alter the electronic structures after the liquid water system reaches equilibrium in classical MD. In addition, all DOS plots in Figs. 2.2a, 2.2b, and 2.2c are very similar to the DOS plots of liquid water in Ref. [104], which implies that the Γ k-point alone is sufficient to give results consistent with previous work.

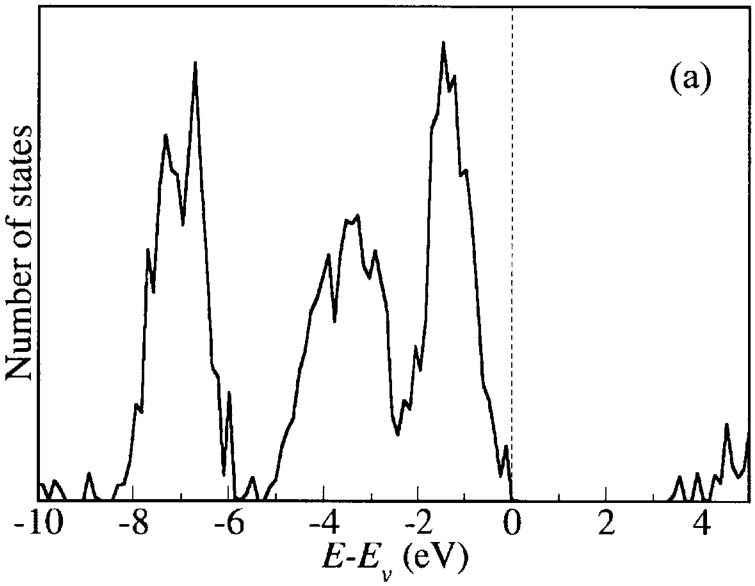

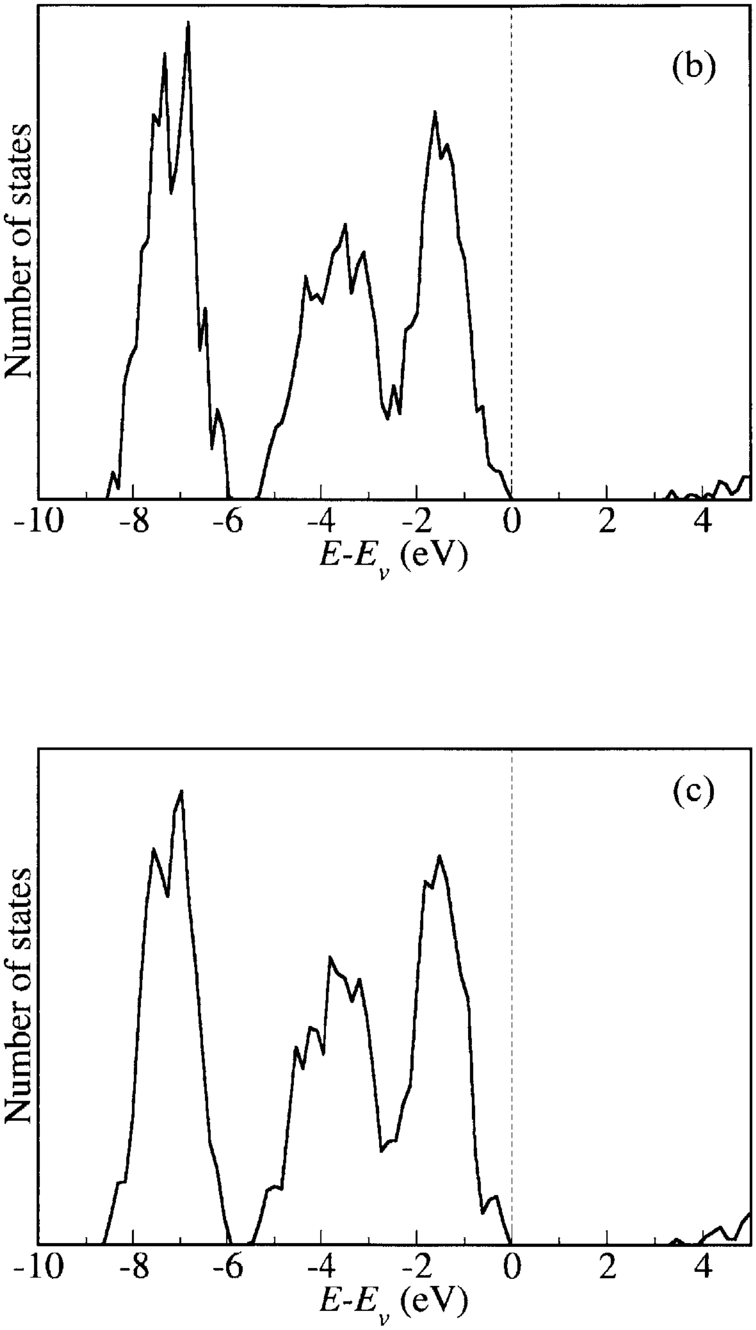

Figure 2.2 Total DOS plots for (a) a 128 H_2O molecules liquid system with MD atomic configurations at t = 50 ps without DFT relaxation, with a band gap of 3.76 eV; (b) a 128 H_2O molecules liquid system with MD atomic configurations at t = 100 ps without DFT relaxation, with a band gap of 3.89 eV; (c) a 128 H_2O molecules liquid system with MD atomic configurations at t = 100 ps with DFT relaxations, with a band gap of 3.89 eV. E_v in the x-axis labels is the VB energy eigenvalue.

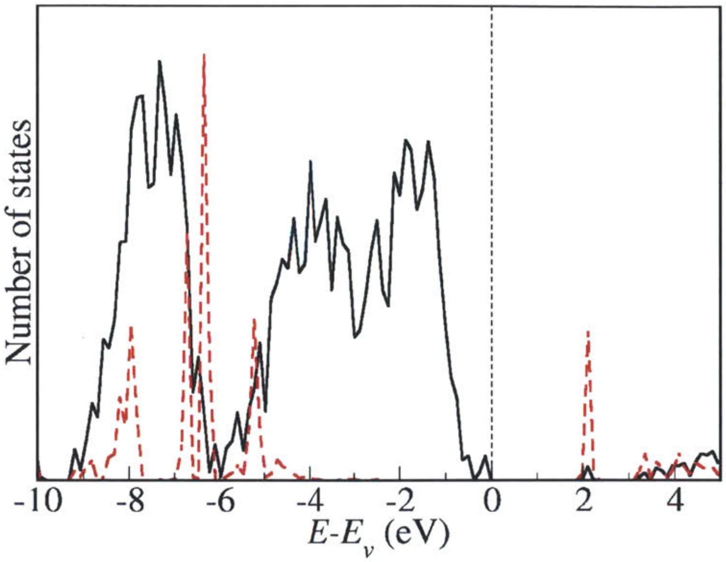

Figure 2.3 DOS plots for a $127H_2O + H_3O^+$ liquid system. The black solid line is the total DOS while the red dashed line is the projected DOS from the H_3O^+ ion in this system. We enlarged the H_3O^+ DOS 30 times to make it visible on the scale of the total DOS. The DOS peak at approximately 2.0 eV represents the LUMO of the system contributed by the H_3O^+ ion. E_v in the x-axis labels is the VB energy eigenvalue.

In order to compute the term $A_{bulk} - H_{sol\_bulk}$, we need to compute the lowest unoccupied molecular orbit (LUMO) level of water because this level is recognized as the acceptor level of water. While the acceptor is nominally the proton (H^+), in an aqueous environment the H^+ is solvated in multiple $H^+(H_2O)_n$ configurations[112]. The hydronium ion H_3O^+, being the simplest, is especially important for computing the acceptor level in water system. We simulated the hydronium ion in water by fully relaxing an isolated H_3O^+ ion in DFT and then replacing one of the 128 H_2O molecules in the liquid water system with this H_3O^+ ion. The O atom of the H_3O^+ is placed in exactly the same position as the O atom of the replaced H_2O molecule. The orientation of the added H_3O^+ ion is randomized. We perform further DFT relaxation for this added H_3O^+ ion in order to optimize the atomic positions and orientation in the water system. A static DFT computation then follows to compute the energy levels of this $127H_2O + H_3O^+$ system. The DOS plot of such a system is shown in Fig. 2.3, which indicates that a level attributed to H_3O^+ is indeed the LUMO. We repeat the above process several times but replace a different H_2O molecule with H_3O^+ to ensure that our results are not affected by the positions of the H_3O^+ ions in the system. The results are shown in Table 2.3.

Replaced H_2O molecule	1	2	3	4
$A_{bulk} - H_{sol\_bulk}$ (eV)	-0.70	-0.65	-0.62	-0.75
Total energy (eV)	-1788.2	-1788.1	-1787.5	-1787.7

Table 2.3 Values of $A_{bulk} - H_{sol\_bulk}$ from liquid water bulk computations.

Table 2.3 indicates that the fluctuation in $A_{bulk} - H_{sol\_bulk}$ due to the position of H_3O^+ ion in the cell is less than 0.1 eV. We will use $A_{bulk} - H_{sol\_bulk} = -0.70eV$ in subsequent calculation since it corresponds to the lowest total energy among all four systems.

2.3.3 Semiconductor-water interface computation

This section describes how the semiconductor-water interface calculation (step 3 in Section 2.2) is implemented. We aim to compute the Hartree potential difference between the semiconductor bulk cell and the liquid water cell in an interfacial slab system. The interfacial cell is constructed by joining several layers of the semiconductor bulk cells in Section 2.3.1 and the liquid water cell in Section 2.3.2 together. For each semiconductor, we perform a convergence test in that we increase the number of layers of semiconductor cells until the Hartree potential difference between the semiconductor side and liquid water side is converged to 0.1 eV. The converged Hartree potential profile along the slab direction for TiO_2 is shown in Fig. 2.4 as an example. The calculated value of $H_{semi\_edge} - H_{sol\_edge}$ for each test compound is listed in Table 2.4. Only the Γ k-point is used for these DFT computations.

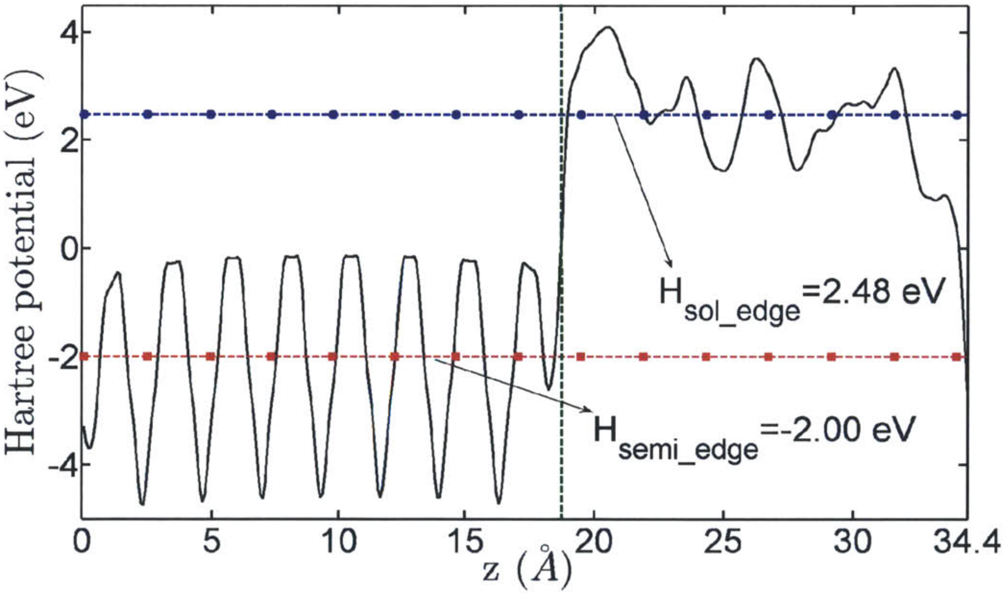

Figure 2.4 Calculated Hartree potential profile of a stoichiometric TiO_2-water slab system. The vertical green dashed line indicates the interface. The left side is semiconductor TiO_2 and right side is water. The black solid line is the planar-averaged Hartree potential as a function of cell dimension normal to the interface. The red dashed line with square makers indicates the planar-averaged Hartree potential of TiO_2, H_{semi_edge}. The blue dashed line with circular makers indicates the planar-averaged Hartree potential of liquid water, H_{sol_edge}.

Testing semiconductor	TiO_2	WO_3	CdS	ZnSe	GaAs	GaP
H_{semi_edge}	-2.00	-1.11	-1.02	-1.05	-1.41	-1.56
H_{sol_edge}	2.48	2.02	1.33	1.30	1.86	1.93
$H_{semi\_edge} - H_{sol\_edge}$	-4.48	-3.13	-2.35	-2.35	-3.27	-3.49

Table 2.4 Values of $H_{semi\_edge} - H_{sol\_edge}$ from interfacial slab computations.

2.3.4 Results of CB edge positions relative to water H_2/H_2O level

By substituting the terms $Ec_{bulk} - H_{semi\_bulk}$, $A_{bulk} - H_{sol\_bulk}$ and $H_{semi\_edge} - H_{sol\_edge}$ into Eqn. 3, we obtain the CB band edge position results relative to water H_2/H_2O level: $Ec_{edge} - A_{edge}$. In Table 2.5, we compare the computed results with experimental data in a pH = 1 electrolyte from Refs. [105-106]. Note that our system is a $127H_2O + H_3O^+$ system, so it is comparable to the pH = 1 electrolyte in terms of H^+ concentration. Fig. 2.5 is plotted from the data in Table 2.5 and shows more directly the relationship between computed $Ec_{edge} - A_{edge}$ and experimental data.

Test semiconductor	TiO_2	WO_3	CdS	ZnSe	GaAs	GaP
$Ec_{edge} - A_{edge}$ (eV)	-0.01	-0.54	1.27	1.60	1.07	1.29
$-e \times V_{NHE}$ (experimental, eV)	0.00	-0.20	1.50	1.50	0.80	1.10

Table 2.5 Computational results of Ec_{edge} - A_{edge} and comparison with experimental data. The experimental data is translated from V_{NHE}, the value reference to Normal Hydrogen Electrode (NHE), to Ec_{edge} - A_{edge} by using $Ec_{edge} - A_{edge} = -e \times V_{NHE}$

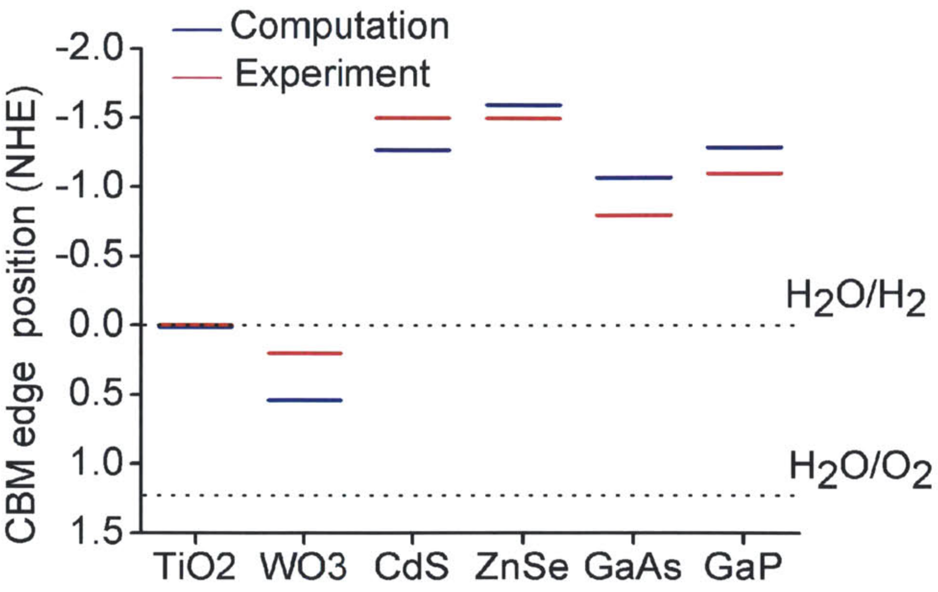

Figure 2.5 CB band edge level results referenced to the NHE. Blue lines are computational results by the method developed in this chapter. Red lines are experimental data from Refs. [105-106]. Two dotted lines indicate the H_2/H_2O and O_2/H_2O levels in water.

2.4 Discussion

	$Ec_{bulk} - H_{semi\_bulk}$	$A_{bulk} - H_{sol\_bulk}$	$H_{semi\_edge} - H_{sol\_edge}$	$Ec_{edge} - A_{edge}$
WO_3 (eV)	2.35	-0.70	-3.39	-0.34

Table 2.6 Computational results of $Ec_{edge} - A_{edge}$ using GGA+U for WO_3.

From both Fig. 2.5 and Table 2.5, we see that our computational results are consistent with experimental data. The WO_3 system shows the largest error. To test whether this error is related to the *d*-character of WO_3's CB, we repeat the computations for WO_3 using the GGA+U approximation[113] with U = 2.0 for the *d*-orbitals of W. The result, shown in Table 2.6, indicates that $Ec_{edge} - A_{edge}$ changes from -0.54 eV to -0.34 eV after applying the +U correction and shows better agreement with the experimental value of -0.20 eV.

As is well known, DFT in the GGA approximation gives large errors for band gaps. However, our results for $Ec_{edge} - A_{edge}$ in Table 2.5 give an average error of 0.19 eV. We believe that the electronic level difference is in better agreement with experiment than the band gap primarily due to two reasons. One is that the computational error for band gaps comes from both CB and VB computations while our approach does not involve VB computation, so that our results do not have the error from computing VB. The other reason is that, in our approach, we are computing the energy difference between CB and LUMO, two unoccupied energy levels. They are both typically underestimated in semi-local functional[114]. Therefore, error cancellation may occur in their difference.

Our approach can be generalized to also compute the VB band edge position relative to O_2/H_2O level in water. However, this may not be necessary if one has an accurate way of computing the band gap of the semiconductor, for example, using the *GW* approximation[115], hybrid or screened hybrid functional[116-120] or the Δ-sol[87] method. We can then determine the VB from the CB band edge position and the band gap.

We also demonstrate here that the relative band edge position at a semiconductor-water interface cannot be computed by the vacuum reference approach. We take GaP as an example. By using the same approach as in Section 2.3.3, we respectively compute the Hartree potential difference at the GaP-vacuum surface and the water-vacuum surface, and denoted them as $H_{semi\_edge} - H_{Vacuum\_edge}$ and $H_{sol\_edge} - H_{Vacuum\_edge}$ in Table 2.7. By subtracting them, we obtain $(H_{semi\_edge} - H_{sol\_edge})_{Vacuum\_approach}$, the Hartree potential difference at the GaP-water interface by the vacuum reference method. The result is -4.18 eV (See Table 2.7). The directly computed value of $H_{semi\_edge} - H_{sol\_edge}$ for the GaP-water interfacial system is -3.49 eV (See Table 2.4). The discrepancy of the two results indicates that the vacuum reference approach is not valid.

	$H_{semi\_edge} - H_{Vacuum\_edge}$	$H_{sol\_edge} - H_{Vacuum\_edge}$	$(H_{semi\_edge} - H_{sol\_edge})_{Vacuum\_approach}$
GaP (eV)	-7.82	-3.64	-4.18

Table 2.7 Result of $H_{semi\_edge} - H_{sol\_edge}$ by the vacuum common reference approach.

2.5 Conclusions

In this chapter, we present a method for computing CB band edge positions relative to the water H_2/H_2O level. The method is computationally efficient since it only involves DFT calculations with a semi-local functional. The average error, over the six compounds tested, is 0.19 eV, which makes this method useful for predicting and designing photocatalyst materials. This method and an accurate band gap DFT computation method together may provide improved knowledge of the energy levels and band gap for any photocatalyst material. Materials that are designed base on this knowledge will need little bias voltage and have a suitable band gap for photocatalysis of water-splitting. Moreover, for an arbitrary photocatalyst material, this method can tell us how large the external bias voltage should be applied in order to activate hydrogen evolution. This information is both an important reference for experimentalists and a clue for evaluating the stability in the electrolyte of the materials.

Chapter III. First principles high throughput screening of oxynitrides for water-splitting photocatalysts

In this chapter, we present the first principles high throughput screening system that we have constructed to search for new water-splitting photocatalysts. We use the system to screen through ~3000 nitrides and oxynitrides. Most of the known photocatalysts materials in the screened chemical space are reproduced. In addition, sixteen new materials are suggested by the screening approach as promising photocatalysts, including three binary nitrides, two ternary oxynitrides and eleven quaternary oxynitrides[71].

3.1 Introduction

In this chapter, we screen compounds using high throughput computational methods by focusing on three significant properties of water-splitting photocatalysts: (1) the crystal structure and its thermodynamic phase stability (versus competing solids and gases); (2) the band gap; (3) the conduction band (CB) and valence band (VB) edge positions relative to the H_2/H_2O and O_2/H_2O levels in solution. For each property, a first principles computational method has been developed which has a low enough computational cost but an adequate accuracy so that it can be used in a high throughput search. By integrating them, we thus design a three-tier high throughput screening system as following: (a) a phase stability screening to eliminate candidate compounds which are not stable enough to be synthesizable; (b) a band gap screening to eliminate all candidates with a too large or too small band gap; (c) a screening of band edge position in aqueous environment to eliminate candidates whose CB or VB position are not suitable for water-splitting. The details of the screening system are introduced in the Section 3.2.

Recently, Refs. [70, 72] computationally screened perovskite metal oxides and identified some new candidates for photocatalysts. The major differences between the screening approach in those papers and in this thesis are the following: (a) the authors in Refs. [70, 72] predicted the CB and VB positions by empirically estimating the middle of the gap using electronegativity of the atoms while we compute them directly from first principles in an aqueous environment; (b) they mainly focused on perovskite metal oxides while we consider a wider range of structures and different chemical spaces.

As the reasons we mentioned in Section 1.2, we choose oxynitrides as the major chemical space to implement the screening system in this work. We screened 2948 different candidate compounds including 68 binary nitrides, 1503 ternary oxynitrides and 1377 quaternary oxynitrides. Our algorithm picked out most of the known water-splitting photocatalysts and also found sixteen new promising candidates. Some new candidates are existing materials from the Inorganic Crystal Structure Database (ICSD)[121] but have not been reported as photocatalysts yet. And some candidates are unknown compounds which are predicted by our compound prediction tool[122]. The detailed results are shown in Section 3.3.

3.2 Construction of the screening system

Fig. 3.1 illustrates the high throughput screening approach in this chapter. All computations are based on DFT[55-56] and are performed with PAW[89] potentials using the plane-wave code VASP[107-108]. For computations in step 1 and 2 in Fig. 3.1, we use the PBE[90] GGA+U[113] exchange-correlation functional unless specified otherwise, with all parameters as in Ref. [84]. For computations in step 3, we use PBE GGA with all parameters as described in Chapter II as well as in Ref. [11].

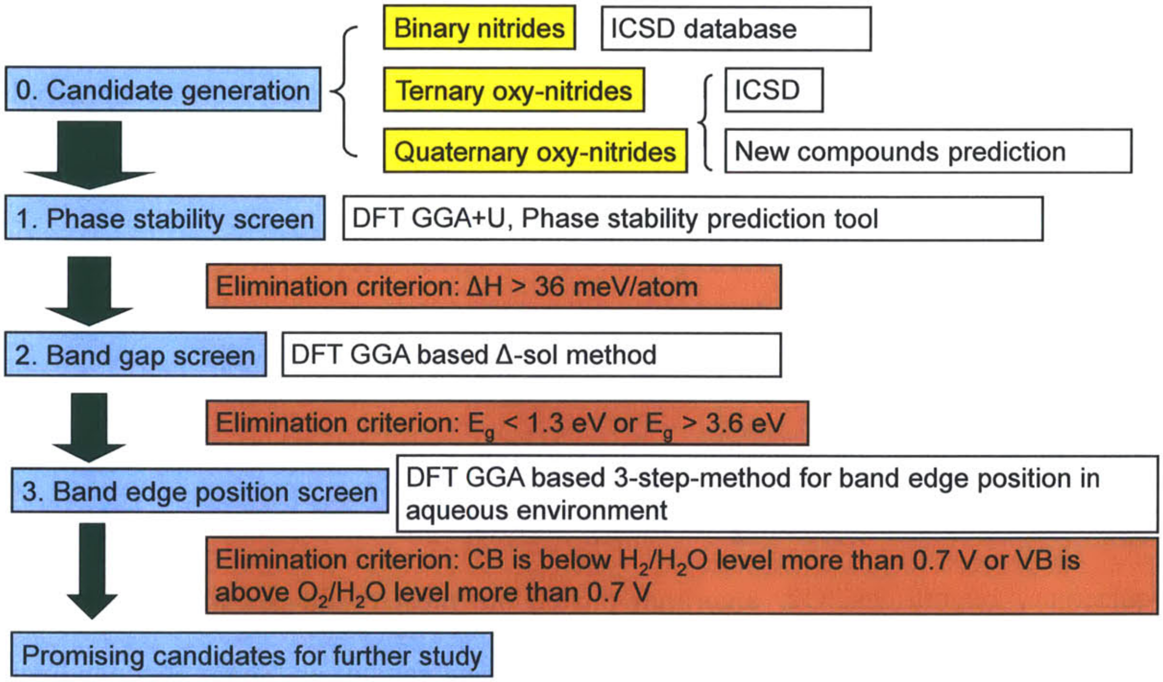

Figure 3.1 High throughput screening approach for water-splitting photocatalysts

3.2.0 Generation of the candidates

In this step, we generate the candidate compounds for the screening. As most known oxides photocatalysts contain d^{10} or d^0 cations[1, 3] (Fig. 1.5), we target primarily oxynitrides and only consider compounds that contains d^{10} cations (Ga^{3+}, In^{3+}, Ge^{4+}, Sn^{4+}, Sb^{5+}, and Bi^{5+}) or d^0 cations (Ti^{4+}, Zr^{4+}, Hf^{4+}, V^{5+}, Nb^{5+}, Ta^{5+}, Cr^{6+}, Mo^{6+}, W^{6+}, Sc^{3+}, and Y^{3+}).

One of the most complete databases of experimentally observed compounds is the ICSD[121]. However, there are very few oxynitrides available in the ICSD. For example, there are only 25 ternary oxynitrides and 118 quaternary oxynitrides which contain d^{10} or d^0 cations in the ICSD. Therefore, we use compound and structure prediction tools[122] to identify possible novel compounds. Since the oxynitrides space has not been as exhaustively searched with experiments as other chemistries (e.g. oxides), it is likely that there are a large number of novel compounds to be found. We used a previously developed approach based on ionic substitutions to propose new likely ternary and quaternary oxynitrides[122]. This approach uses information about the substitution probability of ions --- obtained by datamining all known crystalline compounds --- to come up with suggestions for novel compounds.

To generate novel ternary oxynitrides (M-O-N, with M being a d^0 or d^{10} cation), we used the set of all known binary ionic compounds as a starting point. Using the substitution algorithm from Ref. [122], we evaluated the likelihood that substituting the cation in each compound by M and the anion in the compound by a mixture of O and N would lead to a new stable compound. For instance, the algorithm suggested that the known Ta_3N_5 could have its cation Ta^{5+} substituted by Zr^{4+} and its anion N^{3-} by a mixture of O^{2-} and N^{3-}.

To generate new quaternary compounds (M1-M2-O-N with M1 or M2 being a d^0 or d^{10} cation), we only considered a list of known ternary oxides photocatalysts in Ref. [1] as the structural framework on which to perform the substitutions. For instance, $SrTiO_3$ could lead to a new candidate from substituting Sr^{2+} by La^{3+}, Ti^{4+} by Ta^{5+}, and O^{2-} by a mixture of N^{3-} and O^{2-} according to the probabilistic model in Ref. [122].

The amount of O and N to be substituted in each compound was determined by balancing the charge of the cations. There is however still a remaining degree of freedom in the exact ordering of O^{2-} and N^{3-} on the anion sites. We enumerated the different O^{2-}-N^{3-} orderings by using an algorithm similar to the one developed in Ref. [123] and selected the ones leading to the smaller cells and the larger number of N-N bonds, as the ordering of oxynitride anions has been recently shown to be driven by this factor[124]. For each candidate compound, we computed with DFT all selected orderings and only considered the one with lowest energy. It is worth noting that each possible compound also had to pass the stability screen in its relevant composition space (step 1 in Fig. 3.1) in order to be considered further.

Besides the oxynitrides, we included all binary nitrides M-N with M being a transition metal or semi-metal cation from the ICSD into the screening as well. Thus, in sum, we prepared 3 batches of candidate compounds, binary nitrides (M-N), ternary oxynitrides (M-O-N) and quaternary oxynitrides (M1-M2-O-N).

3.2.1 Phase stability screening

Phase stability is an essential component of high-throughput materials discovery as new proposed candidates need to be stable enough to be synthesizable. To assess if a compound is stable at zero K, we compared its energy versus the energy of other phases or their linear combinations. This can be technically achieved through the convex hull construction[86]. Not only does the convex hull construction indicate if a compound is stable versus competing phases but this construction can be used to assess how unstable a compound is. Therefore, we define the instability energy ΔH, in meV/atom, as the negative of the decomposition reaction energy to the stable phases. Stable compounds have an instability energy ΔH equal to zero and the larger the instability energy ΔH, the less stable the material is.

We performed this stability analysis for all compounds considered in this work. The possible competing phases were mainly obtained from the ICSD[121]. More details on the parameters used for the computations can be found in Ref. [84]. In addition, we used a recently developed scheme to mix GGA and GGA+U computations[125] as oxides and oxynitrides computations are usually performed with GGA+U while all nitrides have been computed with GGA.

In this screening, we eliminated all compounds with an instability energy ΔH larger than 36 meV/atom. We obtained this threshold energy by doing a brief analysis of the instability energy of compounds in the ICSD. We find that more than 80% of the ICSD compounds have an "instability energy ΔH" less than 36 meV/atom. Since the "ICSD compounds" have, in principle, all been synthesized, we consider this threshold to be reasonable to find compounds that can be made.

3.2.2 Band gap screening

In this step, we compute the band gap of the remaining candidates and eliminate those with unsuitable band gaps. Since the band gap computed from Kohn-Sham levels is usually lower than the experimental band gap by 30% ~ 100%[87], this approach cannot be used for band gap screening. Alternatively, we use the Δ-sol method[87] to determine the gaps. The Δ-sol method is motivated by the dielectric screening properties of the homogeneous electron gas, and determines the fundamental gap from DFT total energies of systems with an electron or a hole added within the screening radius of the material. Unreliable Kohn-Sham levels are not involved in the determination of the gap, and gross underestimation of band gaps is avoided. When tested across a large number of compounds with diverse chemistries, the Δ-sol method gives a mean absolute error of 0.2 eV for the gap[87]. In addition, the method requires three DFT total energy computations so it is acceptable in terms of computational cost. More detailed information is available in Ref. [87].

In this screening step, we eliminate all candidates with band gaps lower than 1.3 eV or higher than 3.6 eV. The theoretical lower limit of the band gap for a water-splitting photocatalyst is 1.23 eV[1-3] but an over-potential of 0.25 eV or more is usually required[38, 126-127]. Therefore, the lowest possible band gap in practice is around 1.5 eV. We further take the mean error of the Δ-sol method, around 0.2 eV, into account and finally set the lower threshold to 1.3 eV. The upper threshold is more flexible. For visible light absorption, 2.7 eV could be a good upper limit. However, we extend the upper limit to 3.6 eV to also capture any interesting oxynitride materials that absorb outside visible light region.

3.2.3 Screening of band edge positions in aqueous environment

In this step, we compute the CB and VB band edge positions in aqueous environment and compare them with the H_2/H_2O and O_2/H_2O levels in water. We used the earlier developed three-step method[11]. Since the method has been presented in detail in Chapter II, we do not reiterate it here. When tested on six typical photocatalysts, the method gives a mean absolute error of 0.19 eV for the CB position relative to the H_2/H_2O level in solution. It is worth to note that, once we obtain the CB position relative to H_2/H_2O level in water, it is straight forward to obtain the VB position relative to O_2/H_2O level since the band gap has been computed in the previous step.

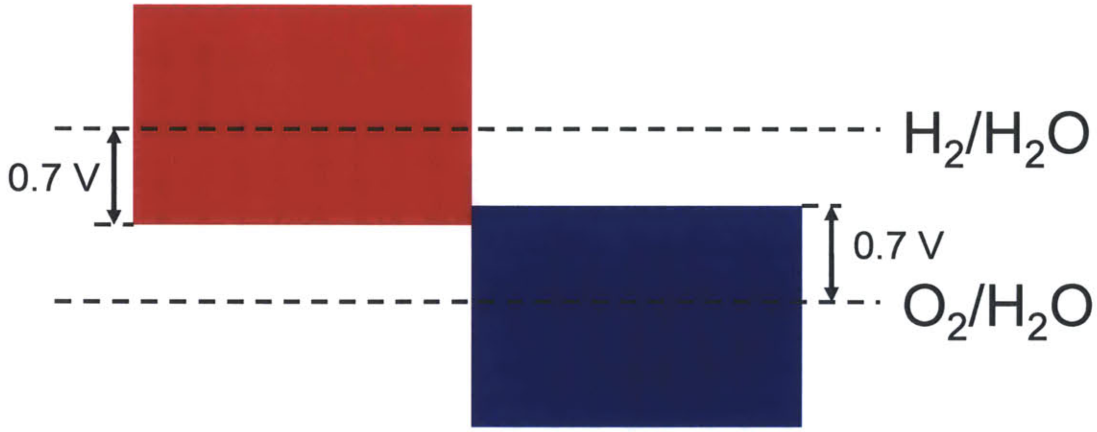

Figure 3.2 Allowed CB and VB positions. The red shaded area represents the allowed CB positions while the blue shaded area represents the allowed VB position.

The photocatalytic water-splitting process is energetically favorable only if the CB is higher than the H_2/H_2O level and VB is lower than the O_2/H_2O level. If this is not the case, then an external bias voltage is required to shift the bands to the right positions. However, applying an external bias voltage increases the complexity of the device and more importantly requires energy input to the device thus reducing the efficiency. As a result, too large a bias voltage should be avoided. We set the threshold of the allowed bias voltage as 0.7 V and eliminate all candidates whose CB is 0.7 eV lower than the

H_2/H_2O level or whose VB is 0.7 eV higher than the O_2/H_2O level in water as shown in Fig. 3.2.

3.3 Results of the screening

3.3.1 Binary nitrides

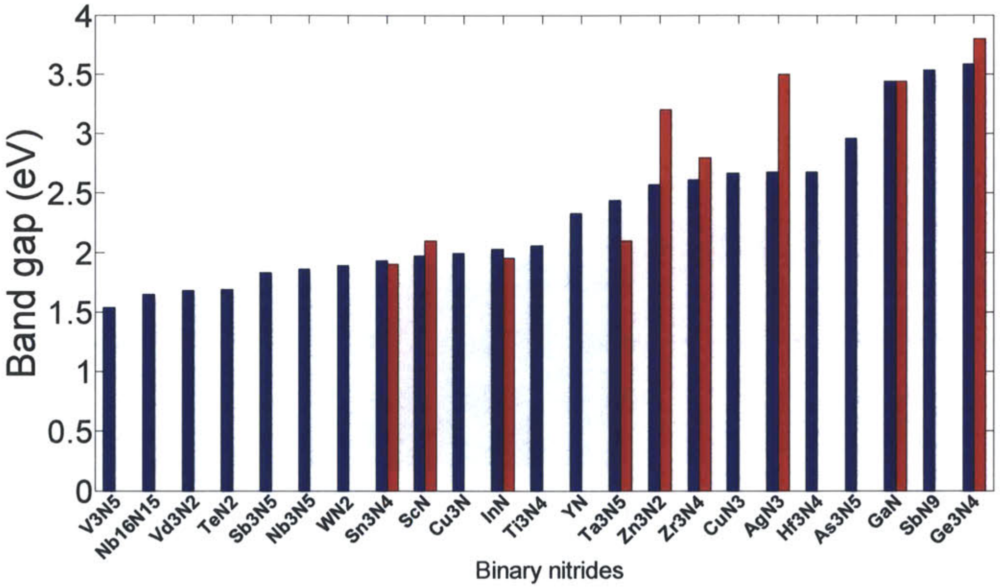

Figure 3.3 Binary metal nitrides from the ISCD with a calculated band gap between 1.5 eV to 3.6 eV. The blue bars are computational band gaps while the red bars are experimental band gaps (if available). The experimental band gaps are collected from Refs. [3, 128-136].

We screened 68 different binary nitrides M-N where M consists of all transition metal elements and semi-metal elements. Since all of the candidate compounds are obtained from the ICSD database, we assume them to be synthesizable, so we do not present the results of their phase stability here. We find that 23 binary nitrides have a gap between 1.3 eV and 3.6 eV. These gaps and some experimental gap data (if available) are shown in Fig. 3.3. There is generally good agreement between computational band gaps and experimental band gaps.

For the 23 compounds with a suitable band gap, the band edge positions are calculated. All candidates not satisfying the band position criteria indicated in Fig. 3.2 are eliminated. The remaining candidates and their band levels are shown in Table 3.1.

Material	Band gap (eV)	CB vs. H_2/H_2O (eV)	VB vs. O_2/H_2O (eV)
GaN	3.49	-0.26	-2.63
Ge_3N_4	3.59	-0.31	-2.67
Ta_3N_5	2.37	0.66 (0.40 in exp)	-0.49 (-0.37 in exp)
Cu_3N	1.99	-0.31	-1.06
AgN_3	2.68	0.48	-0.97
Zr_3N_4	2.61	-0.58	-1.96

Table 3.1 Identified binary nitrides candidates. In the column of "CB vs. H_2/H_2O" and "VB vs. O_2/H_2O", the number indicates how much the band edge is higher (more negative in the NHE reference) than the corresponding water level. Therefore, a positive number in the "CB vs. H_2/H_2O" column and a negative number in the "VB vs. O_2/H_2O" column is the optimum case as that indicates that the CB and VB are bracketing the water redox levels and no bias voltage is needed.

The first three nitrides in Table 3.1, GaN, Ge_3N_4 and Ta_3N_5 are known as water-splitting photocatalysts[44, 65-66]. Only for Ta_3N_5 have the band edge positions been experimentally measured[3], and these values are included in Table 3.1 for comparison. Cu_3N, AgN_3, and Zr_3N_4 are known compounds but have not been reported as photocatalysts yet. We plot their band positions relative to the water redox levels in Fig. 3.4.

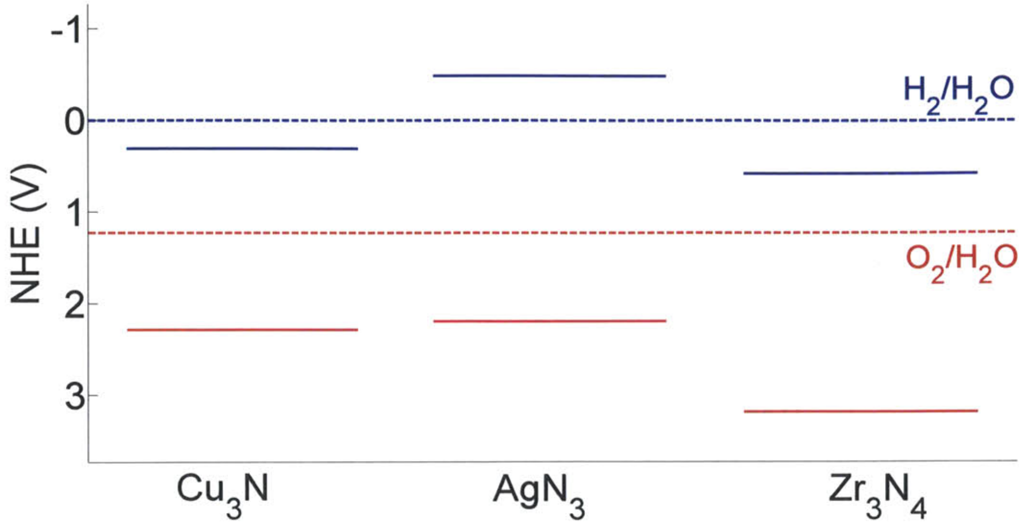

Figure 3.4 Band edge positions of Cu_3N, AgN_3, and Zr_3N_4 in the normal hydrogen electrode (NHE) reference. The solid blue lines indicates the CB levels and the solid red lines indicates the VB levels.

Fig. 3.4 suggests that AgN_3 has its CB and VB bracketing the water redox levels, and thus may achieve water-splitting without an external bias voltage. However, its band gap, predicted to be 2.68 eV and experimentally measured as 3.5 eV, is suitable to absorb only UV light. Cu_3N has a VB lower than the O_2/H_2O level in water but its CB is 0.31V lower than the H_2/H_2O level in water too. This indicates that H_2 evolution cannot be photo-catalyzed without applying an external bias voltage of at least 0.3V. However, the band gap of Cu_3N, predicted as 1.99 eV, is relatively small. This may provide enough optimization room to increase the CB while still retaining a reasonable gap. Similar to Cu_3N, Zr_3N_4 also has a too low CB and may need a bias voltage to photo-catalyze H_2 evolution. However, unlike Cu_3N, the band gap of Zr_3N_4, predicted as 2.61 eV, is already relatively large and provides little optimization room to increase the CB. As a result,

Zr_3N_4 is likely to be less efficient as a visible light driven photocatalyst.

Our screening of the binary nitrides reproduced three known binary photocatalysts, Ta_3N_5, GaN, and Ge_3N_4. In addition, we identified three known compounds as new candidates: Cu_3N, AgN_3, and Zr_3N_4. Cu_3N has the potential to be an efficient visible light driven photocatalysts, while AgN_3 and Zr_3N_4 are more likely to work under UV illumination.

3.3.2 Ternary oxynitrides

In this section, we screened 1503 different ternary oxynitrides, M-O-N, where M is one of the d^0 or d^{10} cations mentioned in Section 3.2. The calculated phase stability of these compounds is shown in Fig. 3.5. As most of these compounds are computationally designed, it is not surprising that many of them are not stable as indicated by their large ΔH for decomposition in Fig. 3.5(a).

Fig. 3.5 indicates that all ternary oxynitrides consisting of V^{5+}, Cr^{6+}, Mo^{6+}, or Sb^{5+} are very unstable. This may be explained by the limited oxidation power of nitrogen gas. Support for this interpretation is the fact that there are no stable binary nitrides for V^{5+}, Cr^{6+}, Mo^{6+}, and Sb^{5+} in the ICSD. Moreover, we will show in the Section 3.4 that the required oxidizing power for these four cations are indeed the highest among all cations listed in Fig. 3.5. Fig. 3.5 also suggests that the majority of the stable and quasi-stable ternary oxynitrides are obtained with Ti^{4+}, Zr^{4+}, Hf^{4+}, Ta^{5+}, Ga^{3+}, and Ge^{4+} which are much easier to oxidize.

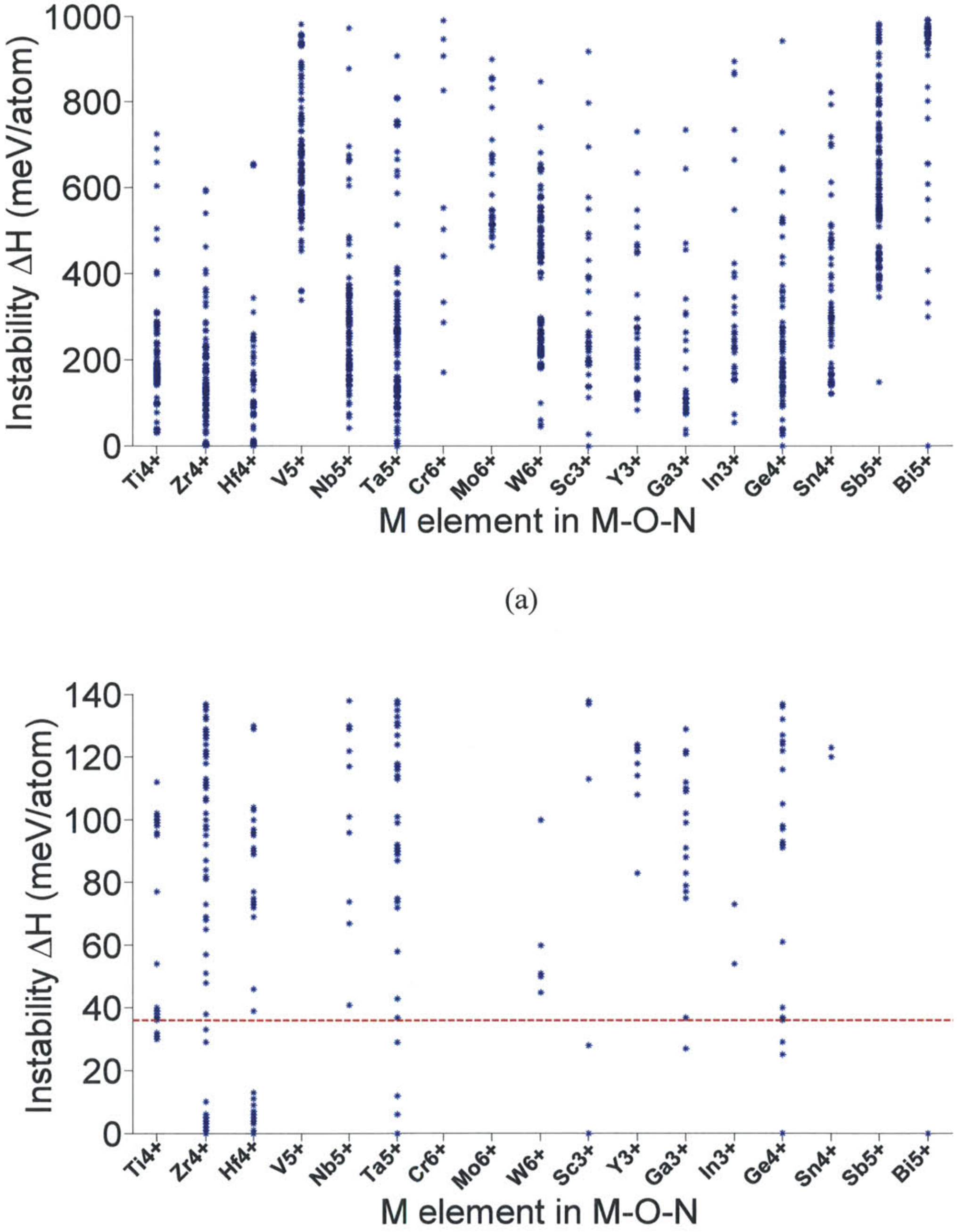

(a)

(b)

Figure 3.5 Phase stability of ternary oxynitrides. Each point represents a different compound. The instability energy ΔH is defined in Section 3.2. Larger ΔH indicates a larger instability. Figure (a) presents all candidate compounds whose ΔH is less than 1000 meV/atom. Figure (b) is an enlarged version of Figure (a) focusing on the stable and quasi-stable candidates region. The red dashed line in Figure (b) represents the elimination criterion of this step, 36 meV/atom. All candidates above the red line were eliminated.

Material	Reported/ New	ΔH (meV/atom)	Band gap (eV)	CB vs. H_2/H_2O (eV)	VB vs. O_2/H_2O (eV)
TaON	Reported	0	2.83	0.64 (0.34 in exp)	-0.97 (-0.93 in exp)
Zr_2ON_2	Reported	0	2.57	-0.34	-1.67
$Ti_3O_3N_2$	New	31	2.37	0.22	-0.92
$Zr_3O_3N_2$	New	1	3.40	1.54	-0.63

Table 3.2 Identified ternary oxynitrides candidates. The numbers in the column of "CB vs. H_2/H2O" and "VB vs. O_2/H2O" have the same meaning as in Table 3.1.

After further screening on band gap and band edge positions, four ternary oxynitrides, TaON, Zr_2ON_2, $Zr_3O_3N_2$, and $Ti_3O_3N_2$ are identified as photocatalysts as shown in Table 3.2. Among the four ternary oxynitrides, TaON is a well-known water-splitting photocatalysts[3]. Its band edge positions have been experimentally measured[3] and are given in Table 3.2 for comparison. Zr_2ON_2, while not present in the ICSD, has been reported as a promising material for photo-electrochemical water-splitting[137]. And the reported bixbyite structure for this compound is the same as our prediction, showing some validity of our structure prediction approach.

The remaining two materials, $Ti_3O_3N_2$ and $Zr_3O_3N_2$ have not been reported yet and are predicted by this work. Both compounds are generated from the crystal structure of Ta_3N_5. Their crystal structures are compared in Fig. 3.6. The instability energy ΔH is 31 meV/atom for $Ti_3O_3N_2$ and 1 meV/atom for $Zr_3O_3N_2$. This suggests that both materials are likely to be synthesizable. In fact, $Ti_3O_3N_2$ is declared to have been synthesized from a website[88].

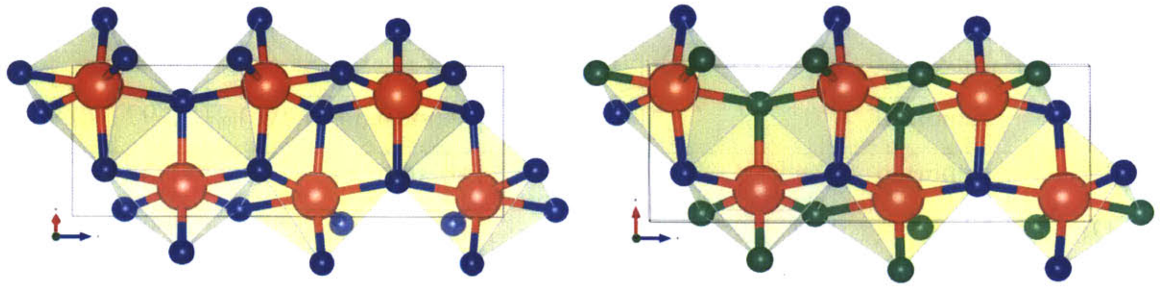

(a) Ta_3N_5 (b) $Ti_3O_3N_2$

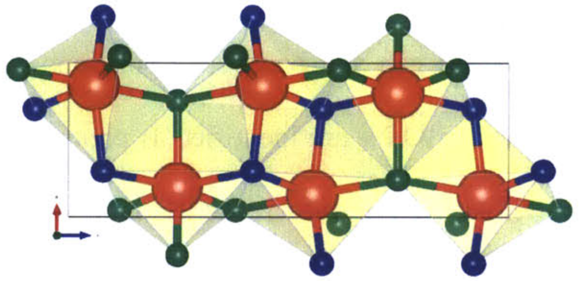

(c) $Zr_3O_3N_2$

Figure 3.6 Crystal structures of (a) Ta_3N_5, (b) $Ti_3O_3N_2$, and (c) $Zr_3O_3N_2$. Blue atoms are N, green atoms are O and red atoms are (a) Ta (b) Ti (c) Zr. Structures (b) and (c) are generated by substituting all Ta atoms in (a) for Ti atoms and Zr atoms respectively and substituting 3/5 of the N atoms in (a) for O atoms. However, note that the positions of the O atoms in (b) and (c) are not identical.

The band edge position shown in Fig. 3.7 suggest that $Ti_3O_3N_2$ is particularly interesting as its CB and VB bracket the water redox levels and its band gap, predicted as 2.37 eV, is small enough for visible light absorption. Comparing the band properties of $Ti_3O_3N_2$ with TaON, the best oxynitride photocatalyst so far[3], we find that both of them have their CB and VB bracketing the water redox levels, but the band gap of $Ti_3O_3N_2$ is expected to be smaller than the band gap of TaON (2.83 eV in our computation and 2.4 eV in experiment). Therefore, $Ti_3O_3N_2$ has a potential to exhibit better photocatalytic performance than TaON. $Zr_3O_3N_2$ also has its CB and VB bracketing the water redox levels, but its predicted band gap is large (3.40 eV). However, Fig. 3.7 suggests that the large band gap of $Zr_3O_3N_2$ is mainly due to its too high CB level. Shifting the CB downwards is a relatively easy band engineering problem which can be achieved with cation doping. If its CB can be shifted to be slightly higher than the H_2/H_2O level while retaining its VB position, the band gap will be reduced to 2.0 eV, making it a promising candidate for visible light driven photocatalysts.

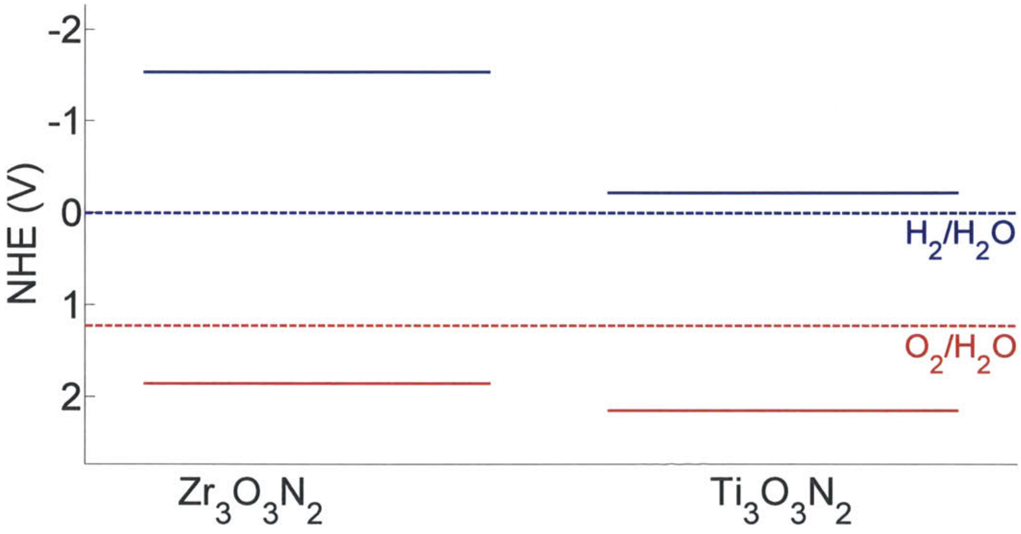

Figure 3.7 Band edge position of $Ti_3O_3N_2$, and $Zr_3O_3N_2$ in the normal hydrogen electrode (NHE) reference. The solid blue lines indicate the CB levels and the solid red lines indicate the VB levels.

In this section, we identified four materials, TaON, Zr_2ON_2, $Ti_3O_3N_2$, and $Zr_3O_3N_2$ as promising candidates for photocatalysts. TaON and Zr_2ON_2 are known photocatalysts and reproducing them from our screening system shows the validity of the approach. More importantly, we identified two new materials, $Ti_3O_3N_2$ and $Zr_3O_3N_2$. $Ti_3O_3N_2$ shows a very promising band gap and band edge positions, and has a potential to be a better visible-light driven photocatalysts than TaON. $Zr_3O_3N_2$ is predicted to be a good photocatalysts under UV illumination, and may also be visible light driven with some CB engineering. In addition, $Zr_3O_3N_2$ and $Ti_3O_3N_2$ have both the Ta_3N_5 structure, and thus solid solutions of these three materials are likely to be synthesizable, creating a large chemical space in which these materials can be optimized. Further studies on the Ta_3N_5:$Ti_3O_3N_2$ solid solution as a water-splitting photocatalyst will be presented in Chapter IV.

3.3.3 Quaternary oxynitrides

In this section, we screened 1377 quaternary oxynitrides, M1-M2-O-N, where M1 or M2 is d^0 or d^{10} metal cations as described in Section 3.2. Fig. 3.8 shows the combination of M1-M2 elements for which we find compounds with ΔH less than 0.2 eV/atom. We mentioned in Fig. 3.5 that some d^0 or d^{10} cations such as V^{5+}, Cr^{6+}, Mo^{6+}, and Sb^{5+} do not have stable corresponding ternary oxynitrides. In Fig. 3.8, we found that Cr^{6+}, Mo^{6+}, and Sb^{5+} do have some stable corresponding quaternary oxynitrides. This suggests that the required oxidizing power for these cations may decrease by adding a second metal cation into the system. It may also be noted that, for some d^0 or d^{10} cations which have stable corresponding ternary oxynitrides in Fig. 3.5, such as Zr^{4+} and Ga^{3+}, we have not found any corresponding quaternary oxynitrides in Fig. 3.8. This is because that, as we mentioned in Section 3.2.0, our sampling in quaternary oxynitrides is not exhaustive but only based on a limited prototypes of ternary oxides listed in Ref. [1]. It is possible that stable Zr^{4+} and Ga^{3+} quaternary oxynitrides exist but they cannot be derived from the prototypes we considered in this work. Another consequence of the limited sampling in quaternary oxynitrides is that some known quaternary oxynitride photocatalysts ($SrNbO_2N$[138] for instance) were not reproduced by our screening since they could not be derived from the prototypes we considered.

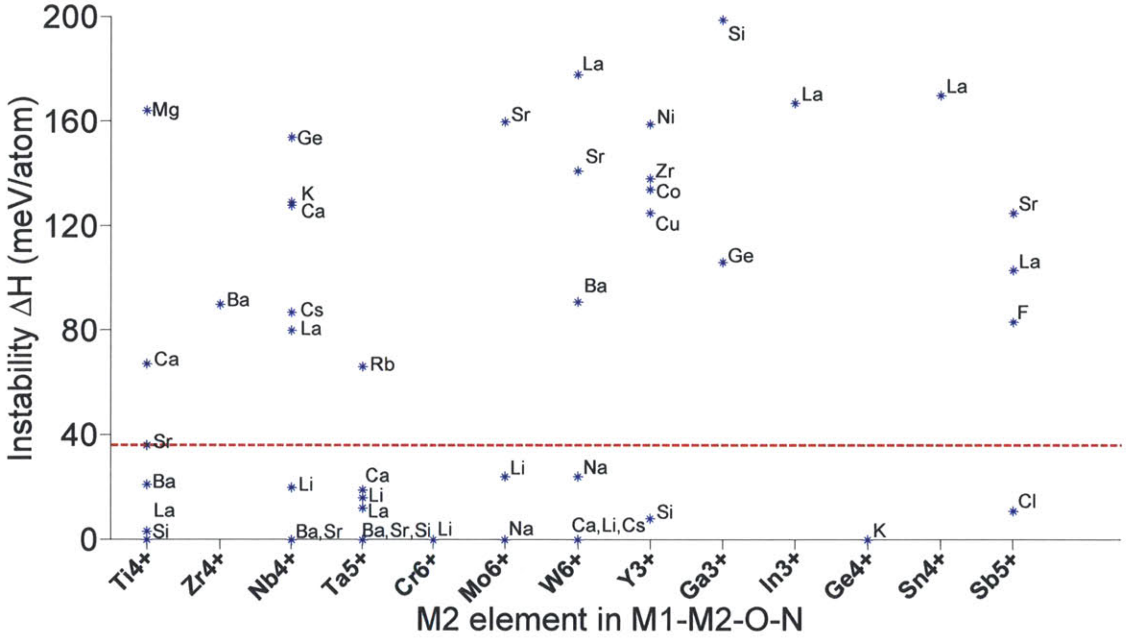

Figure 3.8 Phase stability of quaternary oxynitrides. Each point represents the lowest energy compound containing the two specified cations (i.e. a d^0 or d^{10} cation with another metal cation). We only show those pairs of cations which have at least one compound with ΔH less than 0.2 eV/atom. All candidates above the red dashed line (36 meV/atom) were eliminated.

After screening for band gap and band edge positions, seventeen compounds are identified as promising candidates for photocatalysts as shown in Table 3.3. Six of these compounds, $CaTaO_2N$[67], $SrTaO_2N$[67], $BaTaO_2N$[67], $LaTaO_2N$[69], $LaTiO_2N$[68], and $BaNbO_2N$[139] have been reported as water-splitting photocatalysts. Experimentally measured band gaps for $CaTaO_2N$, $SrTaO_2N$, and $BaTaO_2N$ are reported as 2.4 eV, 2,1 eV, and 1.8 eV respectively and our calculated band gaps for these three compounds, 2.53 eV, 2.26 eV and 1.90 eV respectively, agree well with them. Moreover, the calculated band edge positions of these three compounds suggest that their VB are actually higher than the O_2/H_2O level. Therefore, they are unsuitable for photo-catalyzing the O_2 evolution reaction without an external bias voltage. This result may explain the experimental observation that only H_2 evolution reaction is photo-catalyzed by $CaTaO_2N$, $SrTaO_2N$, and $BaTaO_2N$ in Ref. [67].

Material	Reported /New	ΔH (meV/atom)	Band gap (eV)	CB vs. H_2/H_2O (eV)	VB vs. O_2/H_2O (eV)
$CaTaO_2N$	Reported	19	2.53	1.50	0.20
$SrTaO_2N$	Reported	0	2.26	1.34	0.31
$BaTaO_2N$	Reported	0	1.90	0.97	0.30
$LaTaO_2N$	Reported	0	1.83	0.55	-0.05
$LaTiO_2N$	Reported	3	2.41	0.09	-1.09
$BaNbO_2N$	Reported	0	2.03	0.59	-0.21
$Ba_3Ta_2O_5N_2$	New	33	2.34	-0.64	-1.75
Ba_2TaO_3N	New	13	2.81	-0.37	-1.95
Sr_2NbO_3N	New	0	3.15	-0.33	-2.25
$Li_{14}Cr_2ON_8$	New	0	2.43	-0.18	-1.38
$Sr_2Ti_6O_{11}N_2$	New	36	2.86	-0.15	-1.78
$Ba_2Ti_6O_{11}N_2$	New	21	2.77	-0.11	-1.65
$La_2TiO_2N_2$	New	3	2.46	0.02	-1.21
Na_5MoO_4N	New	0	3.19	0.43	-1.53
$Na_4WO_2N_2$	New	0	2.95	0.78	-0.94
Li_5MoO_4N	New	24	2.61	1.08	-0.30
$Ca_5WO_2N_4$	New	0	3.26	1.71	-0.32

Table 3.3 Identified quaternary oxynitrides candidates. The numbers in the column of "CB vs. H_2/H2O" and "VB vs. O_2/H2O" have the same meaning as in Table 3.1.

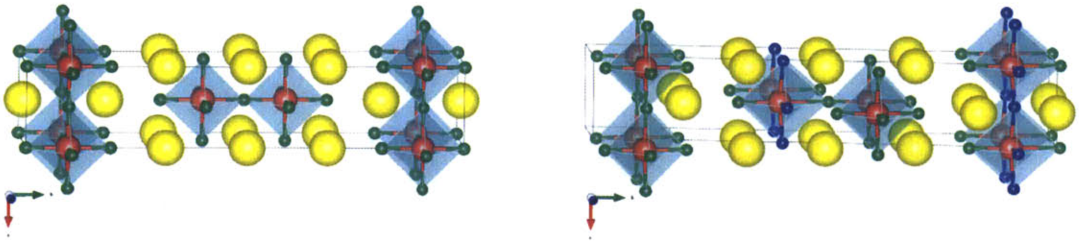

(a) $Sr_3Ti_2O_7$ (b) $Ba_3Ta_2O_5N_2$

Figure 3.9 Crystal structures of (a) $Sr_3Ti_2O_7$ and (b) $Ba_3Ta_2O_5N_2$. Blue atoms are N, green atoms are O, red atoms are (a) Ti (b) Ta, and yellow atoms are (a) Sr (b) Ba. Structure (b) is generated by substitution of all Sr atoms in (a) for Ba atoms, all Ti atoms in (a) for Ta atoms, and 2/7 of the O atoms in (a) for N atoms.

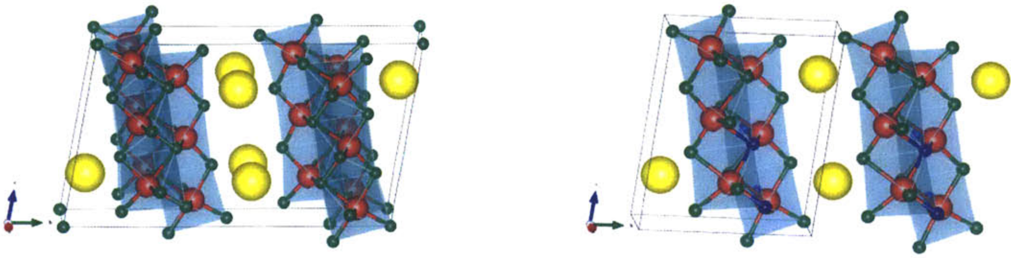

(a) $K_2Ti_6O_{13}$ (b) $Sr_2Ti_6O_{11}N_2$

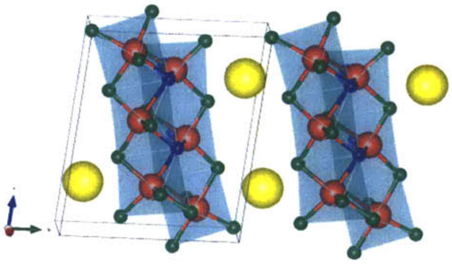

(c) $Ba_2Ti_6O_{11}N_2$

Figure 3.10 Crystal structures of (a) $K_2Ti_6O_{13}$, (b) $Sr_2Ti_6O_{11}N_2$, and (c) $Ba_2Ti_6O_{11}N_2$. Blue atoms are N, green atoms are O, red atoms are Ti, and yellow atoms are (a) K (b) Sr (c) Ba. Structures (b) and (c) are generated by substitution of all K atoms in (a) for Sr atoms and Ba atoms respectively, and 2/13 of the O atoms in (a) for N atoms.

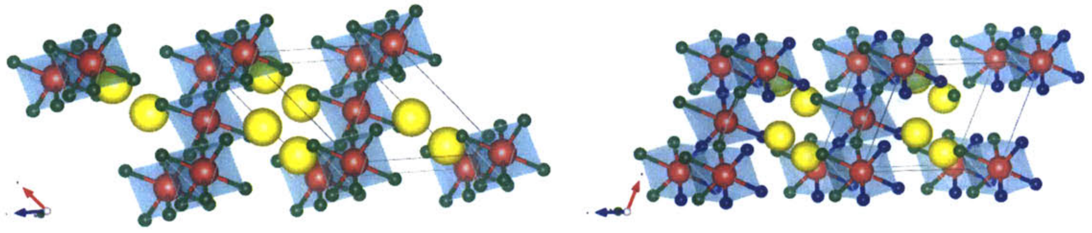

(a) Sr_2SnO_4 (b) $La_2TiO_2N_2$

Figure 3.11 Crystal structures of (a) Sr_2SnO_4 and (b) $La_2TiO_2N_2$. Blue atoms are N, green atoms are O, red atoms are (a) Sn (b) Ti, and yellow atoms are (a) Sr (b) La. Structure (b) is generated by substitution of all Sr atoms in (a) for La atoms, all Sn atoms in (a) for Ti atoms, and 1/2 of the O atoms in (a) for N atoms.

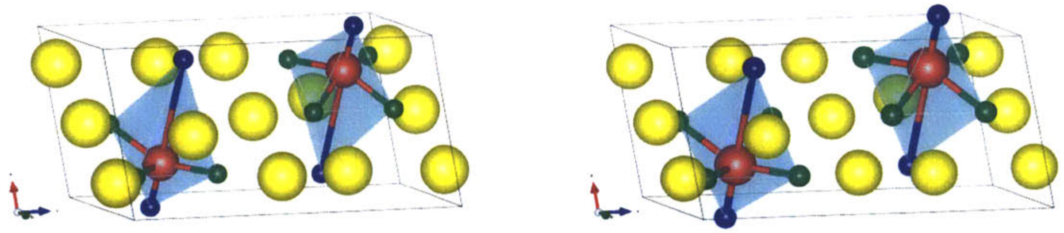

(a) Na_5MoO_4N (b) Li_5MoO_4N

Figure 3.12 Crystal structures of (a) Na_5MoO_4N and (b) Li_5MoO_4N. Blue atoms are N, green atoms are O, red atoms are Mo, and yellow atoms are (a) Na (b) Li. Structure (b) is generated by substitution of all Na atoms in (a) for Li atoms.

The remaining eleven materials, $Ba_3Ta_2O_5N_2$, Ba_2TaO_3N, Sr_2NbO_3N, $Li_{14}Cr_2ON_8$, $Sr_2Ti_6O_{11}N_2$, $Ba_2Ti_6O_{11}N_2$, $La_2TiO_2N_2$, Na_5MoO_4N, $Na_4WO_2N_2$, Li_5MoO_4N, and $Ca_5WO_2N_4$ have not been reported as water-splitting photocatalysts yet. $Li_{14}Cr_2ON_8$, Na_5MoO_4N, $Na_4WO_2N_2$, and $Ca_5WO_2N_4$ can be found in the ICSD with a known crystal structure. Ba_2TaO_3N and Sr_2NbO_3N are not in the ICSD but have been synthesized in Ref. [140]. Their structures are both declared as a K_2NiF_4 structure. This agrees with our computation as we derived both materials from a Sr_2SnO_4 structure prototype, which is closely related to K_2NiF_4. The other five candidates, $Ba_3Ta_2O_5N_2$, $Sr_2Ti_6O_{11}N_2$, $Ba_2Ti_6O_{11}N_2$, $La_2TiO_2N_2$, and Li_5MoO_4N are predicted by us. $Ba_3Ta_2O_5N_2$ is derived from $Sr_3Ti_2O_7$. $Sr_2Ti_6O_{11}N_2$ and $Ba_2Ti_6O_{11}N_2$ are derived from $K_2Ti_6O_{13}$. $La_2TiO_2N_2$ is derived from Sr_2SnO_4. Li_5MoO_4N comes from a substitution of Li for Na in Na_5MoO_4N. We compared their crystal structures in Fig. 3.9, Fig. 3.10, Fig. 3.11, and Fig. 3.12 respectively. The instability energy ΔH for $Ba_3Ta_2O_5N_2$, $Sr_2Ti_6O_{11}N_2$, $Ba_2Ti_6O_{11}N_2$, $La_2TiO_2N_2$, and Li_5MoO_4N are 33 meV/atom, 35 meV/atom, 21 meV/atom, 3 meV/atom and 24 meV/atom respectively.

The band edge positions for these eleven interesting quaternary compounds are shown in Fig. 3.13, which suggests that, among them, $La_2TiO_2N_2$ and Li_5MoO_4N have the best band properties for a visible light driven photocatalyst. For both, the CB and VB are bracketing the water redox levels, and their band gap is predicted as 2.46 eV and 2.61 eV respectively. The CB and VB of $Na_4WO_2N_2$ and $Ca_5WO_2N_4$ also bracket the water redox level, but their band gaps are too large for visible light absorption. However, similarly to $Zr_3O_3N_2$, their large band gaps are mainly due to a too high CB level. Hence, if their CB levels can be shifted downwards by cation doping or solid solution, they may still become promising for visible-light driven photocatalysis. In contrast, $Ba_3Ta_2O_5N_2$ and $Li_{14}Cr_2ON_8$ have small enough band gaps for visible light absorption, but their CB levels are lower than the H_2/H_2O level, indicating that either an external bias voltage or CB engineering is needed to achieve water-splitting. It is worth noting that the CB level of $Li_{14}Cr_2ON_8$ is only 0.18V lower than the H_2/H_2O level, indicating that the bias voltage required is small. The remaining five materials, Ba_2TaO_3N, Sr2NbO3N, $Sr_2Ti_6O_{11}N_2$, $Ba_2Ti_6O_{11}N_2$, and Na_5MoO_4N are promising candidates for photocatalysts under UV illumination.

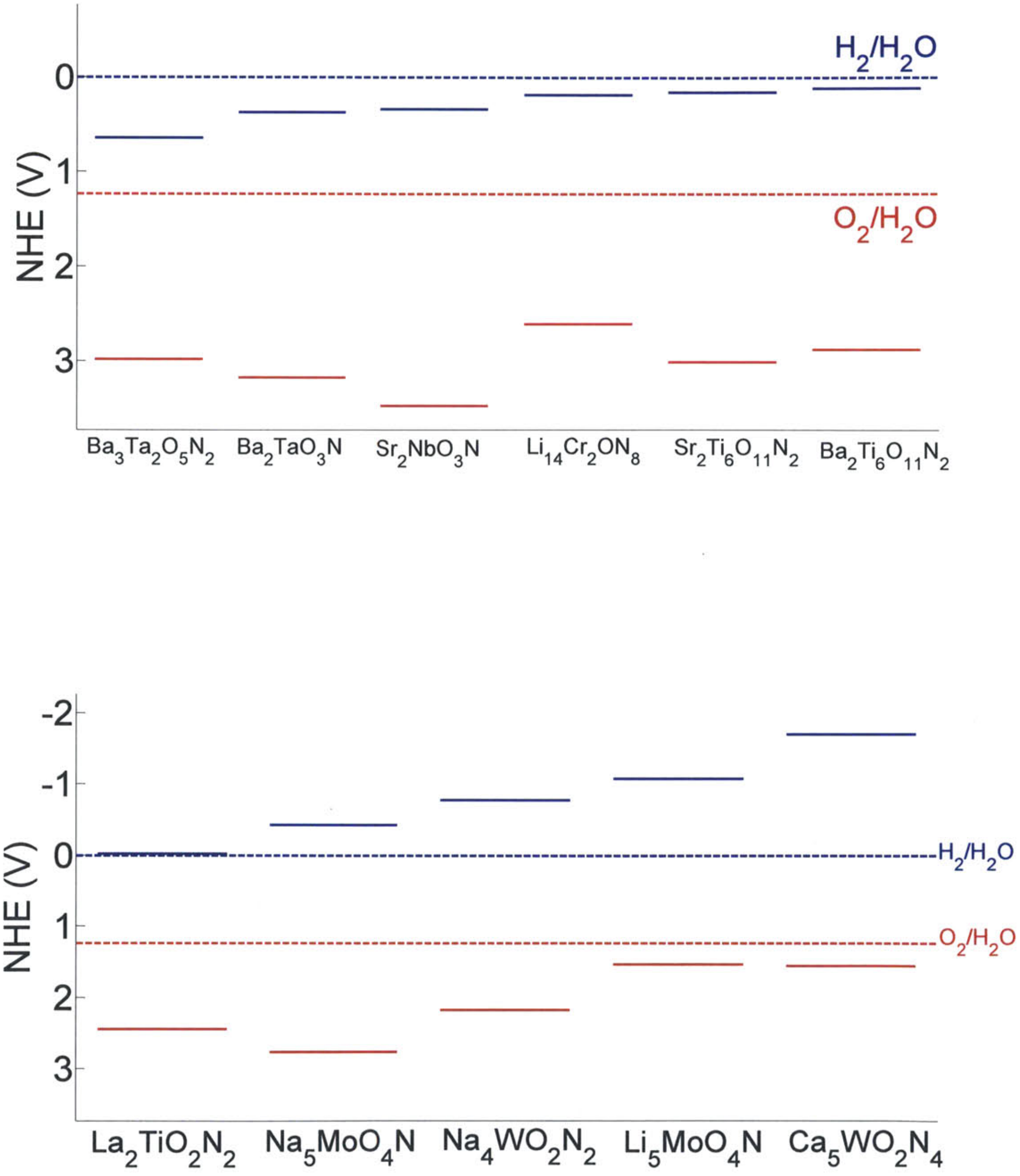

Figure 3.13 Band edge position of $Ba_3Ta_2O_5N_2$, Ba_2TaO_3N, Sr2NbO3N, $Li_{14}Cr_2ON_8$, $Sr_2Ti_6O_{11}N_2$, $Ba_2Ti_6O_{11}N_2$, $La_2TiO_2N_2$, Na_5MoO_4N, $Na_4WO_2N_2$, Li_5MoO_4N, and $Ca_5WO_2N_4$ in the normal hydrogen electrode (NHE) reference. The solid blue lines indicates the CB levels and the solid red lines indicates the VB levels.

In this section, we identified seventeen materials, listed in Table 3.3, as promising candidates for photocatalysts. $CaTaO_2N$, $SrTaO_2N$, $BaTaO_2N$, $LaTaO_2N$, $LaTiO_2N$, and $BaNaO_2N$ have been reported as water-splitting photocatalysts while the other eleven materials, $Ba_3Ta_2O_5N_2$, Ba_2TaO_3N, Sr2NbO$_3$N, $Li_{14}Cr_2ON_8$, $Sr_2Ti_6O_{11}N_2$, $Ba_2Ti_6O_{11}N_2$, $La_2TiO_2N_2$, Na_5MoO_4N, $Na_4WO_2N_2$, Li_5MoO_4N, and $Ca_5WO_2N_4$ are newly identified in this thesis. Among these eleven materials, $La_2TiO_2N_2$ and Li_5MoO_4N have the most promising band gap and band edge positions. Similar to $Ti_3O_3N_2$, they have the potential to be better water-splitting photocatalysts than TaON. $Na_4WO_2N_2$ and $Ca_5WO_2N_4$ have a band gap too large for visible light absorption and can work under UV light illumination. However, with some CB engineering, they may still be promising visible light driven photocatalysts. $Ba_3Ta_2O_5N_2$ and $Li_{14}Cr_2ON_8$ have a good band gap for visible light absorption, but they need an external bias voltage to photo-catalyze the H_2 evolution reaction. In addition, Ba_2TaO_3N, Sr_2NbO_3N and $La_2TiO_2N_2$ have the same crystal structure (Sr_2SnO_4 structure). Therefore, the solid solution of these three materials are also likely to be synthesizable and are likely to be promising candidates for water-splitting photocatalysts as well.

3.4 Discussion

We demonstrated in this chapter a high throughput computational screening for the design of novel water-splitting photocatalysts. Compounds are screened on phase stability, band gap, and band edge positions in aqueous environment. Eleven known photocatalysts are reproduced and sixteen new candidate photocatalysts are proposed by our screening, indicating the validity of the approach. However, as we mentioned in

Section 1.3, there are other important properties not considered in our screening. The aqueous stability of a material is important for the commercial exploitation of a photocatalyst. The standard tool to estimate it is the Pourbaix diagram[141]. However, Pourbaix diagrams have only been determined for elements in equilibrium with water. To assess the stability of more complex materials in water, one could use a recently developed method which enables the construction of Pourbaix diagrams almost entirely from first principles[142]. The method treats the Pourbaix diagram as a phase stability diagram for a material in equilibrium with various aqueous species.

Our screening does not consider kinetic properties either, but they also affect the performance of photocatalysts. For instance, one major issue for hematite Fe_2O_3, a promising visible light driven photocatalyst, is its poor charge carrier diffusion[143]. Defect related properties are also not considered in this work. Defect formation energy and defect concentration are closely related to the charge carrier recombination rate and lifetime, thus having an effect on the efficiency of the device. Dopability suggests to which extent the material can be engineered for a given dopant and also indicates how strong the innate P-N junction field could be designed to help the electron-hole separation. For these properties, the ab-initio predictions are often too expensive to be included in a high throughput screening system, but they could be investigated specifically for the new candidates. Another limitation is that, in this work, the properties are predicted under dark condition. However, a photocatalyst works in an illuminated environment, and thus some of its properties such as band edge positions may change accordingly.

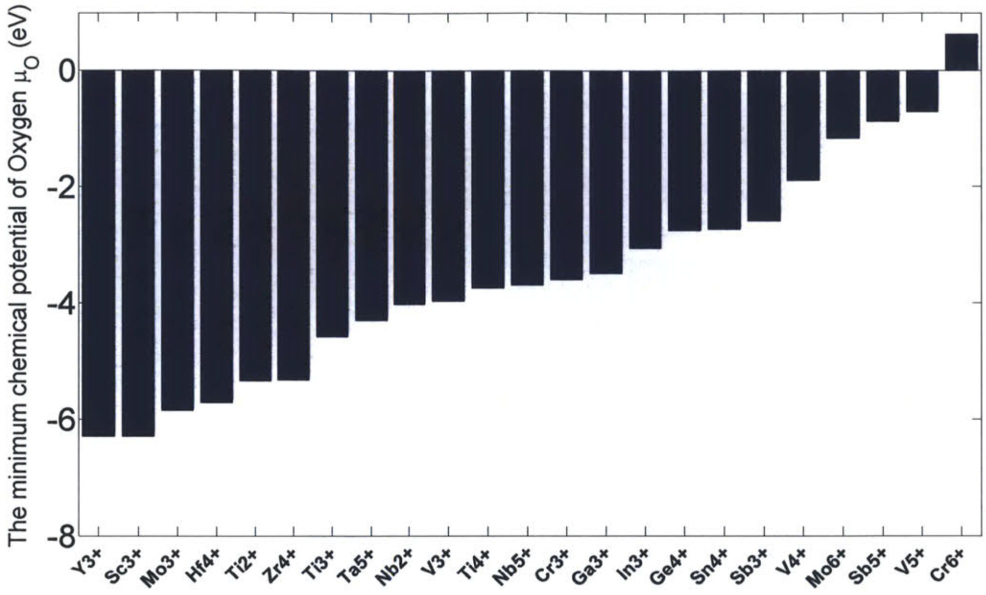

Figure 3.14 Estimate of the oxidizing power required to create some cations.

As we mentioned in Section 3.3.2, Fig. 3.5 suggests that V^{5+}, Cr^{6+}, Mo^{6+}, and Sb^{5+} do not form any stable ternary oxynitrides. We believe this is because the required oxidizing power for these cations is too large to achieve with Nitrogen. Fig. 3.14 illustrates this. For each cation in Fig. 3.14, we analyzed the thermodynamic phase stability of the binary oxide with the cation under different oxygen chemical potentials and thus evaluated the minimum oxygen chemical potential required to form a stable binary oxide with the cation. A higher minimum chemical potential indicates a larger oxidizing power required for the cation. While equivalent data for nitrides is not available, the oxide data in Fig. 3.14 should be representative of the relative oxidation strength needed. Fig. 3.14 shows that, V^{5+}, Cr^{6+}, Mo^{6+}, and Sb^{5+} require the largest oxidizing power among these cations. Moreover, these four cations do not have corresponding binary nitrides in the ICSD, supporting the observation we made in Fig. 3.5. It is worth noting that, we found stable quaternary oxynitrides with Cr^{6+}, Mo^{6+}, and Sb^{5+} in Fig. 3.8, indicating that adding a second cation may reduce the oxidation power required.

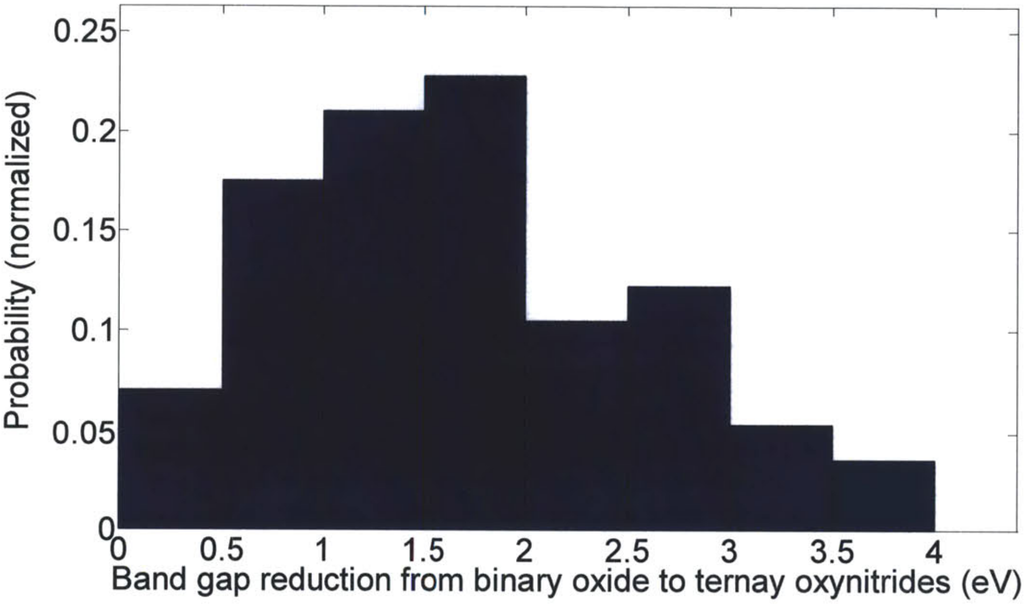

Figure 3.15 A histogram of band gap reduction from d^0 and d^{10} binary oxides to ternary oxynitrides.

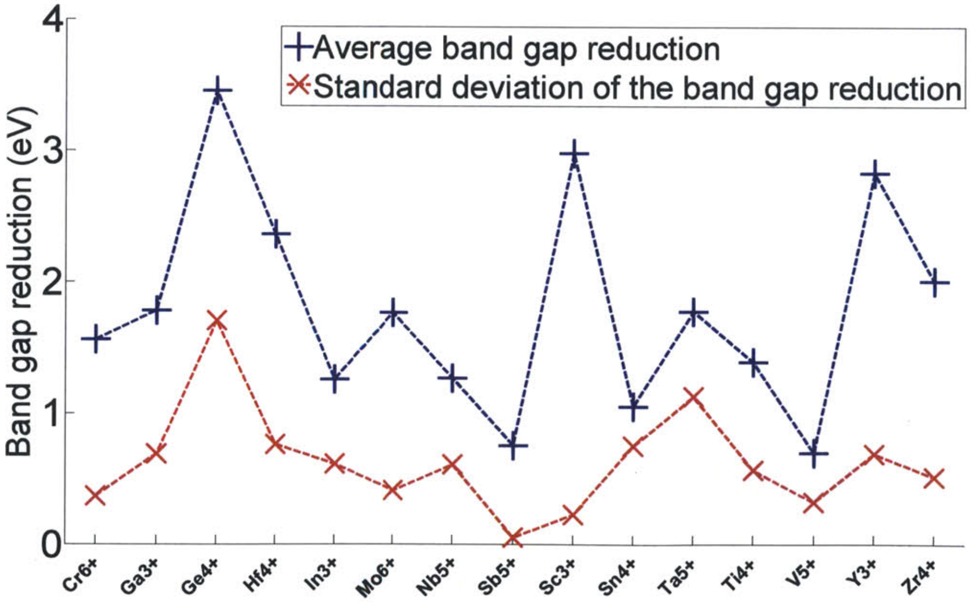

Figure 3.16 The blue line is the band gap reduction for each cation. The red line is the Standard deviation of the band gap reduction for each cation.

The reason to use nitrogen instead of oxygen as the anion was to increase the valence band energy and lower the band gap. It is therefore interesting to investigate the extent of the band gap reduction as one goes from oxide to oxynitride. To study this question, we take the lowest energy structure for each ternary oxynitride that we generated in Section 3.3.2, and compare its computed band gap to the experimentally measured gap of the binary oxide with the same cation. We collected the experimental gaps from Refs. [1, 3, 144-156]. For example, for Ta^{5+}, we compared the band gap of TaON, Ta_3O_6N, $Ta_4O_7N_2$, Ta_4ON_6, and $Ta_8O_{11}N_6$ to the experimental measured band gap of Ta_2O_5. The reasons for using experimentally measured gaps but not computed band gaps as the binary oxide references are that (1) binary oxides are generally well studied in experiment, and thus their measured gaps are accessible and reliable; (2) we used the GGA+U based Δ-sol method[87] for computing the band gaps, and the U value is typically different between oxynitrides and oxides, so even if we compare the computed gaps of oxynitrides to the computed gaps of binary oxides, the comparison would not be consistent as it is based on different U parameters. A histogram of the band gap reduction for all generated ternary oxynitride compounds is shown in Fig. 3.15. Note that we only generated ternary oxynitride containing d^0 or d^{10} cations. The mean band reduction is around 1.8 eV. This verifies that by introducing N into an oxide, the band gap can be significantly reduced. It is worth noting that the range of the band reduction is fairly large, from 0 eV to 4 eV. This large range could be due to two reasons. The first reason may be that the effect depends substantially on the cation. The second reason may be that, even for the same cation, introducing different amount of Nitrogen into the system may lead to different band gap reductions. To better demonstrate these two factors, we plot the band gap reduction for each cation in Fig. 3.16. We see clearly that the mean band gap reduction is generally different for different cations, and this difference is on the order of 1 eV. In the meantime, the standard deviation of the band gap reduction for a given cation is sometimes also on the order of 1 eV. This observation indicates that the two facts mentioned above both influence the band gap reduction.

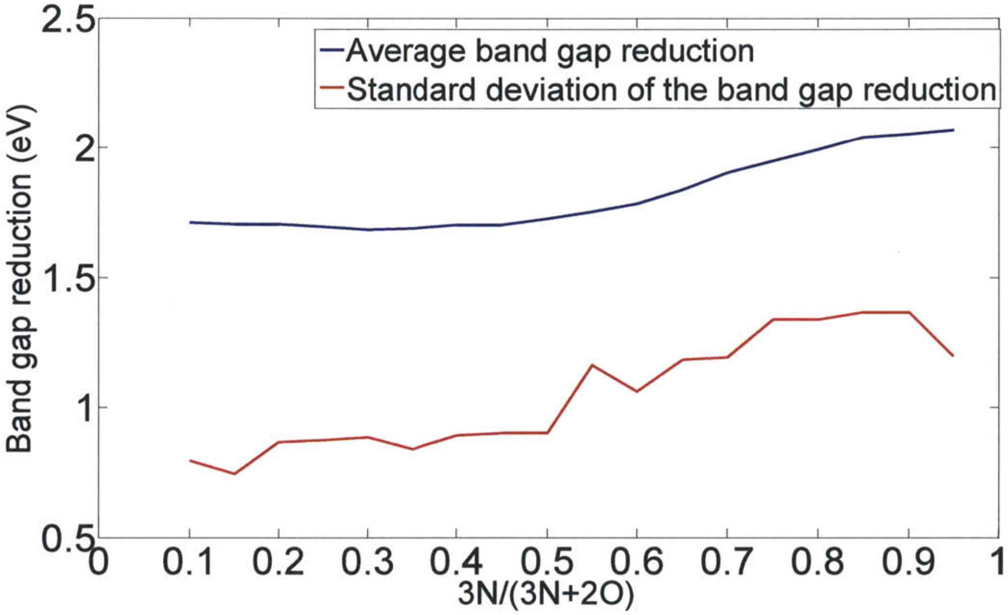

Figure 3.17 The blue line is the average band reduction as a function of N/O ratio. The red line is the standard deviation of the band gap reduction at given N/O ratio.

We look further into the effect of the amount of Nitrogen on the band gap reduction. It is possible that a change of the N/O ratio gives a different O_{2p} and N_{2p} weight in the valence band, thus leading to a different band gap reduction. Alternatively, a different amount of Nitrogen may lead to different crystal structures and thus to a different band gap reduction. Fig. 3.17 shows the average band gap reduction and its standard deviation as a function of N/O ratio. We observe that the average band gap reduction does not change much with the N/O ratio. From a very small ratio of N/O (left end of the blue line in Fig.

3.17) to a very large ratio of N/O (right end of the blue line in Fig. 3.17), the average band gap reduction changes about 0.4 eV. The rest of the difference in band gap reduction, which is on the order of 1 eV, comes from crystal structure change. As an extension of this observation, we would like to point out that adding more Nitrogen into an oxide system does not necessarily lead to a larger band gap reduction as one might assume, because this statement does not consider the effect of the possible crystal structure change. For instance, our computation suggests that the band gap of $Nb_4O_7N_2$ is less than that of Nb_4ON_6 (1.52 eV vs. 1.85 eV).

3.5 Conclusions

In this chapter, we present a high throughput first principle approach to search for new water-splitting photocatalysts, and applied it to oxynitrides and some nitrides. Most of the known photocatalysts materials in the screened chemical space are reproduced, proving the validity of the approach. In addition, sixteen new materials are suggested as promising photocatalysts, including three binary nitrides, two ternary oxynitrides and eleven quaternary oxynitrides. They have been either synthesized experimentally or predicted, by our approach, to be synthesizable. Because of their predicted band gap and band edge positions, $Ti_3O_3N_2$, $La_2TiO_2N_2$ and Li_5MoO_4N are particularly promising as visible light driven photocatalysts. In addition, with some further CB engineering or a small bias voltage, Cu_3N, $Zr_3O_3N_2$, $Ba_3Ta_2O_5N_2$, $Li_{14}Cr_2ON_8$, $Na_4WO_2N_2$, and $Ca_5WO_2N_4$ also have the potential to be good visible light driven photocatalysts. The remaining seven materials, AgN_3, Zr_3N_4, Ba_2TaO_3N, $Sr2NbO_3N$, $Sr_2Ti_6O_{11}N_2$, $Ba_2Ti_6O_{11}N_2$, and Na_5MoO_4N are candidates for photocatalysts that may work under UV illumination. In addition, based on our screening result, the solid solutions of $Ti_3O_3N_2$, $Zr_3O_3N_2$, and Ta_3N_5 and the solid solutions of Ba_2TaO_3N, Sr_2NbO_3N and $La_2TiO_2N_2$ may be synthesizable and may be promising candidates for photocatalysts too.

Chapter IV. First principles study on Ta_3N_5:$Ti_3O_3N_2$ solid solution as a water-splitting photocatalyst

In this chapter, we propose the Ta_3N_5:$Ti_3O_3N_2$ solid solution as a promising water-splitting photocatalyst. Ta_3N_5 is a known visible light driven water-splitting photocatalyst while $Ti_3O_3N_2$ is a newly predicted compound which is proposed by the high throughput screening in Chapter III as a promising water-splitting photocatalyst. Using first principles computations, we study the phase stability, band gap, and band edge positions of the solid solution. The results suggest that the solid solution can likely be synthesized, and has a band gap lower than both its end members. The minimal band gap may be around 2.0 eV for a composition around 50%:50%, indicating that good efficiency under solar illumination may be achieved. In addition, the CB and VB of the solid solution are predicted to be bracketing the water redox levels, so the photocatalysis process is energetically favorable and bias voltage may not be required.

4.1 Introduction

As we mentioned in Section 1.1, in order to achieve a ECE level above ~10% under solar illumination, which is considered to be the minimum for commercialization by US Department of Energy[34], a band gap below or around 2.0 eV is necessary for a single material water-splitting system[38-39]. Although more than 130 inorganic materials have been demonstrated to exhibit photocatalytic performance for water-splitting[1], not many of them have a band gap in this range. Over 80% of the currently known water-splitting photocatalysts are oxides[1]. The smallest band gap of these oxide compounds, which enable water-splitting without a bias voltage, is 2.3 eV[1] in the NiO/RuO_2-Ni:$InTaO_4$ system[157-158]. It is difficult to achieve a lower band gap for oxide photocatalysts, since their valence band (VB) is typically dominated by O_{2p} states which are about 3 eV lower than the H_2/H_2O level[3].

Some (oxy)nitride materials have been recently reported as low band gap (below or around 2.0 eV) photocatalysts. Examples include Ta_3N_5 (2.1 eV)[64], $SrTaO_2N$ (2.1 eV)[67], $BaTaO_2N$ (1.9 eV)[67], $LaTiO_2N$ (2.0 eV)[68], $Ca_{0.25}La_{0.75}TiO_{2.25}N_{0.75}$ (2.0 eV)[68], $LaTaO_2N$ (2.0 eV)[69] and $CaNbO_2N$ (1.9 eV)[69]. Among them, Ta_3N_5 exhibits the best photocatalytic performance. It activates both the H_2 and O_2 evolution reaction without bias voltage, while $SrTaO_2N$, $BaTaO_2N$ and $LaTaO_2N$ fail to activate the O_2 evolution reaction[3]. When tested under the same condition, Ta_3N_5 demonstrated about a 10 times faster O_2 evolution rate and at least a similar H_2 evolution rate compared to $Ca_{0.25}La_{0.75}TiO_{2.25}N_{0.75}$, $LaTiO_2N$ and $CaNbO_2N$[3]. However, the ECE of all these materials is still far from the commercialization target. Therefore, it is of interest to suggest new low band gap materials that have better potential as water-splitting photocatalysts.

Computational studies[2, 70-73, 159] have been conducted to identify new photocatalyst materials. Especially in Chapter III, we identified sixteen known or computationally predicted (oxy)nitrides as promising water-splitting photocatalyst candidates using a first principles high throughput computational screening[71]. Among these candidates, $Ti_3O_3N_2$, a newly predicted compound, is particularly interesting. Computational results indicate that it can likely be synthesized[71]. In fact, a recent report on a website[88] states to have synthesized it. Its CB and VB are predicted to be bracketing the water redox levels[71], indicating that it may activate both the H_2 and O_2 evolution reaction without any bias voltage. The potential issue of the material may be its band gap, which is predicted to be 2.37 eV in Chapter III[71]. Although this band gap is smaller than many known (oxy)nitride photocatalysts and most of the known oxide photocatalysts, it is still not small enough to potentially achieve a commercially viable ECE.

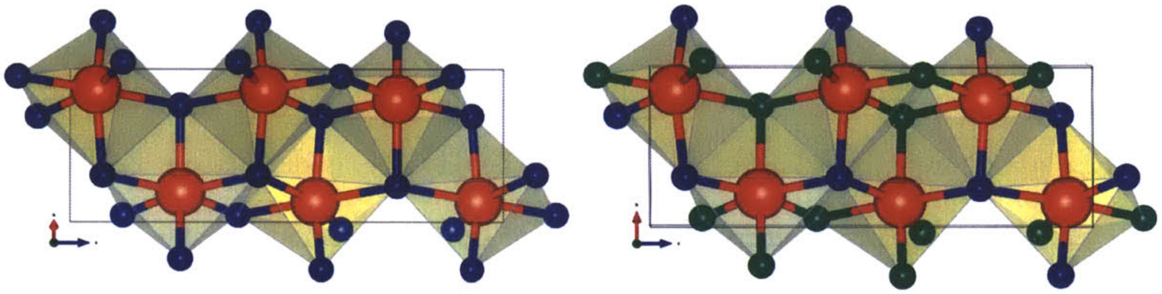

(a) Ta_3N_5 (b) $Ti_3O_3N_2$

Figure 4.1 Crystal structures of (a) Ta_3N_5 and (b) $Ti_3O_3N_2$. The structure of Ta_3N_5 is obtained from ISCD [121] while the structure of $Ti_3O_3N_2$ was proposed in Chapter III[71]. Blue atoms are N, green atoms are O, and Red atoms are Ta in (a) and Ti in (b).

$Ti_3O_3N_2$ and Ta_3N_5 have the same orthorhombic crystal structure (see Fig. 4.1) with a small volume difference. The experimental lattice parameters of Ta_3N_5 are a = 3.89 Å, b = 10.21 Å, and c = 10.26 Å[160], while the lattice parameters of $Ti_3O_3N_2$ are predicted to be a = 3.86, b = 9.89, c = 9.91[71]. Thus, it may be possible to create a solid solution of Ta_3N_5 and $Ti_3O_3N_2$. As we mentioned in Section 1.2, due to band bowing effects[62-63], solid solutions can have a lower band gap than both of their end members. Therefore, it is possible that, by forming a solid solution of Ta_3N_5 and $Ti_3O_3N_2$, one may find materials with a lower band gap than both the end members.

In this chapter, we report on the results of a first principles study of the solid solution of Ta_3N_5 and $Ti_3O_3N_2$. We evaluate the mixing enthalpy of the solid solution at zero K to determine its phase stability. We compute the band gap of the solid solution and compare it with the band gaps of the end members. We also investigate whether the CB and VB edge positions of the solid solution, like the end members, bracket the water redox levels. The detailed methods and results of these computations are presented in Section 4.2 and 4.3.

4.2 Methods

The solid solution consisting of xTa_3N_5 and $(1\text{-}x)Ti_3O_3N_2$ is denoted as $Ta_{3x}Ti_{3-3x}O_{3-3x}N_{2+3x}$. Unless specified otherwise, all DFT[55-56] computations in this chapter are performed with projector augmented wave (PAW)[89] potentials using the plane-wave code Vienna Ab-initio Simulation Package (VASP)[107-108] and the Perdew-Burke-Ernzerhof (PBE)[90] GGA exchange-correlation functional.

To study the phase stability of $Ta_{3x}Ti_{3-3x}O_{3-3x}N_{2+3x}$, a set of DFT computations are performed to determine the mixing enthalpy of the solid solution at zero K, with a Monkhorst-Pack[109] 10 × 8 × 4 k-point grid and a plane wave energy cutoff of 500 eV. In these computations, we use a supercell containing 6 cations (Ta^{5+} or Ti^{4+}) and 10 anions (O^{2-} or N^{3-}). We consider respectively 288, 225, 400, 225, 60 different possible cation and anion arrangements at five different compositions x = 1/6, 2/6, 3/6, 4/6, 5/6. Full geometric (cell shape and cell size) and ionic DFT relaxations are performed for all these configurations and also for the two end members. The mixing enthalpy of every configuration $\Delta H_{mix}^{DFT}(x,n)$ is determined by Eqn. 4.1 and is normalized per cation. Here (x,n) stands for the *n*th configuration at the composition x.

$$\Delta H_{mix}^{DFT}(x,n) = [E^{DFT}(x,n) - xE^{DFT}(Ta_6N_{10}) - (1-x)E^{DFT}(Ti_6O_6N_4)]/6 \tag{4.1}$$

To determine the band gaps, we primarily used the Δ-sol method[87] which has been introduced in Section 3.2.2 and has been widely used in Chapter III. When tested across a large number of compounds with diverse chemistries, the Δ-sol method gives a mean absolute error of 0.2 eV for the gap[87]. In addition, the band gaps of a few (oxy)nitride compounds computed by this method in Chapter III agree well with experiments[71].

As a verification of the band gap results from the Δ-sol method, the band gaps of two end members and the solid solution at selected compositions are also computed using the Heyd-Scuseria-Ernzerhof functional[119, 161] (HSE06) with a Γ-centered 7 × 7 × 3 k-point grid and a plane wave cutoff of 520 eV. Compared to Δ-sol, HSE06 is more accurate in predicting band gaps for typical semiconductors, but has larger errors for transition-metal compounds[87]. In addition, HSE06 is relatively more computationally expensive than the Δ-sol method. Therefore, we choose to primarily use the Δ-sol method for determining band gaps in this work.

To compute the CB and VB band edge positions in aqueous environment and compare them with the H_2/H_2O and O_2/H_2O levels in water, we used the three-step method[11] which has been developed in Chapter II and has been widely used in Chapter III. The method gives a mean absolute error of 0.19 eV for the band edge positions when tested on six typical photocatalysts in Chapter II[11], and also shows a good agreement with experimental values when applied to determine the band edge positions of a few (oxy)nitride systems in Chapter III[71].

4.3 Results

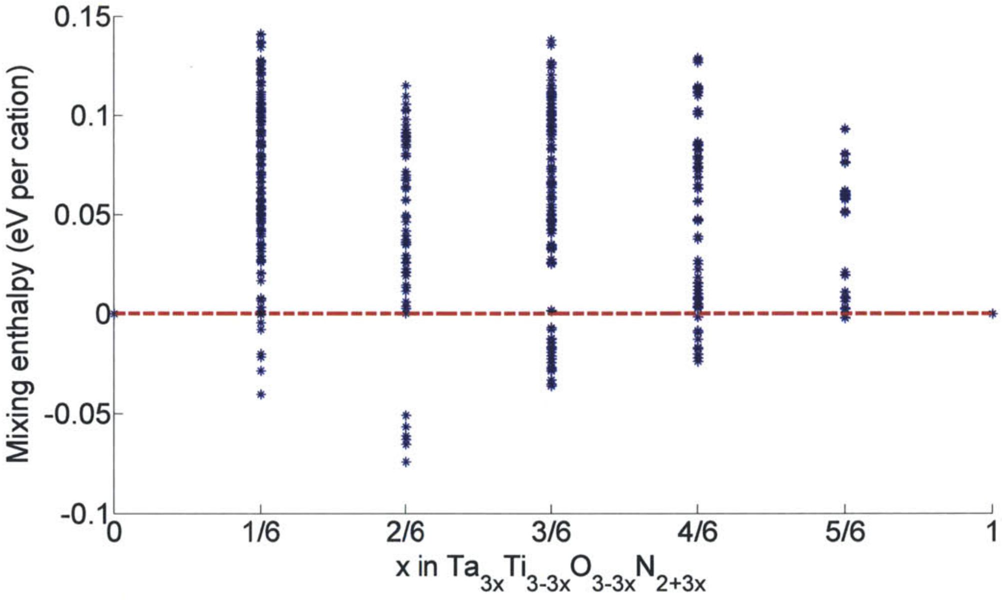

Figure 4.2 $\Delta H_{mix}^{DFT}(x,n)$ of the solid solution at compositions x = 1/6, 2/6, 3/6, 4/6, 5/6. Each blue dot represents a different configuration of the solid solution.

The mixing enthalpy, $\Delta H_{mix}^{DFT}(x,n)$ (eq. 1), is shown in Fig. 4.2. We observe that, there are a few configurations that have a negative enthalpy of mixing for each of the five compositions x = 1/6, 2/6, 3/6, 4/6, 5/6. Especially at compositions x = 1/6, 2/6, 3/6, 4/6, the lowest energy configurations have an enthalpy of mixing well below zero. This indicates that the ordered solid solution phase is likely dominant at zero K for all these compositions. At elevated temperatures, the increasing configurational entropy effect will further stabilize the solid solution phase. As a result, we believe that the solid solution

$Ta_{3x}Ti_{3-3x}O_{3-3x}N_{2+3x}$ can likely be synthesized and remain stable for all these compositions.

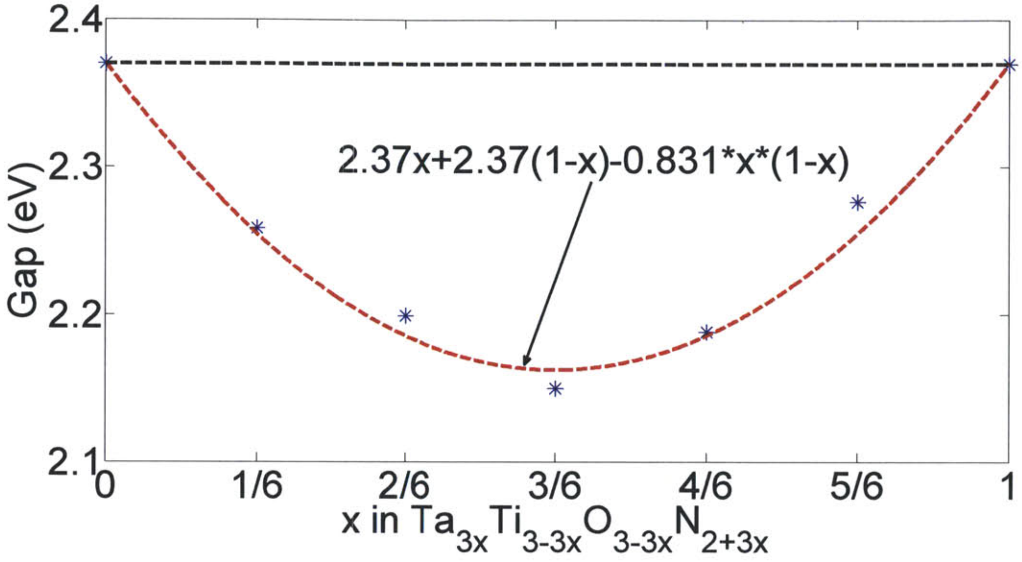

Figure 4.3 The band gap results of the solid solution $Ta_{3x}Ti_{3-3x}O_{3-3x}N_{2+3x}$. Blue dots represent the band gaps determined by the Δ-sol method. The red dash line represents $E_g(x)$ from Eqn. 4.2.

$$E_g(x) = (1-x)E_g(0) + xE_g(1) - b_g x(1-x) \tag{4.2}$$

To determine the band gap of the solid solution, we use the Δ-sol method[87] to calculate the gap of the configuration with lowest energy at each composition. The band gap of both Ta_3N_5 and $Ti_3O_3N_2$ determined by the same method is 2.37 eV[71], and the computed gap of Ta_3N_5 is in reasonable agreement with the experimental measurement, 2.1 eV[64]. We find that the band gap in the solid solution is indeed lower than the gaps of both the end members. We also notice that the band gap vs. composition x exhibits a convex shape. This is commonly known as the downward band bowing effect[62-63] and is usually described by Eqn. 4.2. In the equation, $E_g(0)$ and $E_g(1)$ represent the band gaps of the two end members, while b_g represents the magnitude of the band bowing. In this case, $E_g(0) = E_g(1) = 2.37\ eV$ and $b_g = 0.831\ eV$ may best fit the results from the Δ-sol method, and the corresponding $E_g(x)$ is shown (as the red dash line) in Fig. 4.3. At composition $x = 0.5$, $E_g(x)$ is minimized with a value of 2.16 eV, which is ~0.2 eV lower than the band gap of both the end members. It is worth to note that, the experimental band gap of Ta_3N_5 is actually 2.1 eV instead of 2.37 eV. Therefore, we may expect the minimal band gap of the solid solution in practice to be lower than 2.16 eV. In fact, if we substitute into Eqn. 4.2 the experimental band gap of Ta_3N_5 (i.e. $E_g(1) = 2.1\ eV$), we find that, in a wide region of compositions $3/6 \leq x \leq 5/6$, $E_g(x)$ is close to 2.0 eV. In conclusion, the solid solution of Ta_3N_5 and $Ti_3O_3N_2$ exhibits a band gap lower than the band gaps of both the end members, and the minimal band gap would be reached near composition $x = 0.5$ with a likely value close to 2.0 eV.

Besides band gap, band edge positions are also important for water-splitting photocatalysts since the photocatalysis process is energetically favorable only if the CB and VB bracket the water redox levels. Otherwise, a bias voltage is necessary. Fig. 4.4 shows the results of the band edge positions vs. the water redox levels determined by the three-step method reported in Ref. [11]. For the two end members, Ta_3N_5 and $Ti_3O_3N_2$, the band edge positions have been computed in Ref. [71] by the same method, and are reproduced in this work. In addition, the band edge positions of Ta_3N_5 have been measured experimentally[3] and the results are shown in Fig. 4.4. The computational results are in a good agreement with the experimental results. Furthermore, the band edge position of the solid solution at composition $x = 0.5$, i.e. $Ta_{1.5}Ti_{1.5}O_{1.5}N_{3.5}$, is computed and is also shown in Fig. 4.4. This solid solution corresponds to the state with minimal band gap in Fig. 4.3. Fig. 4.4 shows that both the end members and the solid solution have their CB and VB bracketing the water redox level. This indicates that no bias voltage is required for either of them.

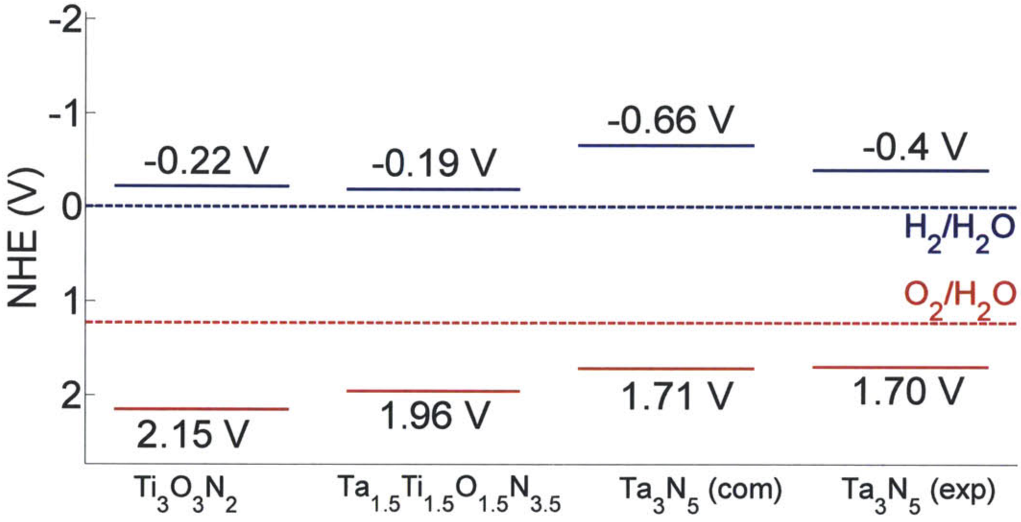

Figure 4.4 Band edge positions of $Ti_3O_3N_2$, Ta_3N_5 and their solid solution $Ta_{1.5}Ti_{1.5}O_{1.5}N_{3.5}$ versus the normal hydrogen electrode (NHE) reference. Both the computational and experimental results of Ta_3N_5 are shown in the figure. The solid blue lines represent the CB levels and the solid red lines represent the VB levels. The number beside each line shows the value of the band edge position.

4.4 Discussion

There are many possible cation and anion arrangements in the solid solution $Ta_{3x}Ti_{3-3x}O_{3-3x}N_{2+3x}$. It is interesting to recognize the patterns which lead to low energy configurations. We mainly focus on pair patterns in this analysis. We observe the first and second nearest neighbor cation-cation, anion-anion and cation-anion pairs in the top 10% lowest energy configurations at each composition. In these configurations, we find that (1) for cation-anion pairs, Ti-O and Ta-N are preferred rather than Ti-N and Ta-O. This is likely due to the minimization of the columbic energy. (2) For anion-anion pairs, O and N like to pair with the same type of anion rather than forming O-N. This agrees with the observation in Ref. [124], that the anion ordering of oxynitrides is driven to have more N-N bonds. (3) For the cation-cation pairs, Ti-Ta is slightly more favorable than Ti-Ti and Ta-Ta. These findings indicate that the low temperature ordering is likely driven by the minimization of the electrostatic energy. Although size effects, in this case likely between N^{3-} and O^{2-}, tend to add a positive contribution to the enthalpy of mixing[162], the electrostatic effect is still dominant and leads to an overall negative enthalpy of mixing[163] in this system.

Fig. 4.3 in Section 4.3 shows that the band gap of the solid solution has a convex shape, i.e. a downward band bowing effect[62-63]. This effect leads to the important finding that the solid solution $Ta_{3x}Ti_{3-3x}O_{3-3x}N_{2+3x}$ may achieve lower band gaps than both of its end members. Therefore, it is interesting to understand the mechanism of this phenomenon. The band edge position result in Fig. 4.4 shows that the solid solution $Ta_{1.5}Ti_{1.5}O_{1.5}N_{3.5}$ has its CB position very close to that of $Ti_3O_3N_2$ and its VB position between those of $Ti_3O_3N_2$ and Ta_3N_5. This indicates that the solid solution is likely to have a CB dominated by Ti_{3d} orbitals and a VB mainly dominated by N_{2p} orbitals. To confirm this, we computed the density of states (DOS) diagrams of the solid solution $Ta_{1.5}Ti_{1.5}O_{1.5}N_{3.5}$ using respectively the PBE-GGA functional[90] with a Γ-centered 10 × 8 × 4 k-point grid and HSE06[119, 161] with a Γ-centered 7 × 7 × 3 k-point grid. The GGA DOS diagram is shown in Fig. 4.5. We find that the solid solution indeed has its CB dominated by the orbitals from Ti atoms and has its VB dominated by the orbitals from N atoms. The HSE06 DOS diagram, though is not shown here, gives the same trends. We further confirm that these dominant orbitals are mainly Ti_{3d} and N_{2p}. It is known that Ti_{3d} orbitals are lower in energy than Ta_{5d} orbitals[164] which dominate the CB of Ta_3N_5, and N_{2p} orbitals are higher in energy than O_{2p} orbitals[3] which partially contribute to the VB of $Ti_3O_3N_2$. Therefore, being dominated by Ti_{3d} orbitals and N_{2p} orbitals at CB and VB, the solid solution exhibits a lower band gap than the interpolation of the band gaps of its end members. This explains the mechanism of the downward band bowing effect.

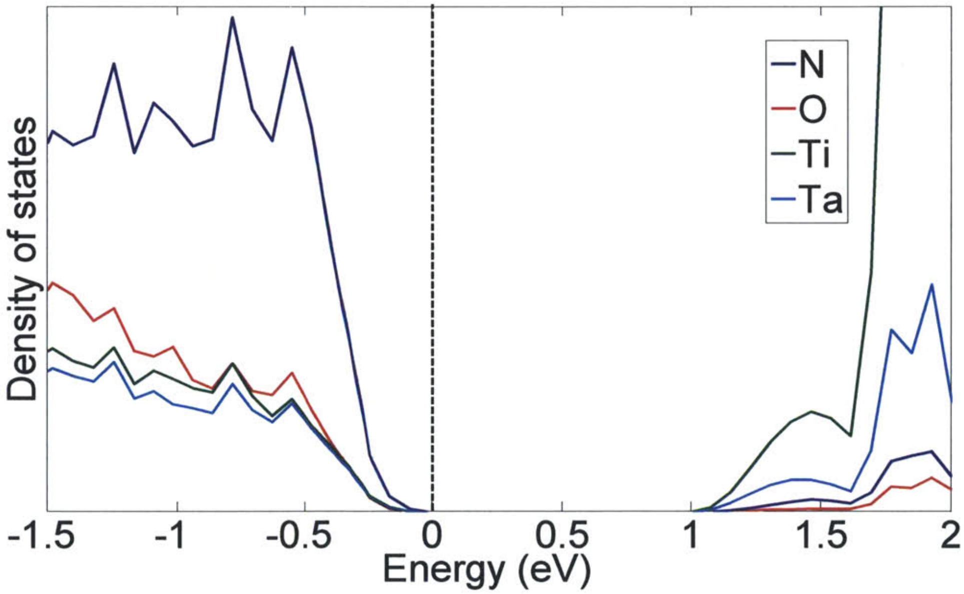

Figure 4.5 Computed DOS of the solid solution $Ta_{1.5}Ti_{1.5}O_{1.5}N_{3.5}$ by PBE-GGA functional. The DOS contributed by Ta, Ti, O, N are colored as cyan, green, red and blue respectively.

To further support the result of downward band bowing, the band gaps of $Ta_{1.5}Ti_{1.5}O_{1.5}N_{3.5}$, Ta_3N_5 and $Ti_3O_3N_2$ have been also computed using HSE06[119, 161]. The HSE results indicate that all three materials have an indirect band gap, and the band gap values are compared with the Δ-sol results in Table 4.1. We find that, comparing to the experimental value, the Δ-sol method overestimates the band gap of Ta_3N_5 while HSE06 underestimates it by roughly the same magnitude, 0.2 ~ 0.3 eV. In spite of this, both methods show that the solid solution has a lower band gap than both of the end members. In fact, if we compute the magnitude of the downward band bowing at the composition $x = 0.5$ by Eqn. 4.3, both methods give a ΔE_g of ~0.2 eV. Therefore, the results of band gap reduction from these two methods are consistent.

	Ta_3N_5 (exp 2.1 eV)	$Ta_{1.5}Ti_{1.5}O_{1.5}N_{3.5}$	$Ti_3O_3N_2$
Δ-sol method	2.37 eV	2.15 eV	2.37 eV
HSE06	1.81 eV	1.71 eV	2.04 eV

Table 4.1 Computed band gaps of Ta_3N_5, $Ta_{1.5}Ti_{1.5}O_{1.5}N_{3.5}$ and $Ti_3O_3N_2$ by the Δ-sol method and HSE06.

$$\Delta E_g = 0.5E_g(Ta_3N_5) + 0.5E_g(Ti_3O_3N_2) - E_g(Ta_{1.5}Ti_{1.5}O_{1.5}N_{3.5}) \qquad (4.3)$$

In this work, we propose the solid solution $Ta_{3x}Ti_{3-3x}O_{3-3x}N_{2+3x}$ as a promising water-splitting photocatalyst based on the computational phase diagram, band gap and band edge positions. However, some aspects which are not considered in this work may be also significant for the photocatalytic performance. For instance, we have not considered the aqueous stability even though it is important for the commercial exploitation of photocatalyst. This is mainly due to the fact that handling such a problem by first principles computations is still challenging, though several studies have recently proposed approaches to predict aqueous stability[142, 165]. While computational results are not available, relevant information from experiments can still be collected. For instance, the aqueous stability of Ta_3N_5 has been tested in experiments. The material is stable under a pH $\geq$ 7[64], indicating that it can work in both pure water and sea water. $Ti_3O_3N_2$ has not been tested so far, but oxynitrides are usually considered to be more stable in water than nitrides[3].

Kinetic properties of the solid solution are not computed in this work, but they may affect the rate of both the H_2 and O_2 evolution reaction, which is an important aspect of photocatalytic performance. However, in most cases, the reaction rate is not only determined by the photocatalyst itself but is also significantly affected by the co-catalysts, materials that can lower the kinetic barrier of the water-splitting reaction at the interface. For instance, the rate of H_2 evolution reaction becomes ~100 times faster when 5 wt% Ru is added to TaON[43], and in the ZnO:GaN solid solution, both H_2 and O_2 evolution changed from negligible to clearly observable when 5 wt% RuO_2 was present[44].

4.5 Conclusions

In this chapter, we propose the solid solution $Ta_{3x}Ti_{3-3x}O_{3-3x}N_{2+3x}$ as promising water-splitting photocatalysts. By first principles computations, we study the phase stability, band gap, and band edge positions of the system. The solid solution is very likely to be synthesizable. In addition, the band gap of the solid solution is lower than the band gap of both its end members. The minimal band gap is achieved at the composition x around 0.5 and may be around 2.0 eV. This indicates that the solid solution may be able to achieve high absorption of solar illumination and obtain good efficiency. We also confirm that the CB and VB of the solid solution is bracketing the water redox levels, meaning that the photocatalysis process is energetically favorable and bias voltage may not be required in this system. In conclusion, all the results suggest that the $Ta_{3x}Ti_{3-3x}O_{3-3x}N_{2+3x}$ solid solution has a good potential to achieve water-splitting photocatalysis under solar illumination with high efficiency.

Chapter V. Conclusions and future work

In this thesis, we use first principles computational approaches to facilitate the design of new inorganic water-splitting photocatalysts. We have developed a so-called three-step method to compute the band edge positions relative to the water redox levels in solution. The method, which costs three DFT GGA computations for each semiconductor, gives an absolute error of 0.19 eV when tested on several typical photocatalysts. To our knowledge, no other first principles method for computing the same property has been reported with a better accuracy so far.

We have constructed a high throughput screening system and have used it to identify sixteen new promising candidates for water-splitting photocatalysts from about 3000 (oxy)nitride compounds. Particularly promising candidates, such as $Ti_3O_3N_2$, $La_2TiO_2N_2$ and Li_5MoO_4N, have potentials to exhibit a better photocatalytic performance than any of the known water-splitting photocatalysts.

The screening does not only propose promising candidates, but also suggests possible optimization strategies for the identified candidates. For instance, we have found in the screening that a particularly promising candidate $Ti_3O_3N_2$ has the same crystal structure as Ta_3N_5, a known photocatalyst with a low band gap. This implies that the performance of these two materials can likely be improved by forming the Ta_3N_5:$Ti_3O_3N_2$ solid solution. Using first principles computations, we conclude that the solid solution may indeed be a promising water-splitting photocatalyst with a band gap ~0.2 eV lower than its end members. Due to this band gap reduction of ~0.2 eV, the maximum achievable efficiency increases from ~5% to ~10%.

In the future, we may adapt the high throughput screening system and the related methodologies that are developed in this thesis for the screening of other promising chemical spaces, such as oxysulfides, and solid solutions of oxides, nitrides, and sulfides.

Similar to oxynitrides, oxysulfides also have a higher VB position compared to oxides and may be stable in solution. In fact, a few oxysulfides have been experimentally demonstrated to exhibit a photocatalytic performance. The screening system in this thesis can be directly used to identify promising candidates for water-splitting photocatalysts among a large number of oxysulfide compounds.

Solid solutions of oxides, nitrides, and sulfides are promising for low band gap photocatalysts as well. Because of the band bowing effect, solid solutions can have a lower band gap than both of their end members. Therefore, the band gap problem of oxide photocatalysts may be solved by forming solid solutions with nitrides, sulfides, or even with other oxides. For this screening purpose, two adjustments should be made to the original screening system: (1) a preparation step that groups all candidate end members by their crystal structures should be added into the system; (2) the phase stability screening (Section 3.2.1), band gap screening (Section 3.2.2), and band edge positions screening (Section 3.2.3) should now consider solid solutions at different compositions.

The screening system can also be generalized to identify photocatalysts for other applications. For example, photocatalysts can be used in various CO_2 reduction schemes to produce liquid fuels (Table 5.1). In this application, the required properties of the photocatalysts are similar to those of water-splitting photocatalysts, expect that (1) the band edge positions should now bracket different redox levels; (2) the selective kinetics at the photocatalyst-solution interface should now favor the CO_2 reduction reaction; (3) the p-type photocatalysts are preferred in this application. Therefore, we can, in principle, still screen the candidate materials based on their phase stability, band gap and band edge positions, and exam other required properties individually. The potential challenge comes from the candidates generation step (Section 3.2.0), since most known photocatalysts in this application are molecular (organic) materials but our algorithm for proposing new possible stable materials currently considers only inorganic compounds. Therefore, an alternative method needs to be developed to suggest a large number of possible candidate materials as potential photocatalysts for CO_2 reduction.

Reaction, VS. NHE @ pH 7	Number of electrons	Potential (V)
$CO_2 + 2 H^+ + 2 e^- \rightarrow HCO_2H$	2	-0.61
$CO_2 + 2 H^+ + 2 e^- \rightarrow CO + H_2O$	2	-0.53
$CO_2 + 4 H^+ + 4 e^- \rightarrow HCHO + H_2O$	4	-0.48
$CO_2 + 6 H^+ + 6 e^- \rightarrow CH_3OH + H_2O$	6	-0.38
CO2 + 8 H^+ + 8 e- $\rightarrow CH_4 + 2 H_2O$	8	-0.24

Table. 5.1 Possible products for photochemical and photoelectrochemical CO_2 reduction.

Bibliography

1. Osterloh, F. E., Inorganic materials as catalysts for photochemical splitting of water. *Chem Mater* **2008,** *20* (1), 35-54.

2. Liao, P.; Carter, E. A., New concepts and modeling strategies to design and evaluate photo-electro-catalysts based on transition metal oxides. *Chemical Society Reviews* **2013,** *42* (6), 2401-2422.

3. Maeda, K.; Domen, K., New non-oxide photocatalysts designed for overall water splitting under visible light. *J Phys Chem C* **2007,** *111* (22), 7851-7861.

4. Benson, E. E.; Kubiak, C. P.; Sathrum, A. J.; Smieja, J. M., Electrocatalytic and homogeneous approaches to conversion of CO2 to liquid fuels. *Chemical Society Reviews* **2009,** *38* (1), 89.

5. Meyer, T. J., Chemical Approaches to Artificial Photosynthesis. *Accounts Chem Res* **1989,** *22* (5), 163-170.

6. Alstrum-Acevedo, J. H.; Brennaman, M. K.; Meyer, T. J., Chemical approaches to artificial photosynthesis. 2. *Inorg Chem* **2005,** *44* (20), 6802-6827.

7. Ruttinger, W.; Dismukes, G. C., Synthetic water-oxidation catalysts for artificial photosynthetic water oxidation. *Chem Rev* **1997,** *97* (1), 1-24.

8. Kumar, B.; Llorente, M.; Froehlich, J.; Dang, T.; Sathrum, A.; Kubiak, C. P., Photochemical and Photoelectrochemical Reduction of CO2. *Annu Rev Phys Chem* **2012,** *63*, 541.

9. Gratzel, M., Photoelectrochemical cells. *Nature* **2001,** *414* (6861), 338-344.

10. Fujishima, A.; Zhang, X. T.; Tryk, D. A., TiO2 photocatalysis and related surface phenomena. *Surf Sci Rep* **2008,** *63* (12), 515-582.

11. Wu, Y.; Chan, M. K. Y.; Ceder, G., Prediction of semiconductor band edge positions in aqueous environments from first principles. *Physical Review B* **2011,** *83* (23), 235301.

12. Sayama, K.; Mukasa, K.; Abe, R.; Abe, Y.; Arakawa, H., A new photocatalytic water splitting system under visible light irradiation mimicking a Z-scheme mechanism in photosynthesis. *J Photoch Photobio A* **2002,** *148* (1-3), 71-77.

13. Kato, II.; Iori, M.; Konta, R.; Shimodaira, Y.; Kudo, A., Construction of Z-scheme type heterogeneous photocatalysis systems for water splitting into H-2 and O-2 under visible light irradiation. *Chem Lett* **2004,** *33* (10), 1348-1349.

14. Abe, R., Recent progress on photocatalytic and photoelectrochemical water splitting under visible light irradiation. *J Photoch Photobio C* **2010,** *11* (4), 179-209.

15. Long, M.; Cai, W.; Cai, J.; Zhou, B.; Chai, X.; Wu, Y., Efficient photocatalytic degradation of phenol over Co3O4/BiVO4 composite under visible light irradiation. *J Phys Chem B* **2006,** *110* (41), 20211-6.

16. Kim, H. G.; Borse, P. H.; Choi, W.; Lee, J. S., Photocatalytic nanodiodes for visible-light photocatalysis. *Angewandte Chemie* **2005,** *44* (29), 4585-9.

17. Ye, F.; Ohmori, A.; Li, C., Formation of p-n junction by plasma spraying technique to enhance the photocatalytic activity of TiO2. *Journal of Materials Science* **2004,** *39* (1), 353-355.

18. Chen, Y.; Crittenden, J. C.; Hackney, S.; Sutter, L.; Hand, D. W., Preparation of a novel TiO2-based p-n junction nanotube photocatalyst. *Environmental science & technology* **2005,** *39* (5), 1201-8.

19. Liu, Z.; Zhao, Z.-G.; Miyauchi, M., Efficient Visible Light Active CaFe2O4/WO3Based Composite Photocatalysts: Effect of Interfacial Modification. *The Journal of Physical Chemistry C* **2009,** *113* (39), 17132-17137.

20. Inoue, Y.; Sato, K.; Sato, K., Photovoltaic and photocatalytic behaviour of a ferroelectric semiconductor, lead strontium zirconate titanate, with a polarization axis perpendicular to the surface. *Journal of the Chemical Society, Faraday Transactions 1* **1989,** *85* (7), 1765.

21. Dunn, S.; Stock, M., Artificial Photosynthesis - Use of a Ferroelectric Photocatalyst. *MRS Proceedings* **2012,** *1446.*

22. Zhang, X.; Huo, K.; Hu, L.; Wu, Z.; Chu, P. K., Synthesis and Photocatalytic Activity of Highly Ordered TiO2 and SrTiO3/TiO2 Nanotube Arrays on Ti Substrates. *Journal of the American Ceramic Society* **2010,** *93* (9), 2771-2778.

23. Matthews, R. W., Solar-Electric Water-Purification Using Photocatalytic Oxidation with Tio2 as a Stationary Phase. *Sol Energy* **1987,** *38* (6), 405-413.

24. Mills, A.; Davies, R. H.; Worsley, D., Water-Purification by Semiconductor Photocatalysis. *Chemical Society Reviews* **1993,** *22* (6), 417-425.

25. Fernandez, A.; Lassaletta, G.; Jimenez, V. M.; Justo, A.; GonzalezElipe, A. R.; Herrmann, J. M.; Tahiri, H.; AitIchou, Y., Preparation and characterization of TiO2 photocatalysts supported on various rigid supports (glass, quartz and stainless steel).

Comparative studies of photocatalytic activity in water purification. *Appl Catal B-Environ* **1995,** *7* (1-2), 49-63.

26. Shannon, M. A.; Bohn, P. W.; Elimelech, M.; Georgiadis, J. G.; Marinas, B. J.; Mayes, A. M., Science and technology for water purification in the coming decades. *Nature* **2008,** *452* (7185), 301-310.

27. Lewis, N. S.; Nocera, D. G., Powering the planet: Chemical challenges in solar energy utilization. *P Natl Acad Sci USA* **2006,** *103* (43), 15729-15735.

28. Huynh, W. U.; Dittmer, J. J.; Alivisatos, A. P., Hybrid nanorod-polymer solar cells. *Science* **2002,** *295* (5564), 2425-2427.

29. Bach, U.; Lupo, D.; Comte, P.; Moser, J. E.; Weissortel, F.; Salbeck, J.; Spreitzer, H.; Gratzel, M., Solid-state dye-sensitized mesoporous TiO2 solar cells with high photon-to-electron conversion efficiencies. *Nature* **1998,** *395* (6702), 583-585.

30. Green, M. A.; Emery, K.; King, D. L.; Igari, S.; Warta, W., Solar cell efficiency tables - (Version 26). *Prog Photovoltaics* **2005,** *13* (5), 387-392.

31. Frank, A. J.; Kopidakis, N.; van de Lagemaat, J., Electrons in nanostructured TiO2 solar cells: transport, recombination and photovoltaic properties. *Coordin Chem Rev* **2004,** *248* (13-14), 1165-1179.

32. Heller, A., Conversion of Sunlight into Electrical-Power and Photoassisted Electrolysis of Water in Photoelectrochemical Cells. *Accounts Chem Res* **1981,** *14* (5), 154-162.

33. Law, M.; Greene, L. E.; Johnson, J. C.; Saykally, R.; Yang, P. D., Nanowire dye-sensitized solar cells. *Nat Mater* **2005,** *4* (6), 455-459.

34. Nowotny, J.; Sorrell, C. C.; Bak, T.; Sheppard, L. R., Solar-hydrogen: Unresolved problems in solid-state science. *Sol Energy* **2005,** *78* (5), 593-602.

35. Fujishima, A.; Honda, K., Electrochemical Photolysis of Water at a Semiconductor Electrode. *Nature* **1972,** *238* (5358), 37.

36. Fujishima, A.; Honda, K., Studies on Photosensitive Electrode Reactions .3. Electrochemical Evidence for Mechanism of Primary Stage of Photosynthesis. *B Chem Soc Jpn* **1971,** *44* (4), 1148-&.

37. Goetzberger, A.; Hebling, C.; Schock, H. W., Photovoltaic materials, history, status and outlook. *Mat Sci Eng R* **2003,** *40* (1), 1-46.

38. Bolton, J. R.; Strickler, S. J.; Connolly, J. S., Limiting and Realizable Efficiencies of Solar Photolysis of Water. *Nature* **1985,** *316* (6028), 495-500.

39. Murphy, A. B.; Barnes, P. R. F.; Randeniya, L. K.; Plumb, I. C.; Grey, I. E.; Horne, M. D.; Glasscock, J. A., Efficiency of solar water splitting using semiconductor electrodes. *Int J Hydrogen Energ* **2006,** *31* (14), 1999-2017.

40. Tang, J. W.; Durrant, J. R.; Klug, D. R., Mechanism of photocatalytic water splitting in TiO(2). Reaction of water with photoholes, importance of charge carrier dynamics, and evidence for four-hole chemistry. *J Am Chem Soc* **2008,** *130* (42), 13885-13891.

41. Ni, M.; Leung, M. K. H.; Leung, D. Y. C.; Sumathy, K., A review and recent developments in photocatalytic water-splitting using TiO2 for hydrogen production. *Renewable and Sustainable Energy Reviews* **2007,** *11* (3), 401-425.

42. Linsebigler, A. L.; Lu, G. Q.; Yates, J. T., Photocatalysis on Tio2 Surfaces - Principles, Mechanisms, and Selected Results. *Chem Rev* **1995,** *95* (3), 735-758.

43. Hara, M.; Nunoshige, J.; Takata, T.; Kondo, J. N.; Domen, K., Unusual enhancement of H-2 evolution by Ru on TaON photocatalyst under visible light irradiation. *Chem Commun* **2003,** (24), 3000-3001.

44. Maeda, K.; Takata, T.; Hara, M.; Saito, N.; Inoue, Y.; Kobayashi, H.; Domen, K., GaN : ZnO solid solution as a photocatalyst for visible-light-driven overall water splitting. *J Am Chem Soc* **2005,** *127* (23), 8286-8287.

45. Du, X. S.; Li, Q. X.; Su, H. B.; Yang, J. L., Electronic and magnetic properties of V-doped anatase TiO2 from first principles. *Physical Review B* **2006,** *74* (23).

46. Shao, G. S., Red Shift in Manganese- and Iron-Doped TiO2: A DFT+U Analysis. *J Phys Chem C* **2009,** *113* (16), 6800-6808.

47. Weng, H. M.; Yang, X. P.; Dong, J. M.; Mizuseki, H.; Kawasaki, M.; Kawazoe, Y., Electronic structure and optical properties of the Co-doped anatase TiO2 studied from first principles. *Physical Review B* **2004,** *69* (12).

48. Gai, Y. Q.; Li, J. B.; Li, S. S.; Xia, J. B.; Wei, S. H., Design of Narrow-Gap TiO2: A Passivated Codoping Approach for Enhanced Photoelectrochemical Activity. *Phys Rev Lett* **2009,** *102* (3).

49. Yang, K. S.; Dai, Y.; Huang, B. B., Study of the Nitrogen concentration influence on N-Doped TiO2 Anatase from First-Principles Calculations. *J Phys Chem C* **2007,** *111* (32), 12086-12090.

50. Di Valentin, C.; Pacchioni, G.; Selloni, A.; Livraghi, S.; Giamello, E., Characterization of paramagnetic species in N-doped TiO2 powders by EPR spectroscopy and DFT calculations. *J Phys Chem B* **2005,** *109* (23), 11414-11419.

51. Yang, K. S.; Dai, Y.; Huang, B. B., Understanding photocatalytic activity of S- and P-doped TiO2 under visible light from first-principles. *J Phys Chem C* **2007,** *111* (51), 18985-18994.

52. Di Valentin, C.; Finazzi, E.; Pacchioni, G.; Selloni, A.; Livraghi, S.; Czoska, A. M.; Paganini, M. C.; Giamello, E., Density functional theory and electron paramagnetic resonance study on the effect of N-F codoping of TiO2. *Chem Mater* **2008,** *20* (11), 3706-3714.

53. Long, R.; English, N. J., Band gap engineering of double-cation-impurity-doped anatase-titania for visible-light photocatalysts: a hybrid density functional theory approach. *Phys Chem Chem Phys* **2011,** *13* (30), 13698-13703.

54. Long, R.; English, N. J., Band gap engineering of (N, Si)-codoped TiO2 from hybrid density functional theory calculations. *New J Phys* **2012,** *14.*

55. Hohenberg, P.; Kohn, W., Inhomogeneous Electron Gas. *Physical Review* **1964,** *136* (3B), B864-B871.

56. Kohn, W.; Sham, L. J., Self-Consistent Equations Including Exchange and Correlation Effects. *Physical Review* **1965,** *140* (4A), A1133-A1138.

57. Ji, G. H.; Gu, Z. B.; Lu, M. H.; Zhou, J. A.; Zhang, S. T.; Chen, Y. F., First principles calculations of N:H co-doping effect on energy gap narrowing of ZnO. *Physica B* **2010,** *405* (24), 4948-4950.

58. Xu, Z.; Zheng, Q. R.; Su, G., Charged states and band-gap narrowing in codoped ZnO nanowires for enhanced photoelectrochemical responses: Density functional first-principles calculations. *Physical Review B* **2012,** *85* (7).

59. Wang, F. G.; Di Valentin, C.; Pacchioni, G., Doping of WO3 for Photocatalytic Water Splitting: Hints from Density Functional Theory. *J Phys Chem C* **2012,** *116* (16), 8901-8909.

60. Shi, W. J.; Xiong, S. J., Ab initio study on band-gap narrowing in SrTiO3 with Nb-C-Nb codoping. *Physical Review B* **2011,** *84* (20).

61. Wei, W.; Dai, Y.; Guo, M.; Yu, L.; Jin, H.; Han, S. H.; Huang, B. B., Codoping synergistic effects in N-doped SrTiO3 for higher energy conversion efficiency. *Phys Chem Chem Phys* **2010,** *12* (27), 7612-7619.

62. Zunger, A.; Jaffe, J. E., Structural Origin of Optical Bowing in Semiconductor Alloys. *Phys Rev Lett* **1983,** *51* (8), 662-665.

63. Sun, R. S.; Ceder, G., Feasibility of band gap engineering of pyrite FeS2. *Physical Review B* **2011,** *84* (24).

64. Hitoki, G.; Ishikawa, A.; Takata, T.; Kondo, J. N.; Hara, M.; Domen, K., Ta3N5 as a novel visible light-driven photocatalyst (lambda < 600 nm). *Chem Lett* **2002,** (7), 736-737.

65. Yokoyama, D.; Hashiguchi, H.; Maeda, K.; Minegishi, T.; Takata, T.; Abe, R.; Kubota, J.; Domen, K., Ta3N5 photoanodes for water splitting prepared by sputtering. *Thin Solid Films* **2011,** *519* (7), 2087-2092.

66. Sato, J.; Saito, N.; Yamada, Y.; Maeda, K.; Takata, T.; Kondo, J. N.; Hara, M.; Kobayashi, H.; Domen, K.; Inoue, Y., RuO2-loaded beta-Ge3N4 as a non-oxide photocatalyst for overall water splitting. *J Am Chem Soc* **2005,** *127* (12), 4150-4151.

67. Yamasita, D.; Takata, T.; Hara, M.; Kondo, J. N.; Domen, K., Recent progress of visible-light-driven heterogeneous photocatalysts for overall water splitting. *Solid State Ionics* **2004,** *172* (1-4), 591-595.

68. Kasahara, A.; Nukumizu, K.; Hitoki, G.; Takata, T.; Kondo, J. N.; Hara, M.; Kobayashi, H.; Domen, K., Photoreactions on LaTiO2N under visible light irradiation. *J Phys Chem A* **2002,** *106* (29), 6750-6753.

69. Hitoki, G.; Takata, T.; Kondo, J. N.; Hara, M.; Kobayashi, H.; Domen, K., (Oxy)nitrides as new photocatalysts for water splitting under visible light irradiation. *Electrochemistry* **2002,** *70* (6), 463-465.

70. Castelli, I. E.; Olsen, T.; Datta, S.; Landis, D. D.; Dahl, S.; Thygesen, K. S.; Jacobsen, K. W., Computational screening of perovskite metal oxides for optimal solar light capture. *Energ Environ Sci* **2012,** *5* (2), 5814-5819.

71. Wu, Y.; Lazic, P.; Hautier, G.; Persson, K.; Ceder, G., First principles high throughput screening of oxynitrides for water-splitting photocatalysts. *Energ Environ Sci* **2013,** *6* (1), 157-168.

72. Castelli, I. E.; Landis, D. D.; Thygesen, K. S.; Dahl, S.; Chorkendorff, I.; Jaramillo, T. F.; Jacobsen, K. W., New cubic perovskites for one- and two-photon water splitting using the computational materials repository. *Energ Environ Sci* **2012,** *5* (10), 9034-9043.

73. Jain, A.; Castelli, I. E.; Hautier, G.; Bailey, D. H.; Jacobsen, K. W., Performance of genetic algorithms in search for water splitting perovskites. *Journal of Materials Science* **2013**.

74. Hautier, G.; Jain, A.; Ong, S. P.; Kang, B.; Moore, C.; Doe, R.; Ceder, G., Phosphates as Lithium-Ion Battery Cathodes: An Evaluation Based on High-Throughput ab Initio Calculations. *Chem Mater* **2011,** *23* (15), 3495-3508.

75. Jain, A.; Hautier, G.; Moore, C.; Kang, B.; Lee, J.; Chen, H. L.; Twu, N.; Ceder, G., A Computational Investigation of Li9M3(P2O7)(3)(PO4)(2) (M = V, Mo) as Cathodes for Li Ion Batteries. *J Electrochem Soc* **2012,** *159* (5), A622-A633.

76. Chen, H. L.; Hautier, G.; Jain, A.; Moore, C.; Kang, B.; Doe, R.; Wu, L. J.; Zhu, Y. M.; Tang, Y. Z.; Ceder, G., Carbonophosphates: A New Family of Cathode Materials for Li-Ion Batteries Identified Computationally. *Chem Mater* **2012,** *24* (11), 2009-2016.

77. Hautier, G.; Jain, A.; Chen, H. L.; Moore, C.; Ong, S. P.; Ceder, G., Novel mixed polyanions lithium-ion battery cathode materials predicted by high-throughput ab initio computations. *J Mater Chem* **2011,** *21* (43), 17147-17153.

78. Wang, S. D.; Wang, Z.; Setyawan, W.; Mingo, N.; Curtarolo, S., Assessing the Thermoelectric Properties of Sintered Compounds via High-Throughput Ab-Initio Calculations. *Phys Rev X* **2011,** *1* (2).

79. Madsen, G. K. H., Automated search for new thermoelectric materials: The case of LiZnSb. *J Am Chem Soc* **2006,** *128* (37), 12140-12146.

80. Armiento, R.; Kozinsky, B.; Fornari, M.; Ceder, G., Screening for high-performance piezoelectrics using high-throughput density functional theory. *Physical Review B* **2011,** *84* (1).

81. Hachmann, J.; Olivares-Amaya, R.; Atahan-Evrenk, S.; Amador-Bedolla, C.; Sanchez-Carrera, R. S.; Gold-Parker, A.; Vogt, L.; Brockway, A. M.; Aspuru-Guzik, A., The Harvard Clean Energy Project: Large-Scale Computational Screening and Design of

Organic Photovoltaics on the World Community Grid. *J Phys Chem Lett* **2011,** *2* (17), 2241-2251.

82. Sokolov, A. N.; Atahan-Evrenk, S.; Mondal, R.; Akkerman, H. B.; Sanchez-Carrera, R. S.; Granados-Focil, S.; Schrier, J.; Mannsfeld, S. C. B.; Zoombelt, A. P.; Bao, Z. N.; Aspuru-Guzik, A., From computational discovery to experimental characterization of a high hole mobility organic crystal. *Nat Commun* **2011,** *2.*

83. O'Boyle, N. M.; Campbell, C. M.; Hutchison, G. R., Computational Design and Selection of Optimal Organic Photovoltaic Materials. *J Phys Chem C* **2011,** *115* (32), 16200-16210.

84. Jain, A.; Hautier, G.; Moore, C. J.; Ong, S. P.; Fischer, C. C.; Mueller, T.; Persson, K. A.; Ceder, G., A high-throughput infrastructure for density functional theory calculations. *Comp Mater Sci* **2011,** *50* (8), 2295-2310.

85. Ceder, G.; Hautier, G.; Jain, A.; Ong, S. P., Recharging lithium battery research with first-principles methods. *Mrs Bull* **2011,** *36* (3), 185-191.

86. Hautier, G.; Ong, S. P.; Jain, A.; Moore, C. J.; Ceder, G., Accuracy of density functional theory in predicting formation energies of ternary oxides from binary oxides and its implication on phase stability. *Physical Review B* **2012,** *85* (15).

87. Chan, M. K. Y.; Ceder, G., Efficient Band Gap Prediction for Solids. *Phys Rev Lett* **2010,** *105* (19).

88. *http://www.titandioxide.ru/titan_s/sc3/0176.php*.

89. Blöchl, P. E., Projector augmented-wave method. *Physical Review B* **1994,** *50* (24), 17953-17979.

90. Perdew, J. P.; Burke, K.; Ernzerhof, M., Generalized Gradient Approximation Made Simple. *Phys Rev Lett* **1996,** *77* (18), 3865-3868.

91. De Angelis, F.; Fantacci, S.; Selloni, A., Alignment of the dye's molecular levels with the TiO(2) band edges in dye-sensitized solar cells: a DFT-TDDFT study. *Nanotechnology* **2008,** *19* (42), 424002.

92. Coe, J. V.; Earhart, A. D.; Cohen, M. H.; Hoffman, G. J.; Sarkas, H. W.; Bowen, K. H., Using cluster studies to approach the electronic structure of bulk water: Reassessing the vacuum level, conduction band edge, and band gap of water. *J Chem Phys* **1997,** *107* (16), 6023-6031.

93. Rhoderick, E. H., Metal-Semiconductor Contacts. *Iee Proc-I* **1982,** *129* (1), 1-14.

94. Van de Walle, C. G.; Neugebauer, J., Universal alignment of hydrogen levels in semiconductors, insulators and solutions. *Nature* **2003,** *423* (6940), 626-8.

95. Franciosi, A.; VandeWalle, C. G., Heterojunction band offset engineering. *Surf Sci Rep* **1996,** *25* (1-4), 1.

96. Majewski, J. A.; Stadele, M.; Vogl, P., Stability and band offsets of SiC/GaN, SiC/AlN, and AlN/GaN heterostructures. *Mater Res Soc Symp P* **1997,** *449*, 917-922.

97. Cheng, J.; Sprik, M., Aligning electronic energy levels at the TiO2/H2O interface. *Physical Review B* **2010,** *82* (8).

98. Cheng, J.; Sulpizi, M.; Sprik, M., Redox potentials and pK(a) for benzoquinone from density functional theory based molecular dynamics. *J Chem Phys* **2009,** *131* (15).

99. Shaltaf, R.; Rignanese, G. M.; Gonze, X.; Giustino, F.; Pasquarello, A., Band offsets at the Si/SiO(2) interface from many-body perturbation theory. *Phys Rev Lett* **2008,** *100* (18).

100. Alkauskas, A.; Broqvist, P.; Devynck, F.; Pasquarello, A., Band offsets at semiconductor-oxide interfaces from hybrid density-functional calculations. *Phys Rev Lett* **2008,** *101* (10).

101. Mrovec, M.; Albina, J. M.; Meyer, B.; Elsasser, C., Schottky barriers at transition-metal/SrTiO3(001) interfaces. *Physical Review B* **2009,** *79* (24).

102. Grossman, J. C.; Schwegler, E.; Draeger, E. W.; Gygi, F.; Galli, G., Towards an assessment of the accuracy of density functional theory for first principles simulations of water. *J Chem Phys* **2004,** *120* (1), 300-311.

103. Schwegler, E.; Grossman, J. C.; Gygi, F.; Galli, G., Towards an assessment of the accuracy of density functional theory for first principles simulations of water. II. *J Chem Phys* **2004,** *121* (11), 5400-5409.

104. Prendergast, D.; Grossman, J. C.; Galli, G., The electronic structure of liquid water within density-functional theory. *J Chem Phys* **2005,** *123* (1).

105. Nozik, A. J.; Memming, R., Physical Chemistry of Semiconductor−Liquid Interfaces. *The Journal of Physical Chemistry* **1996,** *100* (31), 13061-13078.

106. Nozik, A. J., Photoelectrochemistry: Applications to Solar Energy Conversion. *Annual Review of Physical Chemistry* **1978,** *29* (1), 189-222.

107. Kresse, G.; Furthmüller, J., Efficient iterative schemes for ab initio total-energy calculations using a plane-wave basis set. *Physical Review B* **1996,** *54* (16), 11169-11186.

108. Kresse, G.; Joubert, D., From ultrasoft pseudopotentials to the projector augmented-wave method. *Physical Review B* **1999,** *59* (3), 1758-1775.

109. Monkhorst, H. J.; Pack, J. D., Special points for Brillouin-zone integrations. *Physical Review B* **1976,** *13* (12), 5188-5192.

110. Smith, W.; Forester, T. R., DL_POLY_2.0: A general-purpose parallel molecular dynamics simulation package. *J Mol Graphics* **1996,** *14* (3), 136-141.

111. Jorgensen, W. L.; Chandrasekhar, J.; Madura, J. D.; Impey, R. W.; Klein, M. L., Comparison of Simple Potential Functions for Simulating Liquid Water. *J Chem Phys* **1983,** *79* (2), 926-935.

112. Hermida-Ramon, J. M.; Karlstrom, G., Study of the hydronium ion in water. A combined quantum chemical and statistical mechanical treatment. *J Mol Struc-Theochem* **2004,** *712* (1-3), 167-173.

113. Dudarev, S. L.; Botton, G. A.; Savrasov, S. Y.; Humphreys, C. J.; Sutton, A. P., Electron-energy-loss spectra and the structural stability of nickel oxide: An LSDA+U study. *Physical Review B* **1998,** *57* (3), 1505-1509.

114. Komsa, H. P.; Broqvist, P.; Pasquarello, A., Alignment of defect levels and band edges through hybrid functionals: Effect of screening in the exchange term. *Physical Review B* **2010,** *81* (20).

115. Hedin, L., New Method for Calculating 1-Particle Greens Function with Application to Electron-Gas Problem. *Physical Review* **1965,** *139* (3A), A796.

116. Becke, A. D., Density-Functional Thermochemistry .3. The Role of Exact Exchange. *J Chem Phys* **1993,** *98* (7), 5648-5652.

117. Lee, C. T.; Yang, W. T.; Parr, R. G., Development of the Colle-Salvetti Correlation-Energy Formula into a Functional of the Electron-Density. *Physical Review B* **1988,** *37* (2), 785-789.

118. Perdew, J. P.; Emzerhof, M.; Burke, K., Rationale for mixing exact exchange with density functional approximations. *J Chem Phys* **1996,** *105* (22), 9982-9985.

119. Heyd, J.; Scuseria, G. E.; Ernzerhof, M., Hybrid functionals based on a screened Coulomb potential. *J Chem Phys* **2003,** *118* (18), 8207-8215.

120. Krukau, A. V.; Vydrov, O. A.; Izmaylov, A. F.; Scuseria, G. E., Influence of the exchange screening parameter on the performance of screened hybrid functionals. *J Chem Phys* **2006,** *125* (22).

121. Inorganic Crystal Structure Database *Inorganic Crystal Structure Database (http://icsd.fiz-karlsruhe.de/icsd/)*.

122. Hautier, G.; Fischer, C.; Ehrlacher, V.; Jain, A.; Ceder, G., Data Mined Ionic Substitutions for the Discovery of New Compounds. *Inorg Chem* **2011,** *50* (2), 656-663.

123. Hart, G. L. W.; Forcade, R. W., Algorithm for generating derivative structures. *Physical Review B* **2008,** *77* (22).

124. Yang, M. H.; Oro-Sole, J.; Rodgers, J. A.; Jorge, A. B.; Fuertes, A.; Attfield, J. P., Anion order in perovskite oxynitrides. *Nat Chem* **2011,** *3* (1), 47-52.

125. Jain, A.; Hautier, G.; Ong, S. P.; Moore, C. J.; Fischer, C. C.; Persson, K. A.; Ceder, G., Formation enthalpies by mixing GGA and GGA plus U calculations. *Physical Review B* **2011,** *84* (4).

126. Wrighton, M. S.; Ginley, D. S.; Wolczanski, P. T.; Ellis, A. B.; Morse, D. L.; Linz, A., Photoassisted Electrolysis of Water by Irradiation of a Titanium-Dioxide Electrode. *P Natl Acad Sci USA* **1975,** *72* (4), 1518-1522.

127. Walter, M. G.; Warren, E. L.; McKone, J. R.; Boettcher, S. W.; Mi, Q. X.; Santori, E. A.; Lewis, N. S., Solar Water Splitting Cells. *Chem Rev* **2010,** *110* (11), 6446-6473.

128. T. Lindgren; M. Larsson; Lindquist, S. E., *Proc. 14th Int. Workshop on Quantum Solar Energy Conversion* **2002.**

129. Smith, A. R.; AL-Brithen, H. A. H.; Ingram, D. C.; Gall, D., Molecular beam epitaxy control of the structural, optical, and electronic properties of ScN(001). *J Appl Phys* **2001,** *90* (4), 1809-1816.

130. Bergman, L.; Chen, X. B.; McIlroy, D.; Davis, R. F., Probing the AlxGa1-xN spatial alloy fluctuation via UV-photoluminescence and Raman at submicron scale. *Appl Phys Lett* **2002,** *81* (22), 4186-4188.

131. Hara, M.; Hitoki, G.; Takata, T.; Kondo, J. N.; Kobayashi, H.; Domen, K., TaON and Ta3N5 as new visible light driven photocatalysts. *Catal Today* **2003,** *78* (1-4), 555-560.

132. Bar, M.; Ahn, K. S.; Shet, S.; Yan, Y.; Weinhardt, L.; Fuchs, O.; Blum, M.; Pookpanratana, S.; George, K.; Yang, W.; Denlinger, J. D.; Al-Jassim, M.; Heske, C., Impact of air exposure on the chemical and electronic structure of ZnO:Zn3N2 thin films. *Appl Phys Lett* **2009,** *94* (1).

133. Becker, J. S.; Kim, E.; Gordon, R. G., Atomic layer deposition of insulating hafnium and zirconium nitrides. *Chem Mater* **2004,** *16* (18), 3497-3501.

134. Rees, C. S.; Chaudhri, M. M., The Electrical-Conductivity of Silver Azide (Agn3) at High Hydrostatic Pressures. *J Phys C Solid State* **1987,** *20* (26), 4097-4104.

135. Kroll, P., Hafnium nitride with thorium phosphide structure: Physical properties and an assessment of the Hf-N, Zr-N, and Ti-N phase diagrams at high pressures and temperatures. *Phys Rev Lett* **2003,** *90* (12).

136. Chen, J. J.; Gila, B. P.; Hlad, M.; Gerger, A.; Ren, F.; Abernathy, C. R.; Pearton, S. J., Band offsets in the Sc2O3/GaN heterojunction system. *Appl Phys Lett* **2006,** *88* (14).

137. Mishima, T.; Matsuda, M.; Miyake, M., Visible-light photocatalytic properties and electronic structure of Zr-based oxynitride, Zr2ON2, derived from nitridation of ZrO2. *Appl Catal a-Gen* **2007,** *324*, 77-82.

138. Maeda, K.; Higashi, M.; Siritanaratkul, B.; Abe, R.; Domen, K., SrNbO2N as a Water-Splitting Photoanode with a Wide Visible-Light Absorption Band. *J Am Chem Soc* **2011,** *133* (32), 12334-12337.

139. Siritanaratkul, B.; Maeda, K.; Hisatomi, T.; Domen, K., Synthesis and Photocatalytic Activity of Perovskite Niobium Oxynitrides with Wide Visible-Light Absorption Bands. *Chemsuschem* **2011,** *4* (1), 74-78.

140. Tobias, G.; Beltran-Porter, D.; Lebedev, O. I.; Van Tendeloo, G.; Rodriguez-Carvajal, J.; Fuertes, A., Anion ordering and defect structure in Ruddlesden-Popper strontium niobium oxynitrides. *Inorg Chem* **2004,** *43* (25), 8010-8017.

141. Pourbaix, M., *Atlas of Electrochemical Equilibria in Aqueous Solutions (National Association of Corrosion Engineers, Houston, Texas)* (1974).

142. Persson, K. A.; Waldwick, B.; Lazic, P.; Ceder, G., Prediction of solid-aqueous equilibria: Scheme to combine first-principles calculations of solids with experimental aqueous states. *Physical Review B* **2012,** *85* (23).

143. Dareedwards, M. P.; Goodenough, J. B.; Hamnett, A.; Trevellick, P. R., Electrochemistry and Photoelectrochemistry of Iron(Iii) Oxide. *J Chem Soc Farad T 1* **1983,** *79*, 2027-2041.

144. Zhai, H. J.; Li, S.; Dixon, D. A.; Wang, L. S., Probing the electronic and structural properties of chromium oxide clusters (CrO3)(n)(-) and (CrO3)(n) (n=1-5):

Photoelectron Spectroscopy and density functional calculations. *J Am Chem Soc* **2008,** *130* (15), 5167-5177.

145. Higashiwaki, M.; Sasaki, K.; Kuramata, A.; Masui, T.; Yamakoshi, S., Gallium oxide (Ga2O3) metal-semiconductor field-effect transistors on single-crystal beta-Ga2O3 (010) substrates. *Appl Phys Lett* **2012,** *100* (1).

146. Zyubin, A. S.; Mebel, A. M.; Lin, S. H., Optical properties of oxygen vacancies in germanium oxides: Quantum chemical modeling of photoexcitation and photoluminescence. *J Phys Chem A* **2007,** *111* (38), 9479-9485.

147. Zhu, W. J.; Tamagawa, T.; Gibson, M.; Furukawa, T.; Ma, T. P., Effect of Al inclusion in HfO2 on the physical and electrical properties of the dielectrics. *Ieee Electr Device L* **2002,** *23* (11), 649-651.

148. Piper, L. F. J.; DeMasi, A.; Cho, S. W.; Smith, K. E.; Fuchs, F.; Bechstedt, F.; Korber, C.; Klein, A.; Payne, D. J.; Egdell, R. G., Electronic structure of In2O3 from resonant x-ray emission spectroscopy. *Appl Phys Lett* **2009,** *94* (2).

149. Mai, L. Q.; Hu, B.; Chen, W.; Qi, Y. Y.; Lao, C. S.; Yang, R. S.; Dai, Y.; Wang, Z. L., Lithiated MoO3 nanobelts with greatly improved performance for lithium batteries. *Adv Mater* **2007,** *19* (21), 3712.

150. Kurmaev, E. Z.; Moewes, A.; Bureev, O. G.; Nekrasov, I. A.; Cherkashenko, V. M.; Korotin, M. A.; Ederer, D. L., Electronic structure of niobium oxides. *J Alloy Compd* **2002,** *347* (1-2), 213-218.

151. Nainani, A.; Sun, Y.; Irisawa, T.; Yuan, Z.; Kobayashi, M.; Pianetta, P.; Bennett, B. R.; Boos, J. B.; Saraswat, K. C., Device quality Sb-based compound semiconductor surface: A comparative study of chemical cleaning. *J Appl Phys* **2011,** *109* (11).

152. Emeline, A. V.; Lobyntseva, E. V.; Ryabchuk, V. K.; Serpone, N., Spectral dependencies of the quantum yield of photochemical processes on the surface of wide-band-gap metal oxides. 2. Gas/solid system involving scandia (Sc2O3) particles. *J Phys Chem B* **1999,** *103* (8), 1325-1331.

153. Kilic, C.; Zunger, A., Origins of coexistence of conductivity and transparency in SnO2. *Phys Rev Lett* **2002,** *88* (9).

154. Chakrabarti, A.; Hermann, K.; Druzinic, R.; Witko, M.; Wagner, F.; Petersen, M., Geometric and electronic structure of vanadium pentoxide: A density functional bulk and surface study. *Physical Review B* **1999,** *59* (16), 10583-10590.

155. Jia, D. D.; Wang, X. J.; Yen, W. M., Delocalization, thermal ionization, and energy transfer in singly doped and codoped CaAl4O7 and Y2O3. *Physical Review B* **2004,** *69* (23).

156. Emeline, A.; Kataeva, G. V.; Litke, A. S.; Rudakova, A. V.; Ryabchuk, V. K.; Serpone, N., Spectroscopic and photoluminescence studies of a wide band gap insulating material: Powdered and colloidal ZrO2 sols. *Langmuir* **1998,** *14* (18), 5011-5022.

157. Zou, Z. G.; Arakawa, H., Direct water splitting into H-2 and O-2 under visible light irradiation with a new series of mixed oxide semiconductor photocatalysts. *J Photoch Photobio A* **2003,** *158* (2-3), 145-162.

158. Zou, Z. G.; Ye, J. H.; Sayama, K.; Arakawa, H., Direct splitting of water under visible light irradiation with an oxide semiconductor photocatalyst. *Nature* **2001,** *414* (6864), 625-627.

159. Kanan, D. K.; Carter, E. A., Band Gap Engineering of MnO via ZnO Alloying: A Potential New Visible-Light Photocatalyst. *The Journal of Physical Chemistry C* **2012,** *116* (18), 9876-9887.

160. Brese, N. E.; O'Keeffe, M.; Rauch, P.; DiSalvo, F. J., Structure of Ta3N5 at 16 K by time-of-flight neutron diffraction. *Acta Crystallographica Section C Crystal Structure Communications* **1991,** *47* (11), 2291-2294.

161. Heyd, J.; Scuseria, G. E.; Ernzerhof, M., Hybrid functionals based on a screened Coulomb potential (vol 118, pg 8207, 2003). *J Chem Phys* **2006,** *124* (21).

162. Tepesch, P. D.; Kohan, A. E.; Garbulsky, G. D.; Ceder, G.; Coley, C.; Stokes, H. T.; Boyer, L. L.; Mehl, M. J.; Burton, B. P.; Cho, K. J.; Joannopoulos, J., A model to compute phase diagrams in oxides with empirical or first-principles energy methods and application to the solubility limits in the CaO-MgO system. *Journal of the American Ceramic Society* **1996,** *79* (8), 2033-2040.

163. Ceder, G.; Kohan, A. F.; Aydinol, M. K.; Tepesch, P. D.; Van der Ven, A., Thermodynamics of oxides with substitutional disorder: A microscopic model and evaluation of important energy contributions. *Journal of the American Ceramic Society* **1998,** *81* (3), 517-525.

164. Kato, H.; Kudo, A., Photocatalytic water splitting into H2 and O2 over various tantalate photocatalysts. *Catal Today* **2003,** *78* (1-4), 561-569.

165. Chen, S.; Wang, L.-W., Thermodynamic Oxidation and Reduction Potentials of Photocatalytic Semiconductors in Aqueous Solution. *Chem Mater* **2012,** *24* (18), 3659-3666.